“Multiheterodyne tunable sources for the interrogation of fiber optic sensors applied to acoustic emissions and ultrasound”

by

Dragoş Andrei Poiană

A dissertation submitted by in partial fulfillment of the requirements for the degree of Doctor of Philosophy in

ELECTRICAL ENGINEERING, ELECTRONICS AND AUTOMATION

Universidad Carlos III de Madrid

Advisor:

José Antonio García Souto

Tutor:

José Antonio García Souto

May 2022

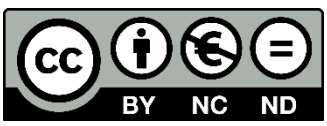

Acknowledgments

Esta es sin duda la parte más importante de este documento. De no ser por el apoyo de ciertas personas, este trabajo nunca habría sido posible.

En primer lugar, quisiera agradecer a mi supervisor José Antonio García Souto por enseñarme todo lo que sé, por su tiempo, paciencia y mesura. Porque me ha enseñado a hacerme las preguntas correctas aun cuando mis respuestas no fueran las más claras.

Le debo mucho al grupo de investigación, desde 2016 me acogieron y me hicieron crecer. Debo dar las gracias por haber estado cerca de personas mucho mejores que yo, a todos los niveles, y que por ello me han ido llevado hacia esa dirección tanto a nivel técnico como personal.

Con esta tesis culmino una etapa que me ha enseñado mucho sobre el mundo y sobre mí mismo. Me ha enseñado a tener un pensamiento crítico e independiente. Me ha enseñado qué pasiones escondidas tengo, en qué soy competente y en qué no, me ha enseñado nuevas habilidades que sin duda me van a servir mucho a lo largo de mi vida profesional y personal.

He de agradecer a Alba, Alberto, Aldo, Borja, Daiana, Farid, Jaime, Julio, Leonardo, Mónica, Oscar, Pedro por las tardes del viernes, y por atenuar los altibajos emocionales propios de la investigación con un filtro paso-bajo de decimo orden.

I have to thank Prof. Xiaoyi Bao for her supervision during my productive research stay at the University of Ottawa.

A la gente que me quiso alguna vez, a la gente que cree que me quiso y finalmente a la gente que no me quiso, que es poca. Sin ellos no estaría aquí. Porque como dijo una gran persona a la que admiro mucho, siempre hay que quedarse con las personas mejores que uno, ellos te moldean y te

llevan en una buena dirección. Porque la única felicidad está en rodearse de personas a las que uno admira.

Finalmente, y más importante a mi madre por haberme apoyado a lo largo de toda mi vida de manera incondicional por saber más que yo y porque en cada conversación que tenemos acerca de la vida me hace más fuerte y sabio.

Quiero agradecer la financiación de este trabajo dada por el Ministerio de Educación, Cultura y Deporte para la Formación de Profesorado Universitario FPU2016 (Beca FPU16/03695) y a través del proyecto PARAQUA (TEC2017-86271-R), así como por el Ministerio de Ciencia, Innovación y Universidades a través de las ayudas de movilidad EST18/00617.

Journal papers

Poiana, D.A, Posada-Román, J.E. and García-Souto, J.A. "Compact Interrogation System of Fiber Bragg Grating Sensors based on Multiheterodyne Dispersion Interferometry for Dynamic Strain Measurements". Sensors, 2022, 22, 3561. doi.org/10.3390/s22093561

Poiana, D.A.; García-Souto, J.A.; Bao, X. "Acousto-Optic Comb Interrogation System for Random Fiber Grating Sensors with Sub-nm Resolution". Sensors, 2021, 21, 3967. doi.org/10.3390/s21123967

Posada-Román, J.E.; García-Souto, J.A.; **Poiana, D.A.**; Acedo, P. "Fast Interrogation of Fiber Bragg Gratings with Electro-Optical Dual Optical Frequency Combs". Sensors 2016, 16, 2007. doi.org/10.3390/s16122007

Conference papers

- **Dragos A. Poiana**, Pedro Martín-Mateos and José A. García-Souto, "Multiheterodyne differential spectroscopy using dual-comb generation based on a dual-drive Mach Zehnder modulator", in OSA Conference on Lasers and Electro-Optics, CLEO2021, 2021

- **Dragos A. Poiana**, José A. García-Souto and Xiaoyi Bao, "Acousto-optic self-heterodyne comb readout for strain sensing with random fiber grating", in 27th International Conference on Optical Fiber Sensors, OFS27, 2020

- **Dragos A. Poiana**, Julio E. Posada-Román and José A. García-Souto, "Interrogation of fiber Bragg grating sensors based on dispersion spectroscopy with optical frequency combs", in 27th International Conference on Optical Fiber Sensors, OFS27, 2020

- **Dragos A. Poiana**, Julio E. Posada-Román and José A. García-Souto, "Compact system of dispersion spectroscopy for interrogating fiber Bragg grating sensors using multi-wavelength phase shift interferometry", in IEEE International Instrumentation and Measurement Technology Conference (I2MTC), I2MTC, 2020

- **Dragos A. Poiana,** José A. García-Souto, Julio E. Posada-Román and Pablo Acedo, "Dynamic readout of a fiber Bragg gratings serial array based on all electro-optical dual optical frequency comb", in OSA Optical Sensors and Sensing Congress, 2019

- **Dragos A. Poiana**, José A. García-Souto, Julio E. Posada-Román and Pablo Acedo, "All-fiber electro-optic dual optical frequency comb for fiber sensors", in 26th International Conference on Optical Fiber Sensors, OFS26, 2018

- **Dragos A. Poiana**, Julio E. Posada Román, P. Acedo y José A. García Souto, "Espectroscopía Multimodal en Sensores de Fibra Óptica para Aplicaciones Industriales", en 25º Seminario Anual de Automática, Electrónica Industrial e Instrumentación, SAAEI, 2018

- **Dragos A. Poiana**, José A. García-Souto, Julio E. Posada-Román and Pablo Acedo, "Stabilization of coherent dual optical frequency comb for fiber Bragg grating sensing", in IEEE SENSORS, 2017

- **Dragos A. Poiana**, José A. García-Souto, Julio E. Posada-Román and Pablo Acedo, "Interrogation system with auto-calibration for fiber Bragg grating sensors using VCSEL based optical frequency comb generators", in 25th International Conference on Optical Fiber Sensors, OFS25, 2017

- **Dragos A. Poiana**, José A. García Souto, Julio E. Posada Román y Pablo Acedo, "Sistema de Instrumentación Optoelectrónico para la Medida de Vibraciones Ultrasónicas con Redes de Bragg en Fibra", en 24º Seminario Anual de Automática, Electrónica Industrial e Instrumentación, SAAEI, 2017

- Julio E. Posada-Roman, **Dragos A. Poiana**, José A. García-Souto and Pablo Acedo, "Interrogation of FBG Sensors Based on Electro-optic Dual Optical Frequency Combs", in OSA Latin America Optics and Photonics Conference, LAOP, 2016

Other conference papers

- Ana K. Reascos-Portilla, **Dragos A. Poiana**, Julio E. Posada-Román and José A. García-Souto, "Fiber optic temperature sensor for nanosatellites", in IEEE International Instrumentation and Measurement Technology Conference (I2MTC), I2MTC, 2020

- Ana K. Reascos Portilla, **Dragos A. Poiana**, Julio E. Posada Román y José A. García Souto, "Sensor de temperatura en fibra óptica para nanosatélites", en 27º Seminario Anual de Automática, Electrónica Industrial e Instrumentación, SAAEI, 2020

- **Dragos A. Poiana** y José A. García Souto, "Sensor de temperatura con fibra óptica basado en interferómetro de Michelson y modulación de la frecuencia óptica", en 27º Seminario Anual de Automática, Electrónica Industrial e Instrumentación, SAAEI, 2020

- **Dragos A. Poiana** y J. A. García Souto, “Salud estructural de conductos mediante medidas distribuidas espacialmente usando reflectometría óptica en el dominio de la frecuencia”, en 26º Seminario Anual de Automática, Electrónica Industrial e Instrumentación, SAAEI, 2019

- Alejandro J. Ramos San Juan, **Dragos A. Poiana** y José A. García Souto, “Sistema electrónico para interferometría con detección síncrona”, en 25º Seminario Anual de Automática, Electrónica Industrial e Instrumentación, SAAEI, 2018

Abstract

Light is a very useful tool for measuring high frequency and low amplitude mechanical vibrations. Thanks to the interference process and under certain circumstances we can obtain a specific sort of optical sources called multimode multiheterodyne sources, that are very useful to read several optical wavelengths at the same time on a single photodetector and distinguishing them from each other. This characteristic makes them suitable for interrogating fiber optic sensors.

In this thesis, I analyze several fiber optic sensor readout methods that mix multiheterodyne techniques, multimode techniques, and interferometry techniques to measure ultrasound and acoustic mechanical waves.

These mechanical waves occur when periodic forces are applied to mechanical structures. This disturbs the layout of atoms and may lead to cracks or the complete collapse of the structure. Therefore, the characterization and measurement of such vibrations are of great importance when performing structure health monitoring (SHM) and non-destructive evaluation (NDE).

This thesis aims to solve this problem by implementing several systems that employ light-based technology to measure and characterize mechanical vibrations up to 1 MHz of frequency and sub-nano-strain (lower than 10^{-3} ppm) level of resolution.

The proposed systems involve new features and parameters more settable compared to more conventional approaches of optical sensor reading processes and therefore they offer wider possibilities.

A total of three systems have been implemented and tested:

First, an electro-optic dual optical frequency comb source to read fiber Bragg gratings for dynamic measurements. This set up reaches 120 kHz of mechanical frequency detection.

The second system is based on a self-heterodyne acousto-optic comb that reads a random fiber grating sensor. In this case, the system can detect up to 1 MHz of mechanical vibrations.

Finally, the third is based on a compact electro-optic dual optical frequency comb that is used to read low reflectivity fiber Bragg gratings with a dispersion interferometer. This system can detect a maximum of 135 kHz of mechanical frequencies.

The results of this thesis improve previous systems achievements to satisfy the specifications required to date in this application, both in mechanical bandwidth and in strain amplitude. They also show the potential of these multimode sources for high-precision optical sensing.

Keywords: Optical fiber sensors, multimode sources, multiheterodyne sources, combs, interferometry, fiber Bragg gratings, random fiber grating, acoustic, ultrasound

Resumen

La luz es una herramienta muy útil para medir vibraciones mecánicas de alta frecuencia y baja amplitud. Gracias al proceso de interferencia y bajo determinadas circunstancias podemos obtener un tipo específico de fuentes ópticas, denominadas fuentes multimodo multiheterodinas, que son muy útiles para leer varias longitudes de onda ópticas al mismo tiempo en un solo fotodetector y distinguirlas entre sí. Esta característica hace que estas fuentes ópticas sean adecuadas para la lectura de sensores de fibra óptica.

En esta tesis, analizo varios métodos de lectura de sensores de fibra óptica que mezclan técnicas multiheterodinas, técnicas multimodo y técnicas de interferometría para medir ultrasonidos y ondas mecánicas acústicas.

Estas ondas mecánicas se producen cuando se aplican fuerzas periódicas a las estructuras mecánicas. Esto perturba la disposición de los átomos y puede provocar grietas o el colapso completo de la estructura. Por lo tanto, la caracterización y medida de dichas vibraciones son de gran importancia a la hora de monitorizar el estado de las estructuras y de realizar una evaluación no destructiva.

Esta tesis tiene como objetivo resolver este problema mediante la implementación de varios sistemas que emplean tecnología basada en la luz para medir y caracterizar vibraciones mecánicas hasta frecuencias de 1 MHz y nivel de resolución sub-nano-deformación (menor que 10^{-3} ppm).

Los sistemas propuestos implican nuevas características y parámetros más configurables en comparación con los enfoques más convencionales de procesos de lectura de sensores ópticos y, por lo tanto, ofrecen posibilidades más amplias.

A lo largo de la tesis se presentan tres sistemas de medida:

El primero está basado en un doble peine de frecuencias ópticas (*dual comb*) electroóptico que es capaz de leer sensores de fibra óptica basados en redes de Bragg (FBG) en régimen dinámico. Este sistema ha sido probado con una frecuencia máxima de detección de 120 kHz.

En segundo lugar, se presenta un sistema basado en un *selfheterodyne comb* acustoóptico para leer sensores de fibra con distribución aleatoria de la rejilla en el núcleo (*random grating*). Este sistema es capaz de detectar señales de vibración de hasta 1 MHz.

El tercer sistema presentado se basa en un doble peine de frecuencias ópticas (*dual comb*) electroóptico compacto que se utiliza para leer sensores FBG de baja reflectividad con un interferómetro de dispersión. Este sistema puede detectar hasta 135 kHz de vibraciones mecánicas.

Los resultados de esta tesis mejoran los obtenidos en sistemas anteriores a fin de satisfacer las especificaciones requeridas hasta la fecha en esta aplicación, tanto en el ancho de banda mecánico como en la amplitud de la deformación. También muestran el potencial de estas fuentes multimodo para la detección óptica de alta precisión.

Palabras clave: sensores de fibra óptica, fuentes multimodo, fuentes multiheterodinas, combs, interferometría, redes de Bragg en fibra, *random fiber grating*, acústica, ultrasonido

General index

Figure index

Table index

Chapter 1: Introduction and objectives

1.1 Motivation

Ultrasound and acoustic emissions are two kinds of mechanical waves that propagate through rigid structures and are subject to phenomena of fast force variation. Their study usually consists of determining the phase and amplitude as a function of time.

This simple problem encounters a main difficulty on the small signal-to-noise ratio. This challenge arises due to the low mechanical amplitude of such vibrations that occur at frequencies above 20 kHz. As we increase the mechanical frequency of oscillation, the structures under study start to behave like a low pass filter for which the higher frequencies are attenuated at a very significant rate. For our purpose, the amplitude can reach $n\varepsilon$ (nano-strain) levels for a frequency of 1 MHz. This level of amplitudes usually propagates just on the surface of the structure on which we are applying the force and, therefore, they can only be detected with high sensitivity sensing systems.

The study of the structure integrity and its health is performed in the discipline called Structural Health Monitoring (SHM) [1]. SHM is a field that studies the integrity of a structure that is under stress to determine whether it is safe, or it will collapse and thus be unfit for any use until maintenance work is done. The presence of superficial cracks can also magnify the probability of collapse of the structure under test and, therefore, the superficial vibrations can magnify the distress of the cracks. At the same time, the cracks can increase due to periodic expansions and contractions of the surface and thus lead to eventual break.

Electronic sensors, such as strain gauges and PZT transducers, allow point measurements that are difficult to extend over long distances or even to operate in locations with electro-magnetic interference or in chemically harsh environments. As a result, their use in industrial applications is limited and their performance is highly dependent on the characteristics of the environment.

Fiber optic sensors, on the other hand, are suitable devices for these applications, as they have a geometry that allows them to be deployed over long distances and to measure accurately and with high resolution. More specifically, fiber Bragg grating (FBG) sensors have been used to measure strain and temperature. They are composed of a diffractive pattern that is inscribed in the fiber core and makes them behave like optical filters whose central wavelength (Bragg wavelength) changes if mechanical stimuli are applied to it. There are several types of FBG sensors [2], [3] such as uniform FBG, chirped FBG and random fiber gratings among others. The interrogation of these sensors with optical sources makes it possible to extract their optical properties and to measure other physical parameters applied to the sensor, such as strain or temperature.

Optical frequency combs are sources composed of several optically coherent tones that are spaced a certain width apart. They are a key component to generate more advanced sources such as dual optical frequency combs [4]–[7] or self-heterodyne combs, which are multiheterodyne sources that have an electrical mapping from the optical domain. This electrical mapping allows to extract their attenuation with respect to the wavelength once they have passed through the optical sensor. Thus, strain information can be extracted directly through the electrical frequency domain.

The motivation of this doctoral thesis is to measure and calibrate the small vibrations that happen on the rigid and solid surfaces with techniques that involve special optical sources that are multiheterodyne and optical fiber sensors, such as FBG and random fiber gratings.

Electro-optic dual optical frequency combs are flexible sources that offer advanced interrogation of sensors whose output is based on wavelength shifting or wavelength filtering, such as FBG sensors. In this thesis, a first FBG interrogation system with these features is presented. It allows to properly select and adjust parameters of the multimode optical source, such as the number of modes and their position within the reflected spectrum of the FBG, and a direct readout is obtained. This scheme is proposed for the measurement of fast phenomena and is demonstrated with 2 kHz vibrations and 40 kHz and 120 kHz ultrasound.

On the other hand, a compact multiheterodyne source is generated with a dual-drive Mach Zehnder modulator [8]–[10] and this arrangement is used to interrogate weak FBG sensors with a dispersion interferometer. The source and the sensing system are tested with up to 135 kHz mechanical vibrations and they are calibrated against a fiber optic heterodyne interferometer.

Self-heterodyne combs are based on a feedback acousto-optic modulator that generates a comb shifted with respect to the seed laser [11], [12]. If mixed with the seed laser they generate a multiheterodyne signal that has the information of the optical tones. This tool is used in this thesis to read random fiber gratings and makes it possible to detect 1 MHz mechanical vibrations.

1.2 Objectives

The aim behind this thesis is to measure and calibrate ultrasonic and acoustic mechanical vibrations by using optical multiheterodyne sources and optical fiber sensors. The main objectives associated to this research are:

- Simulate and analyze the behavior of the multiheterodyne sources
- Develop and implement multimode multiheterodyne sources based on compact implementation to read fiber Bragg grating sensors
- Evaluate and compare those new techniques with more classical ones in terms of best resolution and maximum frequency response as well as to discuss principles of operation and their properties.
- Demodulate and extract the vibration information from sensors like uniform FBG, low reflectivity FBG, random fiber gratings and chirp FBG.
- Implement a self-heterodyne readout for random fiber grating devices

1.3 Research context and collaborations

I would like to thank the economical supports of this work: the *Ministerio de Educación, Cultura y Deporte* (Spain) for the *Formación de Profesorado Universitario* FPU2016: FPU16/03695 grant and PARAQUA project (TEC2017-86271-R), as well as the *Ministerio de Ciencia, Innovación y Universidades* (Spain), *Ayudas de movilidad* EST18/00617.

The means used are those of the Sensors and Instrumentation Techniques (SIT) group of the Electronic Technology Department, University Carlos III of Madrid, Spain, as well as those of the Fiber Optics Group of the Physics Department, University of Ottawa, Canada, during my research stay.

1.4 Structure of the thesis

The structure of this thesis is organized in nine chapters that cover the whole structure from the state of the art that is discussed on chapters two and three, simulation of the multiheterodyne sources that is discussed in chapter four, design and characterization of the employed

instrumentation systems discussed in chapters five, six, seven and eight as well as the discussion, conclusions and future work that are disclosed in chapter nine.

- Chapter 1: Introduction and objectives
    - In this chapter, the goals of the thesis, the motivation, and a summary of the contributions through conference and journal papers are included.
- Chapter 2: Interferometry and electro-optic frequency combs
    - This part presents the types of interferometers and their operating regimes. Those are the key structures that will appear in the following chapters. The different types of multiheterodyne sources that will be used throughout the thesis are also presented.
- Chapter 3: Optical fiber and fiber Bragg grating sensors
    - In this part, different fiber sensors based on a diffraction pattern inscribed in the core are presented. Fiber Bragg gratings are shown to be a key component of the instrumentation system for fast dynamic strain measurement. Uniform FBG, chirped FBG and random fiber gratings are introduced.
- Chapter 4: Simulation of multiheterodyne sources
    - This part shows how electro-optical topologies and acousto-optic topologies are numerically simulated with the operating equations. Typical behavior is discussed, and main parameters are shown.
- Chapter 5: Electro-optic dual optical frequency comb for fiber Bragg grating readout
    - It presents a system based on uniform FBG sensors and an electro-optic dual optical frequency comb. The interrogation method is proposed to detect fast phenomena with the FBG sensor. It shows the implementation with an acousto-optic frequency shift and the demodulation system. The experimental results focus on the measurement of vibrations and ultrasound signals. Finally, a generalization of this interrogation configuration is discussed.
- Chapter 6: Phase generated frequency shifted dual comb implementation
    - In this chapter, a new implementation of the dual-comb architecture using serrodyne phase modulation is proposed for frequency shifting. It is also generalized to the use of a phase generated carrier. This chapter also shows the working principle of multiheterodyne generation by a single device and its characterization through reading the absorption line on an HCN cell. The

experiment demonstrates injective mapping from the optical domain to the electrical domain of this new approach.

- Chapter 7: Acousto-optic self-heterodyne readout of grating sensors
    - This chapter presents the readout of random fiber gratings using a self-heterodyne comb architecture. This interrogation system is also tested with uniform FBG. Measurements of ultrasounds are performed, and frequencies of 1 MHz are achieved. Characterization against a heterodyne interferometer is included.
- Chapter 8: Compact interrogation of grating sensors based on multiheterodyne dispersion interferometry for dynamic strain measurements
    - This part presents the readout in dispersion regime of an FBG sensor. The sensor is interrogated with a source generated with a dual-drive Mach-Zehnder modulator and by means of a dispersion interferometer. It is applied to ultrasound measurement with weak FBG by using lock-in detection. A generalization using phase shift interferometry demodulation is also included.
- Chapter 9: Conclusions and future work
    - In addition to the main conclusions of the thesis, it presents the extension capabilities of the proposed multimode multiheterodyne technique to multiwavelength operation.

Chapter 2: Interferometry and electro-optic frequency combs

"And God said, “Let there be light,” and there was light. And God saw that the light was good. And God separated the light from the darkness."- (Genesis 1:3)

2.1 Introduction

This chapter discusses the importance of the interferometry field and the optical frequency comb paradigm.

Firstly, the concept of light is introduced as a tool for measuring. The interferometry field is defined and the state-of-the-art of different interferometers are presented and discussed in terms of characteristics and performance.

Afterward, the light sources are discussed and the concepts of broadness and wavelength tunability are also presented. Light modulation is exposed and the relationship between modulation and optical frequency combs is presented.

Finally, electro-optic dual optical frequency combs are presented as well as their relationship with the interferometric systems. The injective mapping from the optical domain to the electric domain is briefly discussed. Three additional architectures are also introduced: the pseudo-multiheterodyne architecture, the acousto-optic self-heterodyne comb and the phase-generated-carrier dual optical frequency comb. They are explained further in next chapters as part of the systems designed and implemented for this thesis.

2.2 Light as a measurement tool

Light is an electromagnetic wave that can be used to measure. Like other electromagnetic waves, it behaves as a fluctuating function with respect to space and time. The amplitude $a(r)$ depends on the length at which is measured (r) it has a frequency ν which is absolute in all the media and a phase $\phi(r)$ which also depends on the position which is considered and the wavelength λ. If real-valued [1] functions are considered the plane wave monochromatic behavior can be expressed as (1).

$$u(r,t) = a(r)\,cos\,\left(2\pi\nu t + \phi(r)\right) = a\;cos\;(2\pi\nu t - 2\pi x/\lambda) \tag{1}$$

In most cases, the light is detected by its power magnitude. Which, in the case of the eye and regular photodetectors, is described as a square law (2).

$$I(r,t) = 2\langle u(r,t)^2\rangle \tag{2}$$

When light travels through a certain media its properties change. Those properties can be the phase, the amplitude, the pulse width, the frequency among others [2].

On the other hand, the real function described in (1) can be expressed as complex notation (3):

$$U(r,t) = \alpha(r)e^{j\phi(r)}e^{j2\pi\nu t} = U(r)e^{j2\pi\nu t} \tag{3}$$

The electrical field complex notation leads to a similar expression for the power of an electrical field (4):

$$I(r) = \|U(r)\|^2 = U(r)^* U(r) \tag{4}$$

If the complex form is plugged into the general form of the wave equation, it leads to the Helmholtz equation [1] and specifically to a very important parameter of the light which is the wavenumber (5).

$$k = \frac{2\pi\nu}{c} \tag{5}$$

where ν is the fluctuating frequency and c is the light speed in the medium. However, as light speed depends on the media it can be shown that the speed is inversely proportional to the index of refraction of the media (n) as (6).

$$c = \frac{c_0}{n} \tag{6}$$

where c_0 is the speed of the light in the vacuum. Therefore, the length period known as the wavelength is defined in (7).

$$\lambda = \frac{c}{\nu} \tag{7}$$

2.3 Optical interferometers

Interferometry is the science field that uses light and makes it interfere to recover phase difference between two or more light beams. The process of superposing the beams is dependent on several conditions. The most important are:

- The wavelength of the beams
- The polarization of the beams
- Physical and time-domain position overlapping
- Optical time coherence and space coherence

An interferometer is an instrument that divides the light into two or more beams that travel along different optical paths, and which are finally merged into one beam that has the information of the optical paths' differences. Any imbalance between the arms is translated to an optical phase difference and, therefore, analyzed through the characteristics of the interferogram.

An interferometer can be implemented in either free space, in-fiber, or a mix between both. The main difference is the speed of the light in the medium which in the case of the fiber is near 1.5 times lower than the vacuum case.

If the interferometer is mounted in free space and the interference is projected on the wall optical fringes can be seen with the naked eye. In Fig. 1 concentric circular fringes can be seen of a free-space Michelson interferometer mounted in the laboratory.

The fringes change their intensity if a certain perturbation is applied to one of the interferometer arms. Therefore, clear fringes become dark and vice versa.

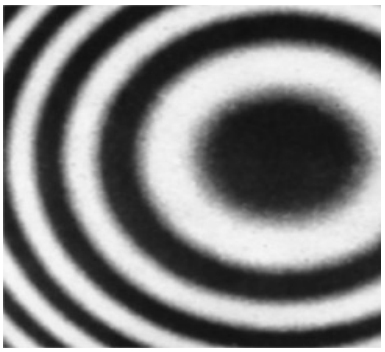

Fig. 1 Interference intensity of a free space interferometer projection taken in the laboratory (free-space Michelson interferometer in 655nm of wavelength).

The interference result is the intensity detected and it is a function of the input optical power and the phase difference between the arms. The detected intensity [3] is of the form of (8):

$$I = I_1 + I_2 + 2\sqrt{I_1 I_2} cos\ (\phi) \tag{8}$$

where I_1 and I_2 are the intensities of the light in the first and second arms of the interferometer. On all the implementations, we can distinguish either homodyne or heterodyne behavior of those metrology instruments. For illustration purposes, if lineal phase modulation is applied over a Mach-Zehnder interferometer a response as the one depicted in Fig. 2 is obtained. And now the fringes can be counted in the time domain (x-axis of Fig. 2) instead of the spatial domain as stated before. The dashed line is the phase modulation applied to the interferometer and the continuous line is the intensity variation of the output of the Mach-Zehnder interferometer. Fringes passing velocity is related to the velocity of phase modulation (slope of the dashed line).

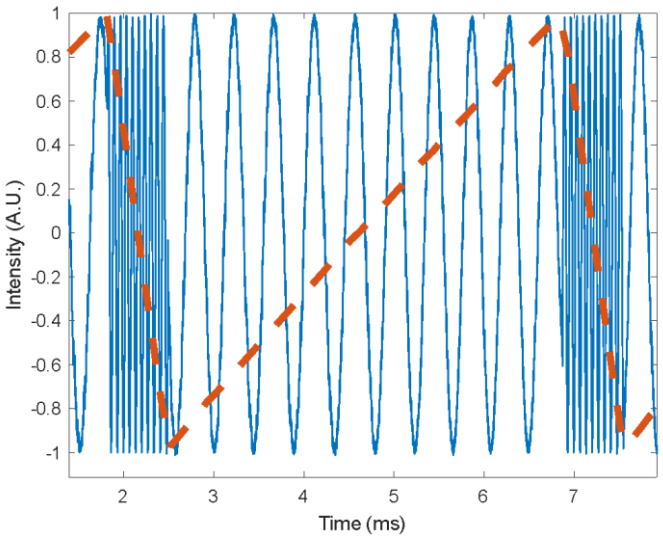

Fig. 2 Mach-Zehnder interferometer response to linear phase modulation for a single-mode fiber implementation. Dashed line: phase modulation, continuous line: the optical intensity output of the interferometer.

2.4 Types of optical interferometers

The Mach-Zehnder interferometer is based on an optical source that is split into two optical paths and afterward, it is merged into one beam utilizing a physically different optical coupler [4]–[6]. The in-fiber implementation can be seen in Fig. 3. The coherent source is split into two beams of equal power employing the first beam splitter then, each beam is directed into its correspondent optical fiber. Both beams are merged into another beam splitter and finally, they are photo detected in the same photodetector.

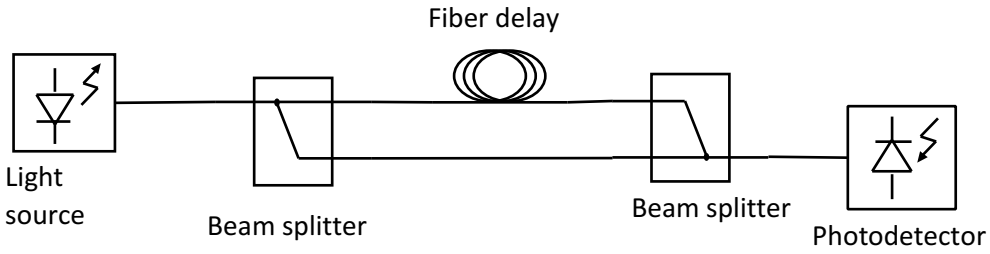

Fig. 3 Mach-Zehnder interferometer; scheme implemented with fiber optic components

On the other hand, in the Michelson interferometer [5], [7]–[11] the same beam splitter is used as a splitter and as a merger at the same time. This reduces the cost of the system. The light is inserted into the splitter, and it is split into two arms with different lengths. Afterward, the light of each arm is independently back-reflected on the terminal reflector placed at the end of this fiber. Finally, it is merged and mixed in the photodetector. It is noteworthy, to observe that the light travels twice the optical fiber as it is reflected by the reflective terminals.

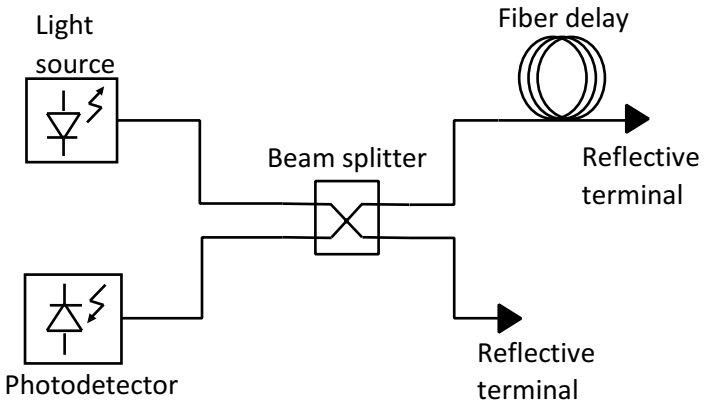

Fig. 4 Michelson interferometer in-fiber implementation

In general, white light interferometry refers to the process of obtaining interference signals from sources that are partially incoherent or have very small coherence. Experimentally it can be shown that the broader the optical bandwidth of the source the more difficult it is to make it interfere. As the coherence length of the source decreases, the path difference of the interferometer needs also to be decreased to obtain an interference signal of good quality.

Particularly, the Michelson and Mach-Zehnder interferometers [15] have the difficulty of exact path matching. However, they are very useful instruments, especially on dispersion measurements [16], [17]. To overcome the disadvantage of fiber balancing interferometers a free space translating stage can be used and considering the pathlength factor difference due to the index of refraction of the air with respect to the fiber.

2.4.1 Interferometer operation regimes

Each interferometer can work in different regimes. We classify them into homodyne, heterodyne, pseudo-heterodyne and multi-heterodyne. That means that a different response to perturbation is achieved depending on the controllable parameters. Those parameters are mainly the frequency modulation, the wavelength, the optical phase modulation and the frequency shift.

When no frequency modulation is applied, both optical paths have the same optical frequency. Therefore, the optical phase difference will be determined by the path difference and the wavelength of the light beam λ as seen in Fig. 2. Therefore, we obtain (9), where d is the path difference of the interferometer. This interferometer will be considered in homodyne regime.

$$I = I_1 + I_2 + 2\sqrt{I_1 I_2} cos\ (\frac{2\pi d}{\lambda}) \tag{9}$$

On the other hand, if frequency difference is imposed between the arms of the interferometer the phase difference will fluctuate with time [18], [29]–[32]. We can obtain (10). This interferometer will be considered in heterodyne regime, also named heterodyne interferometer.

$$I = I_1 + I_2 + 2\sqrt{I_1 I_2} cos\ (2\pi(f_1 - f_2)t + \phi) \tag{10}$$

If the frequency shift is imposed using a piecewise constant derivative phase modulation (saw-tooth signal) a pseudo frequency translation happens. And the response will be similar to (10). However, the limitations on the piecewise negative slope may distort the frequency shift generating a sideband signal with respect to DC [33]–[35]. This interferometer will be considered in pseudo-heterodyne regime, and it is also named pseudo-heterodyne interferometer in the literature.

When injecting two wavelengths into an interferometer several considerations can be made. If they are close enough for the frequency difference to lie inside the detector bandwidth, we will see the frequency difference as a harmonic in the electrical domain. This is the case of the heterodyne interferometer case explained before. However, if another wavelength is injected into the interferometer and both wavelengths are heterodyned at different frequencies [36], an expression of the electrical frequency can arise (11).

$$I = a + a_1 \cos\left(2\pi \Delta f_1 t + \phi_1\right) + a_2 \cos\left(2\pi \Delta f_2 t + \phi_2\right) \tag{11}$$

where Δf_1 and Δf_2 are the heterodyning for the first wavelength and the second wavelength. However, an interesting generalization arises if multiple wavelengths are coherently inserted into the interferometer. Each pair of wavelengths, whose frequencies are f_i and f_j, will generate an electrical signal with frequency the difference between both $(f_i - f_j)$, which can be easily detected in a photodetector with sufficient bandwidth.

Therefore, the expression that arises is of the form of (12). [37], which has intrinsically the information of the optical powers of both wavelengths $I_i I_j$, as well as the optical phase difference between both $2\pi(f_i - f_j)t + \phi_{i,j}$.

$$I \propto \sum_{i=1, j=1 \; \forall \; i \neq j}^{N} \sqrt{I_i I_j} \cos\left(2\pi(f_i - f_j)t + \phi_{i,j}\right) \tag{12}$$

The important consequence in this generalized formula is that the optical phase change between optical tones is readable by the electrical phase and the optical amplitude $I_i I_j$ is readable from electrical amplitude. The process that generates this intensity is often called a “beat” of tones or a mix of tones.

More generally the multiheterodyne process consists of multiple pairs of tones that generate a beat in the electrical domain and therefore constitute an electrical mapping of each independent pair of modes.

2.5 Optical frequency comb spectroscopy

Spectroscopy is the science field that determines the interaction of any electrical field with the media. This is intended to measure media properties. Those can be a strain, temperature, pressure, index of refraction, concentration, length among others.

For performing spectroscopy, we can inject all of the understudy wavelengths (frequencies) into our sample and read all that data with an optical spectrum analyzer (OSA). The broadband sources are devices that continuously generate those wavelengths, they are not coherent, and they do not interfere typically unless path matching conditions are fulfilled. If detected with a photodetector, all the wavelengths are integrated as a unique electrical signal and no distinction can be made between each one of the wavelengths.

Tunable laser sources can be used to do spectroscopy as they allow us to sweep over a certain interval of wavelengths by just changing a certain controlling input. Therefore, a relationship between time and wavelength can be found. This allows us to determine the media behavior to the wavelength and therefore it allows us to perform spectroscopy techniques.

Fig. 5 shows the typical behavior of a tunable laser for illustrating purposes. As the current increases the wavelength increases as well.

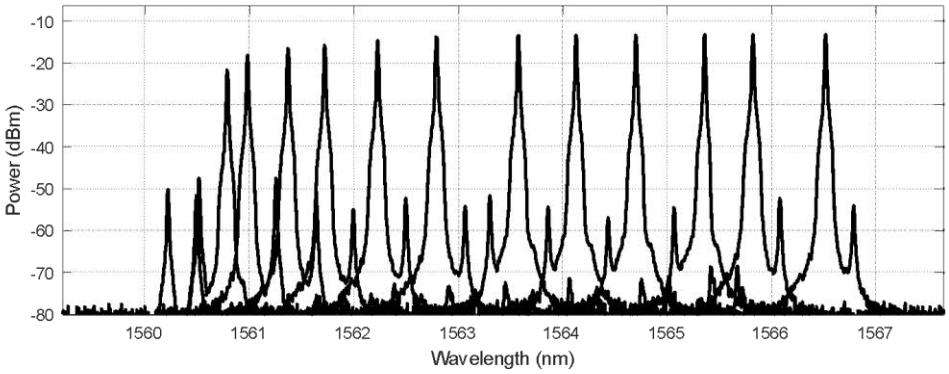

Fig. 5 Response of a VCSEL as a tunable laser: wavelength versus injection current. Lower wavelengths correspond to lower injection current and higher wavelengths correspond to higher injection currents. Current swipe from 2 mA to 14 mA. The total span is 6 nm.

The optical frequency comb [13]–[17] is a set of tones that are equally spaced along the spectral axis. As a result, several wavelengths are spread over the optical domain. Those have their frequency amplitude and optical phase. It behaves conceptually as a broadband source however it is composed of a set of discrete wavelengths that are uniformly distributed over the optical domain. The photodetection process is known to be proportional to the square of the electrical field. Hence the detection leads to the cross beat between each mode with the other ones.

Therefore, the electrical frequency domain is a lateral band with respect to DC. The arrangement of the lines is represented in Fig. 6 a) in the case of the optical domain, and Fig. 6 b) in the case of an electrical photo-detected signal. Optical frequency combs can be generated in a huge variety of ways: Micro-resonator based [38], [39], Gain switching [40], [41], mode-locking [42], electro-optic [43] generation, acousto-optic combs [44], etcetera. However, the most used in this thesis is the electro-optical comb, which has several advantages that will be discussed in further sections.

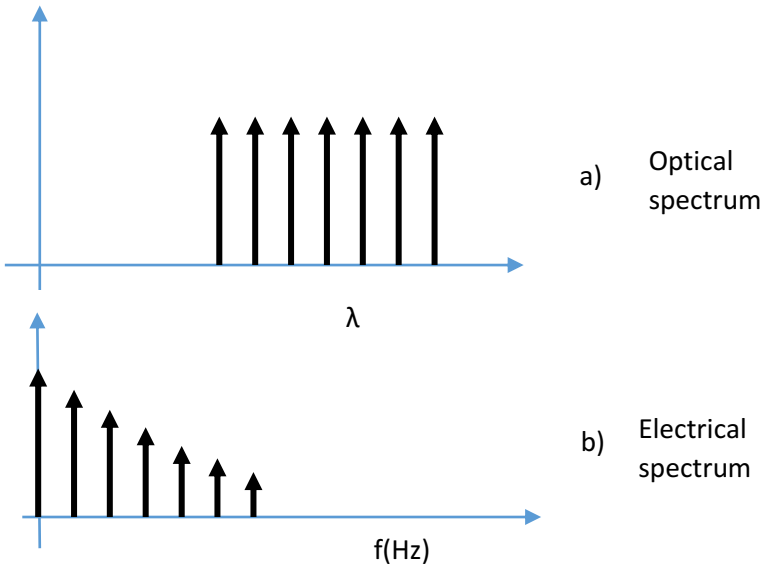

Fig. 6 Optical frequency comb in the optical domain of wavelengths a) and electrical domain b).

2.5.1 Optical frequency comb generation

I. The (phase) electro-optic modulator

The phase electro-optic modulator is a device usually made of lithium niobate compounds. And allows the output light to be shifted in phase a certain amount which is controllable by the electrical input signal. The change in phase on the output electrical field can be expressed as a formal multiplication between the input electrical field phasor and a unitary phasor that is phase-shifted a certain amount (13).

$$E_0(t) = E_i(t)\left(e^{j\phi_1(t)}\right) \tag{13}$$

The output field has ideally the same amplitude as the input one however is shifted according to (14):

$$\phi_1(t) = \frac{\pi n_0^3 L V(t)}{\lambda D} = \pi \frac{V(t)}{V_\pi} \tag{14}$$

where n_0 is the refractive index, r is a constant which depends on the material, L is the length of the active area of the device, λ is the wavelength of the input light beam, D is the separation between the electrodes and the modulation pins and $V(t)$ is the arbitrary function applied to the modulation pin of the device.

II. The (amplitude) Mach-Zehnder modulator

The amplitude modulator or Mach-Zehnder modulator is an electro-optical modulator that transforms internally changes of phase electrically induced to changes in amplitude. They are built internally as Mach-Zehnder modulators that allow a transformation of phase modulation electrical field of one of the arms into amplitude modulation.

The output field $E_i(t)$ is split into two electrical fields of equal amplitude and then one is phase modulated ($e^{j\phi_1(t)}$ term of (15)) and the other is not modified (unitary term of (15)). Finally, they are added together. This process is done according to (15):

$$E_0(t) = \frac{1}{2}\left(1 + e^{j\phi_1(t)}\right)E_i(t) = cos\ \frac{1 - \phi_1(t)}{2}\ E_i(t)e^{\frac{j\left(1+\phi_1(t)\right)}{2}} \tag{15}$$

where $\phi_1(t)$ is the phase modulation described in (*14*).

III. The dual-drive Mach-Zehnder modulator

The dual-drive Mach-Zehnder modulator is a much more general device it allows phase and amplitude modulation at the same time in a single device. It is built like an amplitude modulator but with both arms available for phase modulation. Therefore, the output signal is equal to the input signal multiplied by the sum of two phasors each one representing the process of splitting the signal into two beams then, the independent modulation phase $\phi_1(t)$ and $\phi_2(t)$.

$$E_0(t) = \frac{1}{2}\left(e^{j\phi_1(t)} + e^{j\phi_2(t)}\right)E_i(t) \tag{16}$$

By manipulating (16) with the common factor $e^{\frac{j\left(\phi_1(t)+\phi_2(t)\right)}{2}}$ we can obtain the general form of simultaneous phase and amplitude modulation as (17).

$$E_0(t) = e^{\frac{j(\phi_1(t)+\phi_2(t))}{2}} cos\ \frac{\phi_1(t) - \phi_2(t)}{2}\ E_i(t) = A(t)E_i(t)e^{j\psi(t)} \quad (17)$$

where the phasor $A(t)e^{j\psi(t)}$ is modifying the field phasor $E_i(t)$.

IV. Relationship between optical frequency combs and modulators

The relationship between optical combs and electro-optic modulators lies on (18) for the particular case in which the phase modulation $\phi_1(t)$ is a periodic function of period $1/\omega_m$ and $E_i(t)$ is a periodic function. Considering the Jacobi-Anger expansion [45], (18) is the harmonic decomposition of a phase-modulated complex phasor. Therefore, it can be shown that infinite modes are generated of $J_n(z)$ amplitude each.

$$e^{iz\ sin\ (\theta)} = \sum_{n=-\infty}^{\infty} J_n(z)e^{in\theta} = \sum_{n=-\infty}^{\infty} \left(\frac{1}{2}z\right)^n \sum_{k=0}^{\infty} \frac{\left(-\frac{1}{4}z^2\right)^k}{k!\,\Gamma(n+k+1)} e^{in\theta} \quad (18)$$

However, in practical cases, as n tends to infinity and z is a real number greater than zero, the value of $J_n(z)$ is very low compared to the low-order harmonics. And consequently, when reading with an optical spectrum analyzer, the harmonics lie below the noise floor leading to a finite width optical frequency comb. $\Gamma(x)$ denotes the Gamma function. The numerical values of $J_n(z)$ can be seen in Fig. 7.

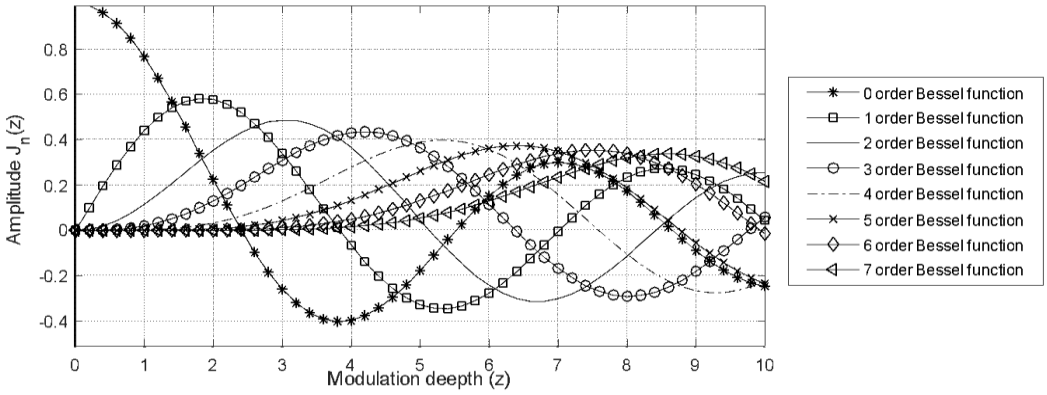

Fig. 7 Bessel functions of the first kind, order n and argument z.

Similarly, if we measure the relative amplitude of the optical modes of an optical frequency comb with the optical spectrum analyzer and we can see that there is a correspondence between the theoretical values from Fig. 7 and Fig. 8. The zeros of the experimental obtained Bessel functions

are at 28 dBm, 32 dBm and 35 dBm, for the first, second and third-order of the first kind Bessel functions, which correspond to z=2.4, z=3.9 and z=5.1. Hence, using (20) and assuming a matching impedance of 50Ω, the V_π of the EOM can be calculated as approximately as V_π =2.35V. Note that the amplitudes of (15) are always positive and the 1st mode corresponds to the 0 order Bessel function.

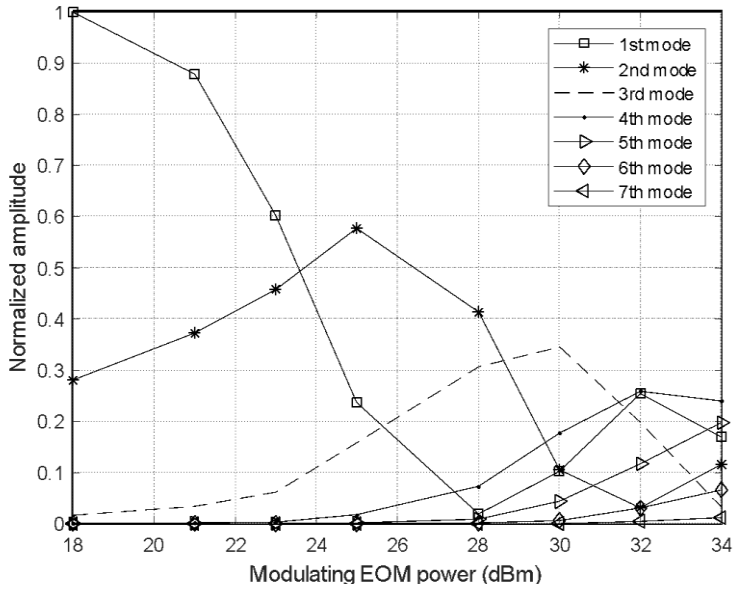

Fig. 8 Measured amplitudes of an optical frequency comb in terms of the phase modulating signal.

Another functional relationship may be established between dual-comb interferometry and two-wavelength interferometry. The arbitrary electrical field amplitude and phase of each tone are obtained in the electrical domain as an electrical tone for each pair of optical tones [36]. Fig. 9 shows a conceptual equivalence between the multimode multi-heterodyne source. Each pair of homolog tones can be seen as an individual generation entity as a heterodyne interferometer. However, the main difference is that the electro-optic dual optical frequency comb does not have an arbitrary phase and amplitude. Therefore, the amplitude of the generated tones depends on the phase sideband generation signals.

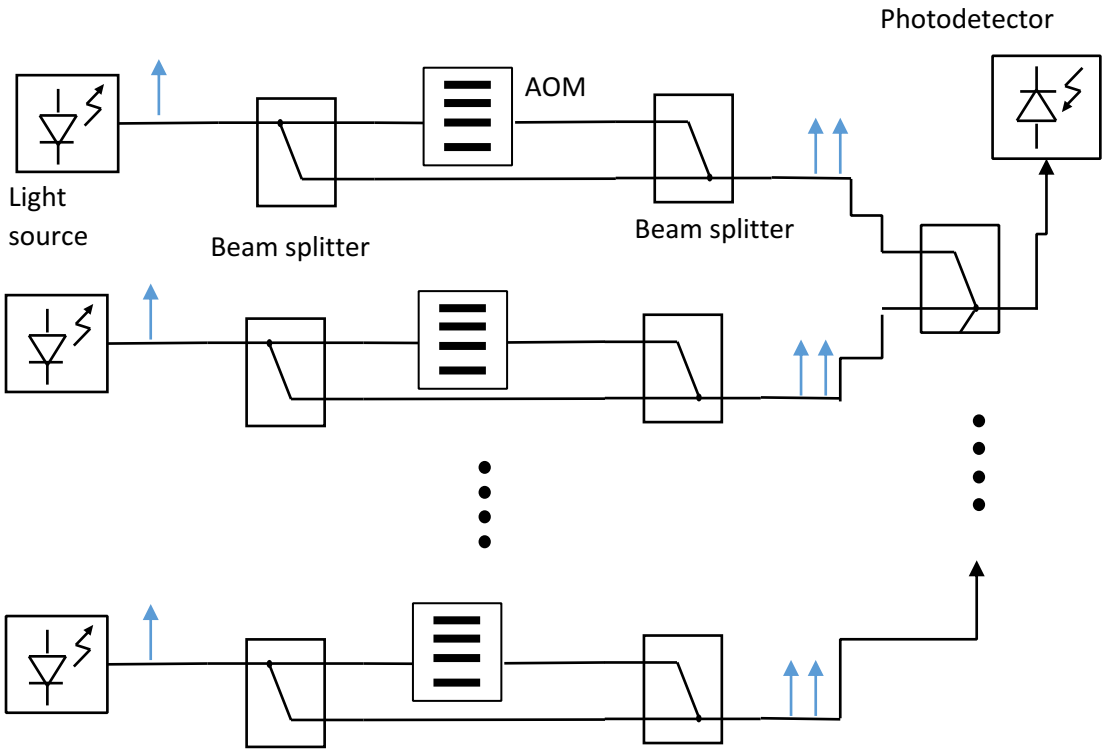

Fig. 9 Functional implementations of multiheterodyne source into a photodetector.

2.6 The electro-optic dual optical frequency comb

A dual optical frequency comb is an extension of the use of an optical frequency comb. Two combs with different repetition rates and different central frequencies are overlapped and are made to interfere to obtain a multi heterodyne source. The concept is similar to the dual-wavelength interferometry described in the earlier section. However, the main difference is that in the case of dual combs several optical tones are overlapped and heterodyned with respect to its homolog on the other comb. The process is done by steps and in the electro-optic case, it is done with a seed laser in a continuous wave domain. The light beam is divided, one of the beams is shifted with respect to each other and then modulated for the comb generation. Finally, the beams are merged, and the resulting signal is photo detected. This procedure is depicted in a scheme in Fig. 10. The acousto-optic modulator (AOM) does the shifting process. And the comb generation is done by the electro-optic modulator [46], [47].

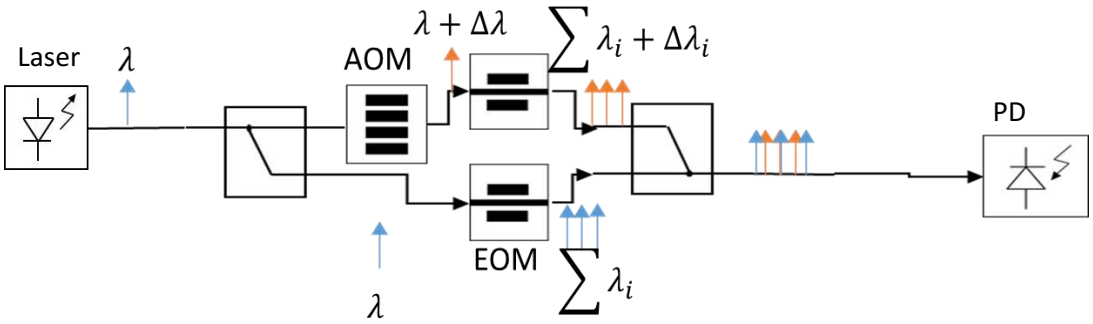

Fig. 10 Classical architecture of electro-optical dual optical frequency comb.

The output of the dual optical frequency comb is the overlap of two combs that are slightly shifted from each other and they have different repetition rates Fig. 11 a), this provokes that the frequency of each pair of homolog tones has different frequency separation which coincides with the electrical mapping frequency Fig. 11 b).

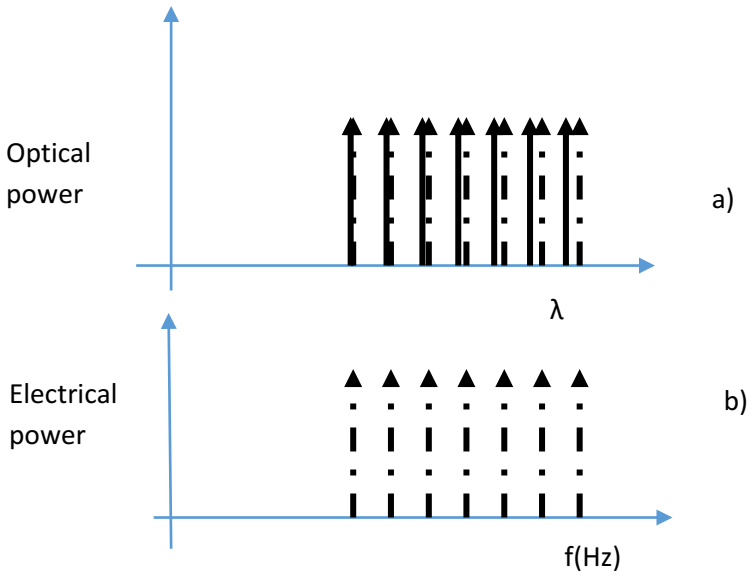

Fig. 11 Multi heterodyne process a) optical spectrum of a multiheterodyne source b) electrical spectrum of a multiheterodyne optical source.

There are several parameters that have to be considered when generating the dual optical frequency combs, which are depicted in Fig. 12, where f_{pm1} is the frequency of the modulation of the first electrooptic modulator, f_{pm2} is the frequency of the modulation of the second electrooptic modulator, f_{shift} is the frequency shift imposed by the acousto-optic modulator and f_0 is the frequency of the laser seed.

In Fig. 12 a) we can observe two optical combs generated at different frequency rates and with the same center frequency. In Fig. 12 b) we can observe two optical frequency combs at different frequency rates and with different frequency centers. It is noteworthy to mention that $f_{pm1} - f_{pm2} << f_{pm1}, f_{pm2}$ and $f_{shift} << f_{pm1}, f_{pm2}$ to achieve an unambiguous mapping process.

Finally, in Fig. 12 c) we can observe the electrical image of the combs depicted in Fig. 12 b).The separation between the electrical modes coincide with fpm1-fpm2 value.

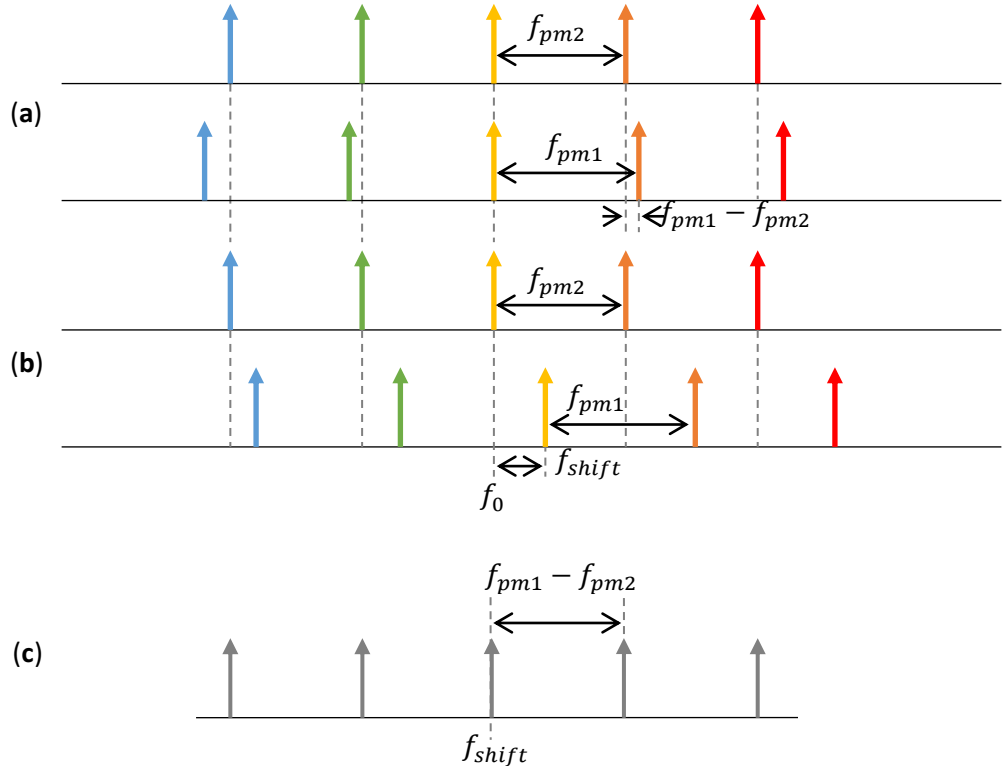

Fig. 12 Representation of the multiheterodyne process that happens in the dual optical frequency comb generation.

The response of those kinds of systems are similar to the one depicted in Fig. 13. In Fig. 13 a) it is shown the optical response of a dual comb implementation in black line and in red line it is shown the seed laser that is used to generate the optical source. In Fig. 13 b) it is shown the electrical response of a dual comb implementation. By injecting the optical source (Fig. 13 a)) into an absorption sample we can recover the shape of that absorption by just registering the amplitudes seen in the electrical domain (Fig. 13 b)).

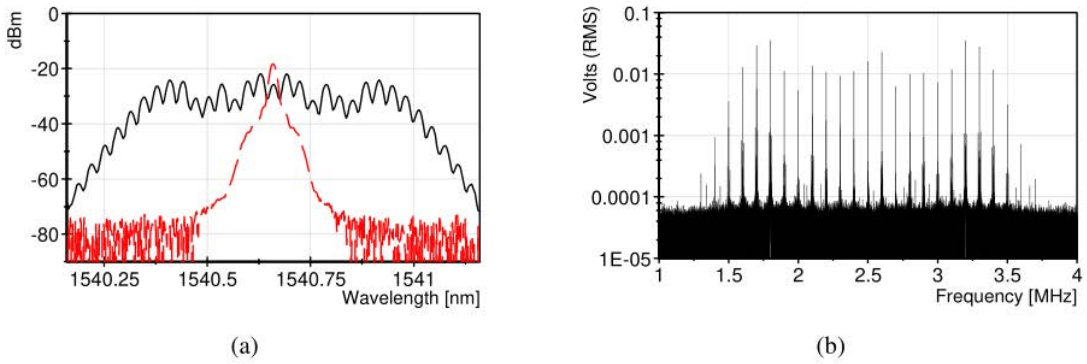

Fig. 13 Typical response of a dual comb multiheterodyne source implementation.

2.7 The pseudo-multiheterodyne architecture

When using just two electro-optic modulators we can inject another modulating signal in order to generate a pseudo carrier in electrical domain. That is done with a sawtooth signal applied to one of the electrooptic modulators. The system can be seen in Fig. 14. It is composed by a laser source that generates a light beam that is split into a Mach-Zehnder interferometer whose arms are modulated in phase by two sinusoidal signals at different frequency rates and a sawtooth signal.

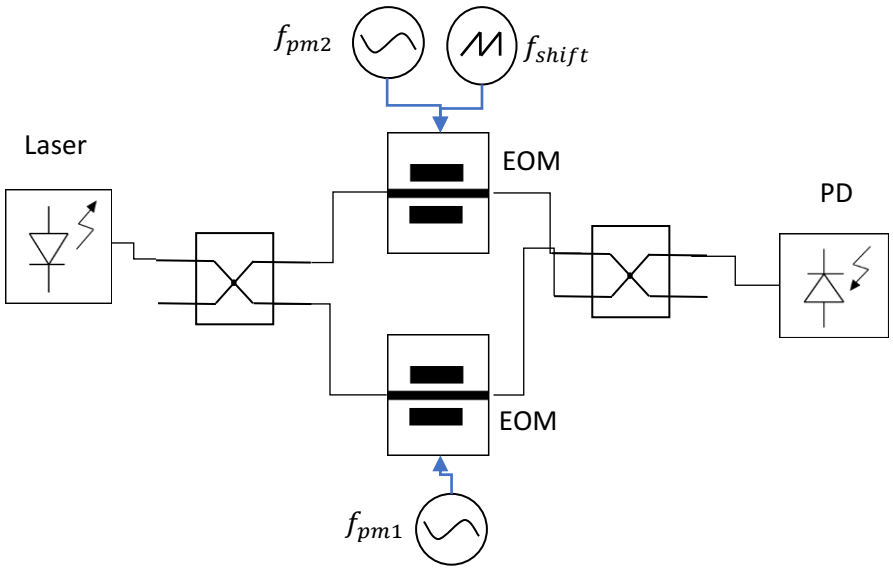

Fig. 14 Setup of a pseudo-multiheterodyne source.

The behavior of the optical modes is depicted in Fig. 15 a) and the electrical mapping is depicted in Fig. 15 b). The frequency of the electrical carrier is determined by the parameters of the

sawtooth signal applied to one of the arms of the interferometer. It is noteworthy to mention that $f_{pm1} - f_{pm2} << f_{shift}$.

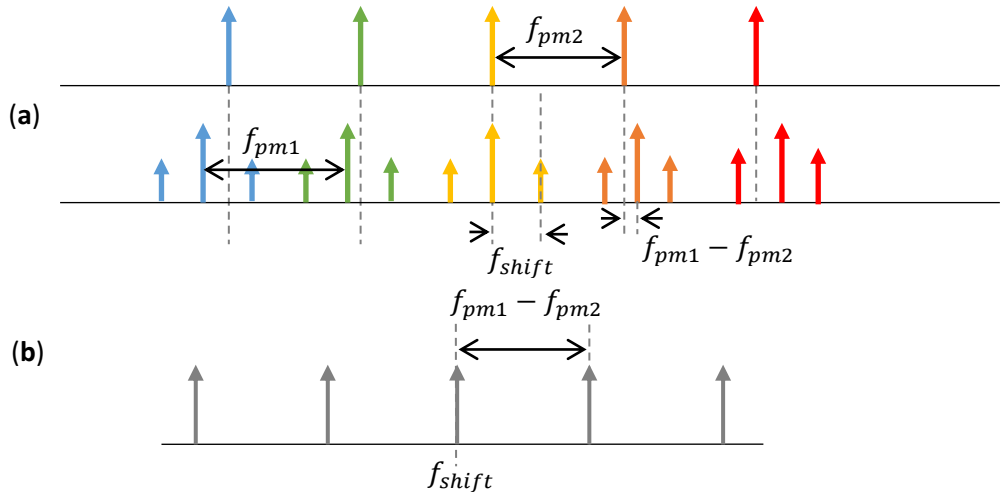

Fig. 15 Scheme of the position of the optical lines of a pseudo-multiheterodyne setup a), position of the electrical lines in the pseudo-multiheterodyne source b).

2.8 The acousto-optic self-heterodyne comb

This arrangement consists of feedbacking an acousto-optic modulator to generate a set of optical tones spaced an amount equal to the modulation frequency of the acousto-optic modulator. The setup is shown in Fig. 16.

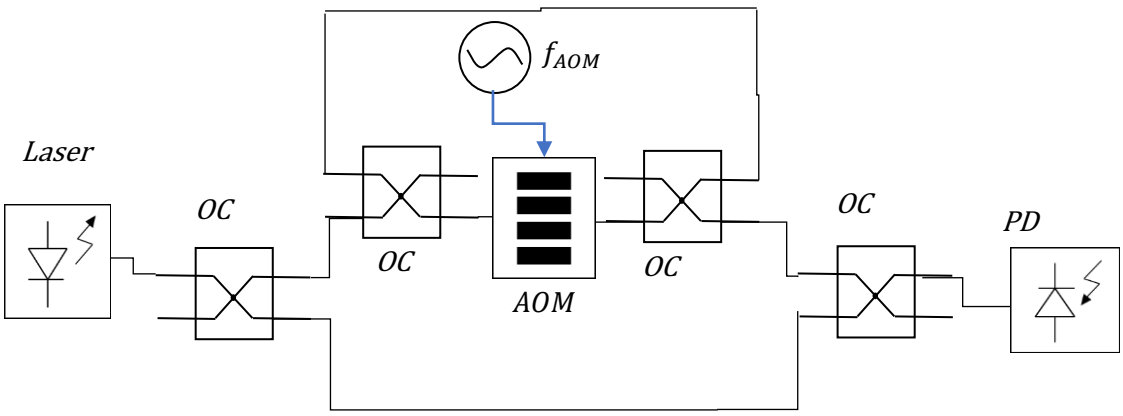

Fig. 16 Setup of an acousto-optic self-heterodyne comb.

The behavior of this kind of multiheterodyne sources consist of an optical comb that is mixed directly with the optical source. This process is shown in Fig. 17 a) in optical domain and in Fig. 17 b) in electrical domain. In this case the multiheterodyne beat does not happen between two optical combs but between an optical comb and the optical line of the seed laser. In this case the optical spacing and the electrical spacing is the same in both cases.

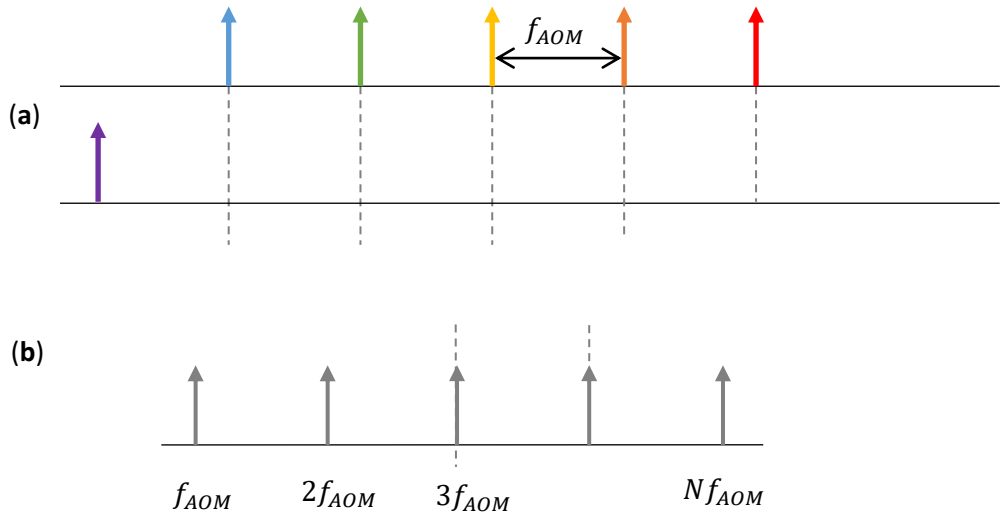

Fig. 17 Position of the optical modes of a self-heterodyne acousto-optic comb a), position of the electrical mapping of a self-heterodyne acousto-optic comb b).

2.9 The phase-generated-carrier dual optical frequency comb

The phase-generated-carrier (PGC) demodulation of an interferometer is intrinsically a multi-heterodyne structure [18]. On the other hand, the main carrier can be used as a frequency shift, similarly to the pseudo-heterodyne architecture. The PGC dual comb is generated by two signals of different frequency applied to a dual drive Mach Zehnder modulator and by a third signal applied to the seed laser that slightly modulates its frequency. This process is shown in Fig. 18.

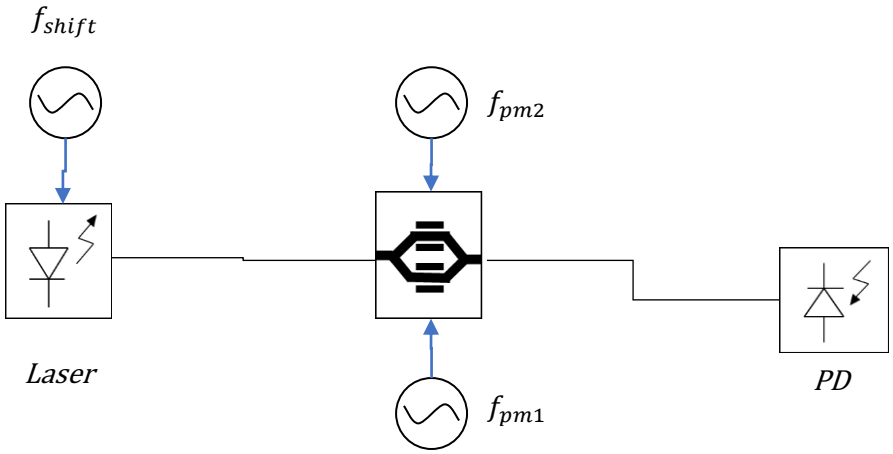

Fig. 18 Setup of the PGC dual comb.

In this case the repetition rate of the laser modulating signal determines the electrical frequency rate at which the comb is repeating in the electrical domain. While the frequency difference between the phase modulator signals is determining the electrical spacing of the lines of each comb image. This process is shown in Fig. 19 a) in optical domain and in Fig. 19 b) in electrical domain. It is noteworthy to mention that $f_{pm1} - f_{pm2} << f_{shift}$.

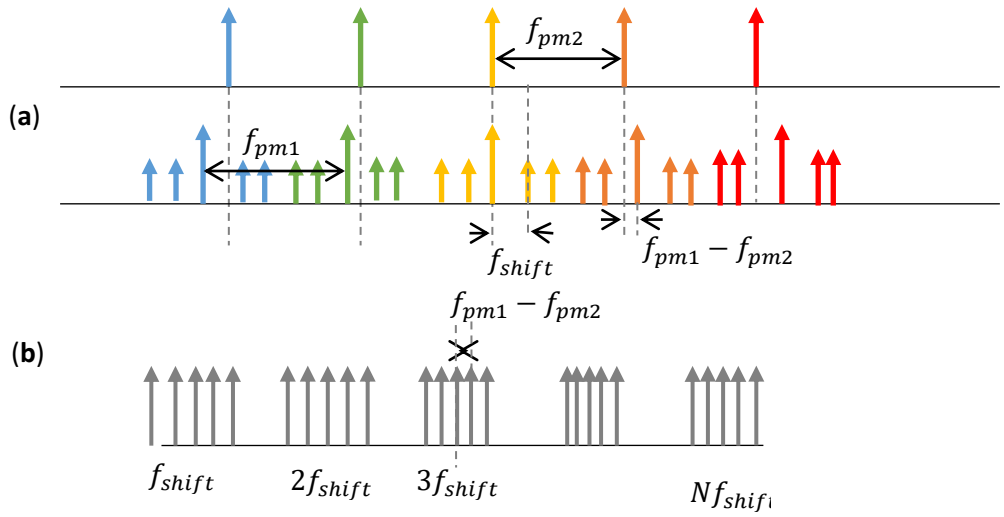

Fig. 19 Position of the optical modes of a multiheterodyne PGC comb a), position of the electrical mapping of a multiheterodyne PGC comb b).

2.10 Conclusions

This chapter summarizes the basic concepts of optical interferometry, optical frequency combs, and multiheterodyne detection as the tools that we used in this thesis. We have presented the field of interferometry and its application to generate optical frequency combs and multimode multiheterodyne sources based on dual-comb techniques. All those optical sources allow wavelength spectroscopy, and they are the key components in the next chapters for interrogating fiber optic sensors, such as fiber Bragg grating sensors and random fiber grating sensors. High throughput systems are going to be presented that can detect fast phenomena.

Chapter 3: Optical fiber and fiber Bragg grating sensors

“There are only two ways to live your life. One is as though nothing is a miracle. The other is as though everything is a miracle.”- Albert Einstein

3.1 Introduction

This chapter presents a general overview of the optical fiber and the fiber grating sensors. We comment on the basic physical morphology of the optical fiber and the roles of absorption and dispersion in the optical fiber.

Afterward, we briefly introduce the fiber grating sensors, the different kinds of diffractive patterns and their different behavior in terms of absorption and dispersion for the basic interrogating types.

We finally discuss the concept of depth penetration in chirped kind fiber Bragg grating sensors.

All these concepts are used further in the thesis and their importance arises when we combine them with the tool of the optical frequency comb, as they are discussed in chapters 5, 7 and 8.

3.2 Optical fiber

Optical fiber is a geometrically cylindrical component that allows the light to travel and be confined through a determined optical path it is composed of cladding and a core [19], [20]. Both have a different refractive index, which is greater in the case of the core and smaller in the case of the cladding. As seen in Fig. 20. We use single mode fiber along all the thesis implementation and step index fiber. This fiber type is propense to the polarization changes of the light and therefore all the setups should be placed on a stable optical table and to contain a polarization controlling unit.

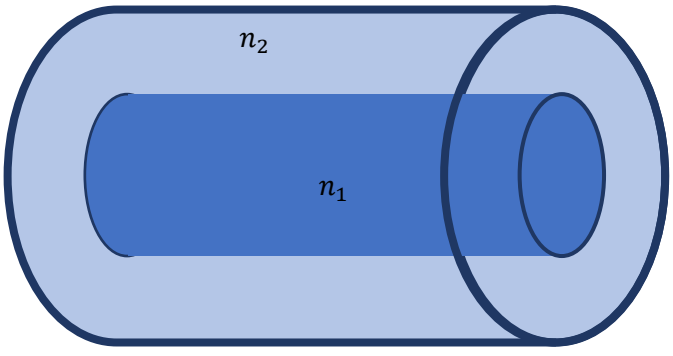

Fig. 20 Geometrical scheme of optical fiber.

When light travels through a medium the power of the electrical field is diminished as it travels in the media due to the inhomogeneous structure of the material. This coefficient is assumed constant and is expressed as (19) and it is known as attenuation

$$\alpha = \frac{1}{L} log_{10} \frac{P(0)}{P(L)} \tag{19}$$

where $P(0)$ is the power at the beginning of the media, in this case, the optical fiber and $P(L)$ is the optical power at the length L of the fiber.

Moreover, when light is traveling along optical fibers, it is affected by attenuation and dispersion. Attenuation affects the amplitude of the electromagnetic wave while dispersion acts on the group velocity of each wavelength component of the light beam. If a light beam is modulated in amplitude and injected into an optical fiber as a pulse stream, the pulses spread by consequences of the difference of group velocity between wavelengths.

There are mainly four types of dispersion [21]: Modal dispersion, material dispersion waveguide dispersion and nonlinear dispersion.

- Modal dispersion: it happens on multimode fibers due to differences in the group velocities of each one of the traveling modes.
- Material dispersion: in which the refractive index is a function of the wavelength
- Waveguide dispersion: it is dependent on the morphology of the core. Even though the material is nondispersive, the ratio between the wavelength and the radius of the optical fiber induces delays on each particular wavelength.
- Nonlinear dispersion: it happens when the power of the light is so high that the index of refraction depends on the input power.

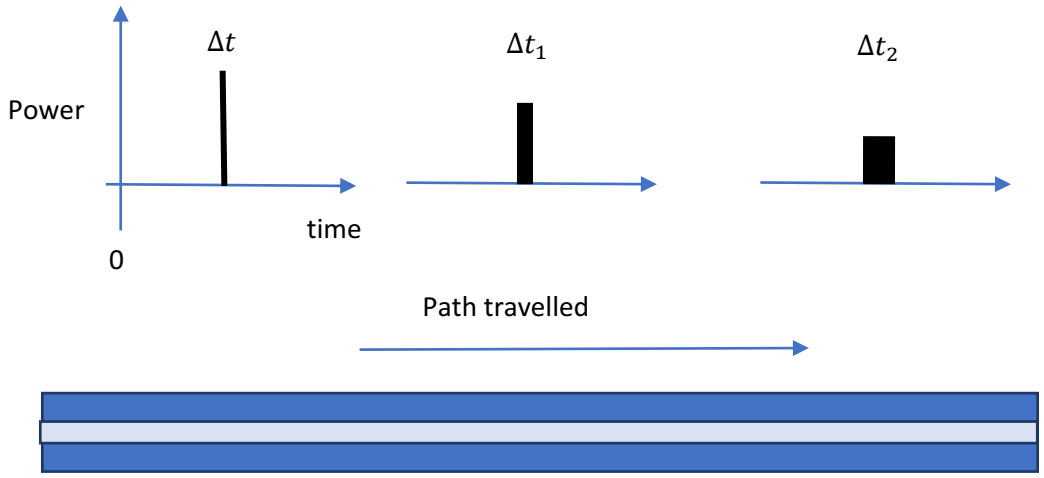

Fig. 21 Spreading of an optical pulse along a longitudinal section of an optical fiber caused by dispersion.

The effect of dispersion can be seen in Fig. 21 Δt represents the time domain broadness of an optical pulse. Δt_1 and Δt_2 represents a wider broadness after the pulse has travelled a certain path.

Let be $X(j\omega)$ the Fourier transform of the input optical signal $x(t)$ and $H(j\omega)$ the Fourier transform of the optical transfer function of the optical fiber.

If the bandwidth of the carrier signal is small we can accurately approximate phase as a linear form with respect the pulsation by (20) if the bandwidth of the input signal is narrow enough [21], [22]:

$$arg\big(H(j\omega)\big) = \psi(\omega) = -\phi - \omega\alpha \tag{20}$$

where arg() represents the argument, $-\phi$ is the initial phase and $-\omega\alpha$ is the pulsation-dependant term.

By convolving the input signal with the optical transfer function of the fiber. We obtain:

$$\begin{aligned} Y(j\omega) = X(j\omega)H(j\omega) &= X(j\omega)\|H(j\omega)\|e^{j\psi(\omega)} \\ &= X(j\omega)\|H(j\omega)\|e^{-j\phi}e^{-j\omega\alpha} = F(x(t-\alpha))\|H(j\omega)\|e^{-j\phi} \end{aligned} \tag{21}$$

where α is the group delay of the media; in this case, the media is an optical fiber. It corresponds to (22):

$$\tau_g = -\frac{d}{d\omega} arg\,(H(j\omega)) = -\frac{d\psi(\omega)}{d\omega} \tag{22}$$

Consequently, as the phase is performed on every time dependence in function $x(t)$ oscillatory part of $x(t)$ is delayed in time τ_{phase}

$$\tau_{phase} = -\frac{arg\ (H(j\omega))}{\omega} \tag{23}$$

If $x(t) = a(t)\cos(\omega t + \theta)$. The output will turn into $y(t) = \|H(j\omega)\|a(t - \tau_g)\cos(\omega(t - \tau_{phase}) + \theta)$ if $a(t)$ variation is slow enough compared to ω.

$\tau_g$or α is therefore an important parameter that shows how much delay is produced over the optical pulse expressed per units of wavelength.

3.3 Fiber Bragg grating sensing

Fiber Bragg Gratings sensors are in-fiber devices fabricated by inscribing a refractive index pattern into the optical fiber core [2], [3]. An ultraviolet light beam sets a periodic pattern into the fiber that is photosensitive to those ultraviolet wavelengths. This is done with the purpose of inscribing different interfaces of refractive index in the core of the photosensitive fiber [23]. Each pattern has its typical refractive index. That periodic pattern affects the wavelengths that can travel forward through the fiber and thus, the wavelengths that are out of that particular set are back-reflected towards the input light source. This is seen in Fig. 22.

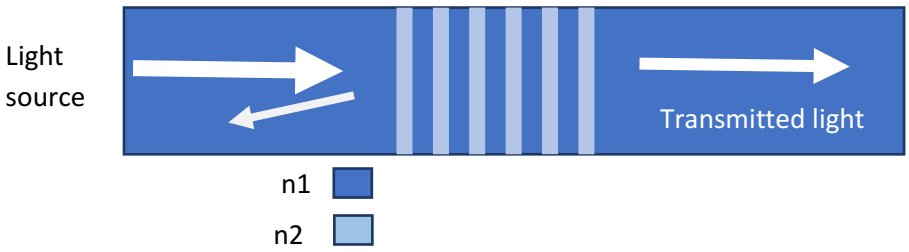

Fig. 22 Diagram of the different interfaces of an FBG sensor.

The FBG is in fact also a sensor as, if we apply strain or temperature, it will affect the intra-grating properties and therefore this change will be translated to changes in the optical back-reflection properties. Therefore, the optical bandwidth that is going to be reflected backward depends on the properties of the grating and the environmental parameters to which the sensor is exposed.

The first order Bragg condition states that the central wavelength at which the grating is reflecting is determined by the grating spacing as [2], [24]:

$$\lambda_B = 2n\Lambda \tag{24}$$

where n is the effective refractive index and Λ is the grating spacing. The Bragg wavelength λ_B, is the central wavelength of the back-reflected optical bandwidth.

The FBG Bragg wavelength depends on the index of refraction and the intra-grating distance or grating spacing.

If we calculate the total differential of (24) with respect to the temperature and the axial strain, we arrive to (25):

$$\begin{aligned}\delta\lambda_B &= 2\left(\left(\frac{dn\Lambda}{dl}\right)dl + \frac{dn\Lambda}{dT}dT\right) \\ &= 2\left(n\frac{d\Lambda}{dl}\Delta l + \Lambda\frac{dn}{dl}\Delta l + \Lambda\frac{dn}{dT}\Delta T + n\frac{d\Lambda}{dT}\Delta T\right)\end{aligned} \tag{25}$$

where dl is a differential of length and dT is a differential of temperature. We can observe two contributions.

The first term represents variations of the Bragg wavelength with respect to the strain applied to the sensor as (26).

$$\delta\lambda_{B,\varepsilon} = \lambda_B\left(\frac{1}{\Lambda}\frac{d\Lambda}{dl}\Delta l + \frac{1}{n}\frac{dn}{dl}\Delta l\right) = \alpha\lambda_B\,\varepsilon \tag{26}$$

where α is the relative strain sensitivity of the fiber Bragg grating sensor.

Similarly, for temperature, we obtain (27):

$$\delta\lambda_{B,T} = \lambda_B\left(\frac{1}{n}\frac{dn}{dT}\Delta T + \frac{1}{\Lambda}\frac{d\Lambda}{dT}\Delta T\right) = (\beta_T + \beta_e)\lambda_B\,\Delta T \tag{27}$$

where β_T is the termo-optic coefficient and β_e is the temperature expansion coefficient. In conclusion, FBG can be used either as strain sensors or as temperature sensors [23], [25]–[28].

Different kinds of FBGs have different properties according to their refractive index distribution. Their back-reflection response depends on the intra-grating space distance distribution as well as the index of refraction of the material.

3.4 Uniform FBG

If we consider a typical fiber Bragg grating formed with several layers at different refraction indexes we can express the index of refraction in terms of a mean value $\overline{n_0}$ and a variation of that

parameter with respect to the optical axis (z-axis) of Δn_0 one can define the index of refraction in terms of the space as (28):

$$n(x) = \overline{n_0} + \Delta n_0 cos\,(\frac{2\pi}{\Lambda} z) \tag{28}$$

Δn_0 is in the range from 0.00001 to 0.01. All those variables are represented in Fig. 23.

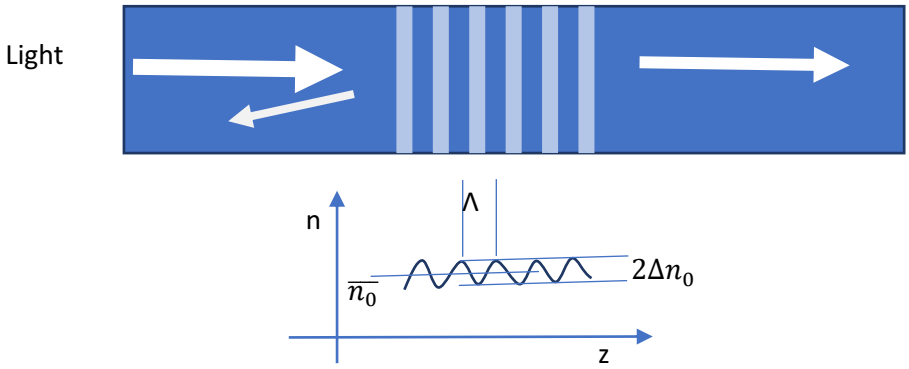

Fig. 23 Morphology of a uniform fiber Bragg grating.

The reading process of the FBGs can be done either with a broadband source and an optical spectrum analyzer, to have the relationship of power with respect to the wavelength, or with a tunable laser and a photodetector, as the wavelength is translated to the time axis. In Fig. 24 we can observe the typical response of an FBG device interrogated by a broadband source or by a tunable laser.

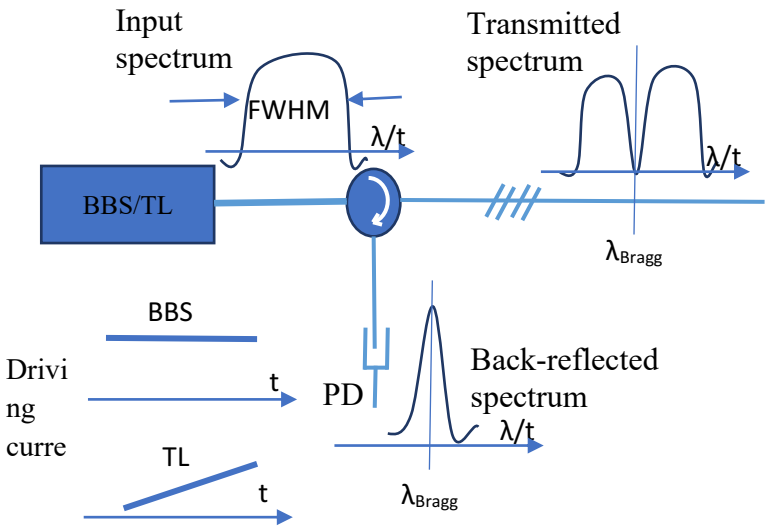

Fig. 24 Back- reflection response of an FBG sensor interrogated with a broadband optical source or a tunable laser. BBS: Broad Band Source, TL: Tunable laser, PD: photo-detector.

The typical interrogating system for an FBG is seen in Fig. 24. The light is back-reflected and the beam is separated from the incident light using a circulator. Finally, the light is analyzed with a PC knowing that the relationship between the time-mapped-power of the sweep and the optical wavelength is linear.

The typical FBG reflection response of Fig. 25 a) is based on VCSEL. In the same picture appears the Bragg wavelength that is placed at λ_B≈1541.21nm. The green trace represents the first derivative of the curve, and it can be used to spot the maximum slope points of the curve at 1541.1nm and 1542.3nm approximately. This trace can be used for different kinds of FBG measuring techniques [29], [30].

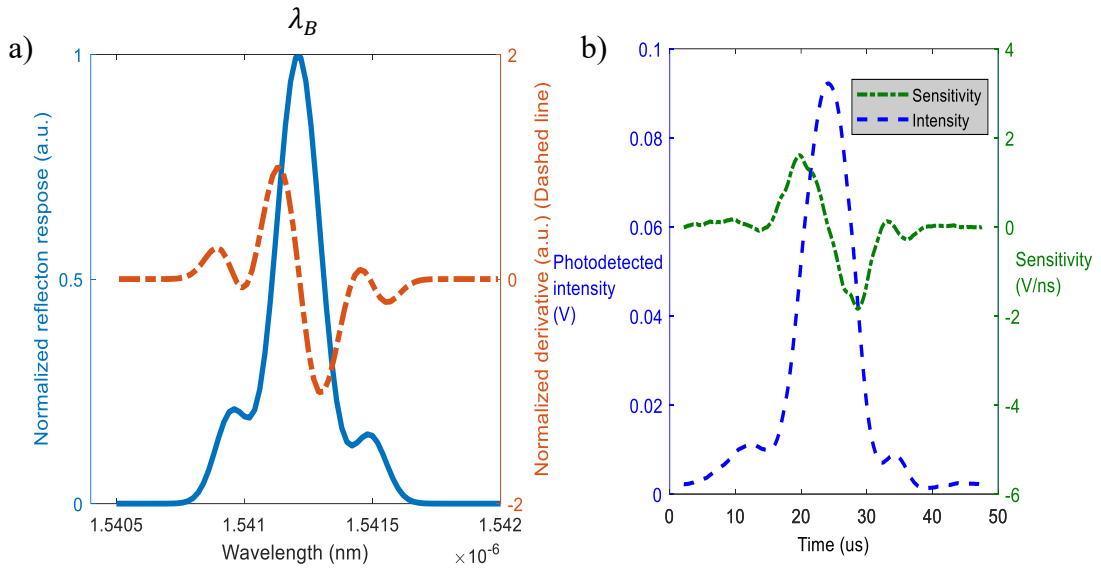

Fig. 25 Reflection response for a Fiber Bragg Grating illuminated by a tunable laser a) mathematical model data for optical domain b) experimental data recorded using a tunable laser.

To complete the analysis, a model is presented and depicted in Fig. 25 b). It responds to the equation (29). This model is presented for one lobe in [31] however here we show how we can extend it to the number of lobes (N) of the FBG:

$$Ro(\lambda) = \sum_{i=1}^{N} R_i \cdot e^{-4 \cdot ln(2) \cdot \left(\frac{\lambda - \lambda_{Bi}}{\Delta\lambda_{Bi}}\right)^2} \tag{29}$$

R_i is the maximum reflectivity of the i-th lobe, λ_{Bi} is the central wavelength of the i-th lobe and $\Delta\lambda_{Bi}$ is the full-width half maximum of the i-th lobe. Finally, N is the number of lobes considered in the model. The equation is stated assuming that the FBG has a finite number of lobes that behave each as a Gaussian curve.

The 3-lobe approximation reduces the error introduced into the model by 20% compared with the one-lobe approximation.

$For\ N = 3$	$i = 1$	$i = 2$	$i = 3$
R_i	0.2 W/W	1 W/W	0.15 W/W
λ_{Bi}	1540.95 nm	1541.12 nm	1541.49 nm
$\Delta\lambda_{Bi}$	0.15 nm	0.2 nm	0.15 nm

Table 1 Parameter table for the FBG model

Table 1 shows the parameters used to simulate the behavior of the FBG absorption shown in Fig. 25 a).

Another approach of reading FBG sensors consists of using an optical line placed in the slope of the reflection profile of the FBG. This produces for every displacement of the FBG an amplitude modulation of the optical line. In Fig. 26 we can observe how a variation of the optical

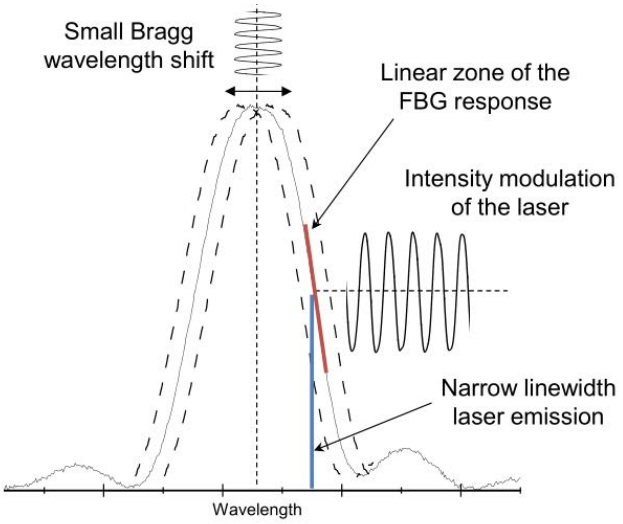

Fig. 26 Diagram of a single line reading process of an FBG sensor.

wavelength of the optical fiber is translated to intensity modulation.

3.5 Chirped FBG

Contrary to uniform FBG sensors, we consider the chirp FBG [32]–[34]. Those devices have a variable intra-grating space Λ with respect to the longitudinal axis (z-axis). This means that the variation of the refractive index is performed with an acceleration in the space frequency. Therefore, the space period of $n(x)$ varies with space as (30):

$$n(x) = \overline{n_0} + \Delta n_0 \cos\left(\frac{2\pi}{\Lambda_0}(\alpha z)z\right) \tag{30}$$

where α is a variation constant of the grating with respect to the z-axis (term αz). Therefore, the intra-grating spacing is not a unique and constant magnitude in those devices. In Fig. 27 the morphology of the device is shown with all the related parameters.

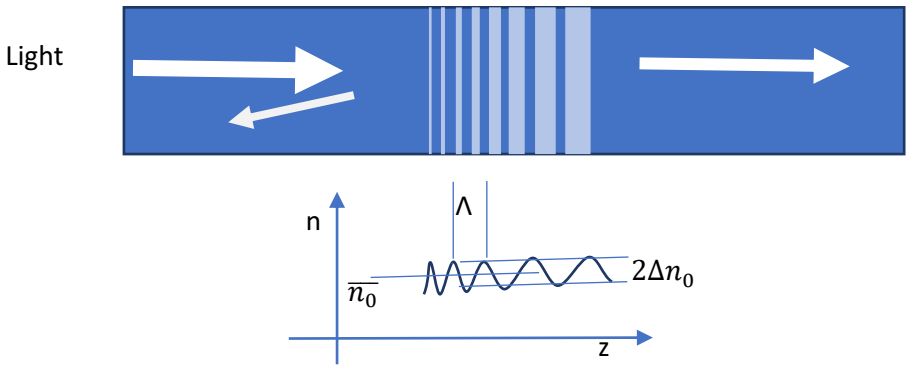

Fig. 27 Morphology of a chirped FBG.

In the case of a chirped FBG, we can see that the phase variation of wavelength has an acceleration with respect to the wavelength. Therefore, the dispersion is not a straight line as in the case of the uniform FBG and therefore it is a parabolic function that has its minimum at a certain wavelength where the phase reference is imposed. In Fig. 28 the reference is imposed at 80% of the chirped FBG and therefore the phase begins to fluctuate at an increasing rate.

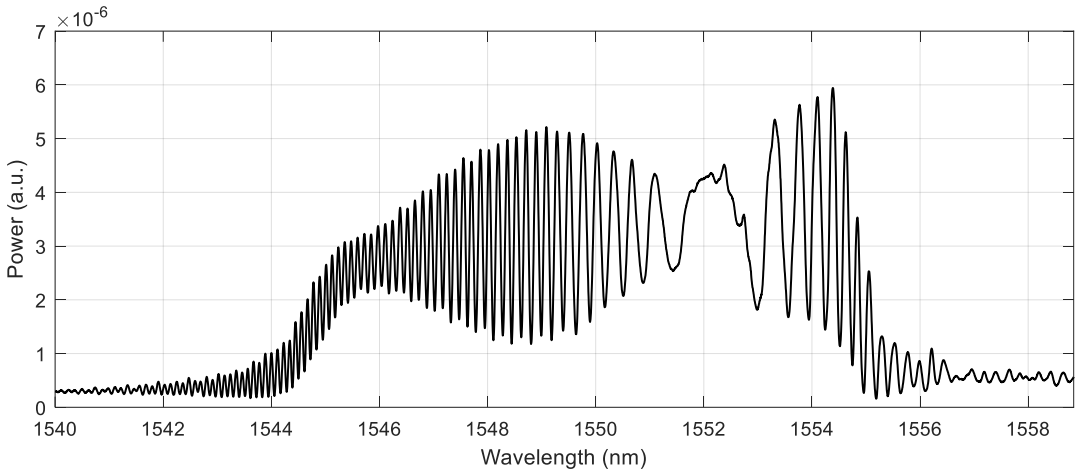

Fig. 28 Dispersion response of a chirped FBG sensor (direct spectra).

If we accumulate the phase of the spectral response, we obtain the quadratic relationship of Fig. 29 which relates the wavelength with the associated dispersion.

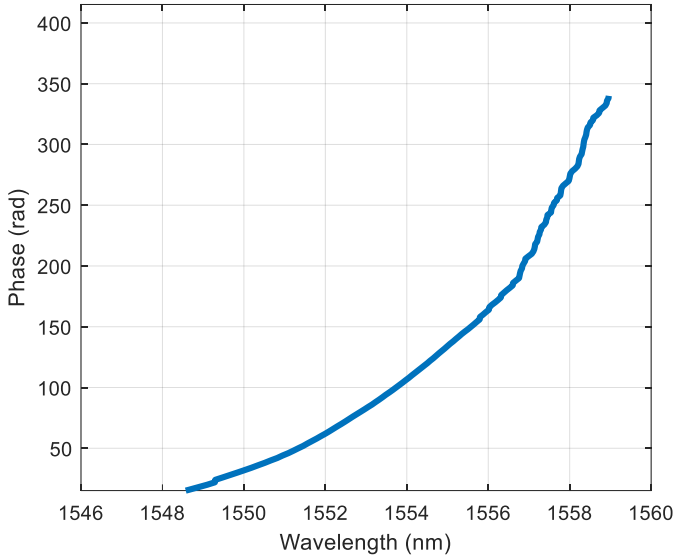

Fig. 29 Dispersion response of phase versus wavelength.

FBGs have been used also for dispersion compensation in optical link systems. This means that the phase that each wavelength is delayed and therefore the broadening process of the pulses can be compensated. In Fig. 30 a) we can observe the dispersion response of a uniform FBG sensor. The number of radians the phase is shifted with respect to a reference wavelength is an indicator of dispersion. In Fig. 30 b) the phase dispersion is represented in terms of the wavelength.

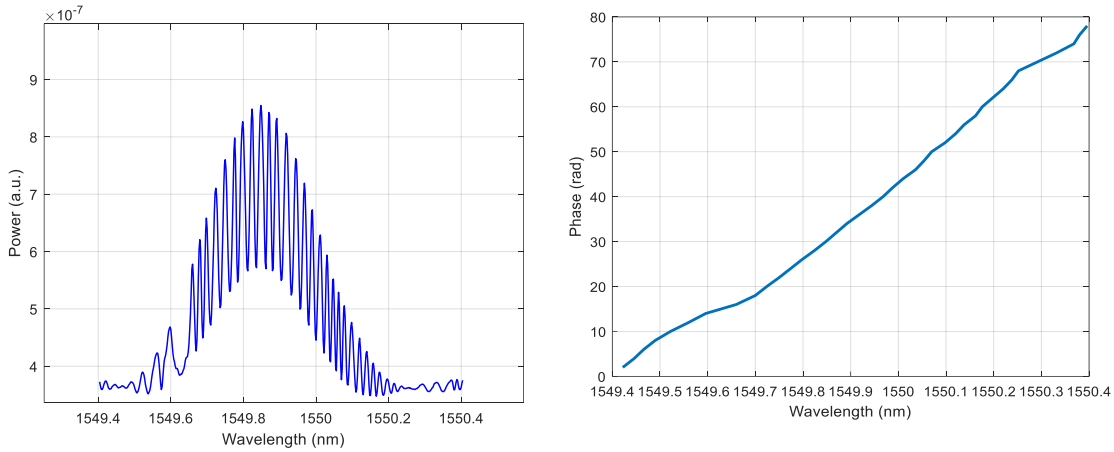

a) b)

Fig. 30 Dispersion response of the FBG sensor. a) direct dispersion readout, b) dispersion response with the wavelength.

3.6 Random fiber grating sensors

A particular case of grating sensors is the random fiber grating sensor. This kind of sensor has a diffractive pattern whose index of refraction is random with respect to the length therefore no deterministic value can be extracted before fabrication as seen in Fig. 31 [35], [36]. This fact leads to a random reflection response with respect to wavelength.

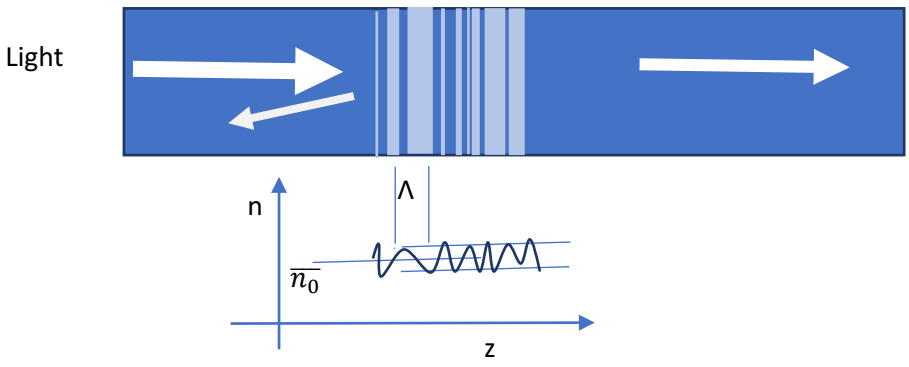

Fig. 31 Morphology of random fiber grating sensors.

Compared to the uniform FBG sensors, random fiber gratings have a spectrum that is degenerated compared to the Gaussian shape one, obtained in the case of uniform FBGs. However, the dependence between the position of the optical transfer function on the spectra axis with the strain applied to the FBG remains true. This can be demonstrated as the correlation peak shifts with respect to the wavelength if the strain is applied to the sensor.

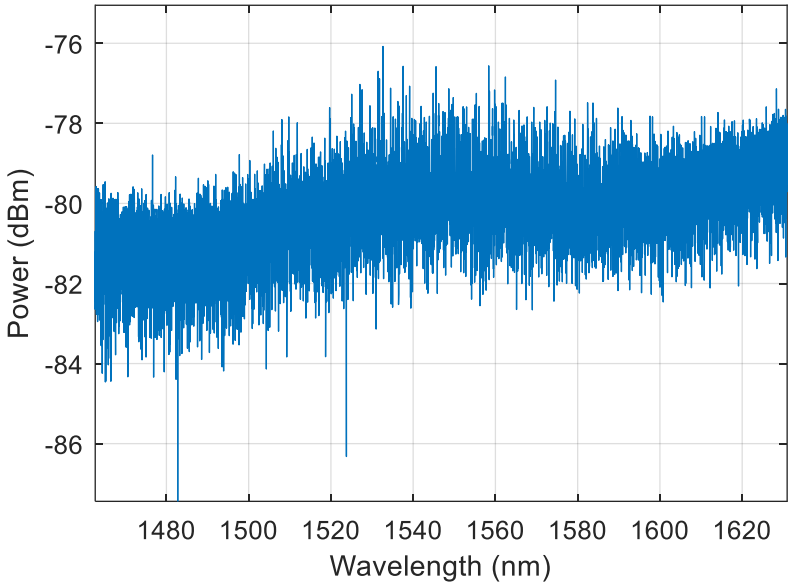

Fig. 32 Reflection profile of a random fiber grating sensor.

Another characteristic is that the back-reflection can be about -30 dB compared to the input to the sensor. This makes it very challenging to obtain a high sensitivity in the sensor.

Another difference between this sensor and the uniform FBG is the wavelength broadness of the random function. In the case of the uniform FBG, it is of the order of 0.2 nm while in the random fiber gratings can reach 200nm-300nm width. This can constitute an advantage compared with the FBG sensors as it allows an easier aligning process between the optical response of the sensor and the reading laser wavelength. This can be useful if several sensors are used. In Fig. 32 it can be observed the reflection profile of a random fiber grating sensor.

3.7 Concept of penetration depth

When irregular strain or temperature is applied to an FBG sensor the distance between each pair of interphases change accordingly to (31) which is a manipulation of (24)

$$\lambda_B(z) = 2n(z)\Lambda(z) \tag{31}$$

As neither the index of refraction $n(z)$, nor the intra-grating spacing $\Lambda(z)$ is constant in each $\lambda_B(z)$ is back-reflected at a different value of depth z therefore the characteristics of each wavelength are associated with a particular length and therefore it is linked to a distributed measurement. That effect is directly related to the chirped FBG; however, it can be induced in a uniform FBG if a gradient perturbation is applied to the sensor. It is because each dl and dT applied to each $dn(z)$ and $d\Lambda(z)$ are not constant as they depend on variables that are position-dependent as can be seen in Fig. 33.

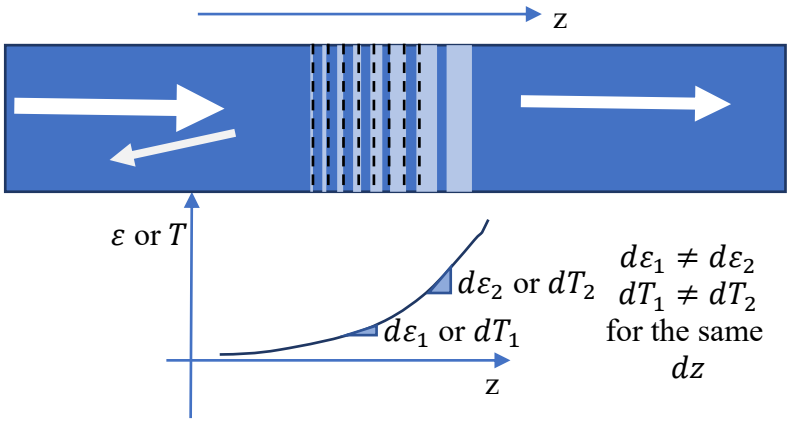

Fig. 33 Gradient magnitude applied to an FBG sensor (In dashed line can be seen the initial position of the grating).

A very important relationship arises, which is the relation of the depth penetration with the wavelength of the FBG. This concept relays on either the dispersion of the FBG or its reflectivity to determine $z(\lambda)$ and therefore the position with respect to one side of the diffractive structure.

The reflection-based calculation is the easiest approach as z coordinates can be obtained from the back reflection response $R(\lambda)$ of the FBG [3] as shown in (32).

$$z(\lambda) = -\frac{L}{2} + \frac{2n}{(\pi \Delta n)^2} \int_{\lambda(z=-L/2)}^{\lambda} -ln\big(1 - R(\lambda')\big)\, d\lambda' \tag{32}$$

where L Is the length of the grating, n is the refracting index, Δn is the variation of the refractive index and $R(\lambda)$ is the response of reflectivity with wavelength.

For the phase-based calculation one can relate the wavelength with the penetration depth. This way we use the dispersion profile of the non-uniform FBG as (33).

The important aspect is that the relationship (33) is dispersion dependent ($\frac{d\phi}{d\lambda}$ term) [3] therefore if the dispersion (group delay) does not vary ($\frac{d\phi}{d\lambda}$ is constant) no penetration depth can be associated to wavelength. Therefore, on a uniform FBG whose strain application field is constant, no penetration depth can be found. Therefore, the density of passing fringes has to vary with the wavelength to be able to associate each $z(\lambda)$ to a particular wavelength.

$$z(\lambda) = -\left(\frac{\lambda^2}{4\pi n}\right)\frac{d\phi}{d\lambda} \tag{33}$$

where λ is the wavelength, n is the refractive index and ϕ is the accumulative wavelength in the wavelength interferogram.

3.8 Conclusions

In this chapter, the main physical parameters of fiber Bragg grating sensors were presented. The optical fiber and the optical fiber sensors are devices that allow the confinement of the light and at the same time provide a durable solution for harsh environments as in chemical or radioactive media.

Fiber Bragg grating sensors are devices that behave as optical filters in wavelength domain. Their center wavelength (Bragg wavelength) changes accordingly if strain or temperature is applied to them. Uniform fiber Bragg gratings, chirp fiber Bragg gratings and random fiber grating sensors have been presented in this chapter.

Chapter 4: Models and simulation of multiheterodyne sources

“Sooner or later discipline will defeat intelligence"- Japanese proverb.

4.1 Introduction

This chapter describes, in a simplified way, the process of electro-optical dual-comb modulation. We present the general approach for a classic architecture of two-phase modulation stages with a frequency shift, as well as a full phase modulation-based architecture. Finally, the acousto-optic self-heterodyne approach is also included.

We comment on phase generated carrier for one-to-one mapping of the optical domain dual-comb to the electrical domain comb. We also present the acousto-optic combs, which are a novelty in the state of the art, and their mapping by means of a self-heterodyne technique. We briefly present the all-optical dual optical frequency comb that for the first time, is implemented in this Thesis.

4.2 The electro-optic dual optical frequency comb

4.2.1 Two modulation stages and frequency shift

The Jacobi-Anger identity relates the phase modulation with its Fourier transform [37] and demonstrates that the phase modulation generates multiple modes or tones that are spaced uniformly in argument as (34).

$$e^{j\,\beta\,sin(\phi)} = \sum_{n=-\infty}^{\infty} J_n(\beta) e^{j\,n\,\phi} \tag{34}$$

where β is the depth modulation of the phase modulation and ϕ denotes the amount of phase that the phase modulator is introducing to the optical wave. $J_n(\beta)$ denotes the Bessel function of the first kind of order n and argument β.

On the other hand, we have a solution of the wave equation that denotes the light wave as (35)

$$E(x,t) = \|A\| e^{j\,\phi(x)} e^{j2\,\pi\nu\,t} \tag{35}$$

were $\|A\|$ is the amplitude of the electric field, $\phi(x)$ is the phase at each point of the space along which the wave is traveling, and ν is the optical frequency at which the wave fluctuates with respect to time.

For simplicity, we can make a variable change according to (36):

$$E(x,t) = A(x)e^{j2\,\pi\nu\,t} \tag{36}$$

If we are heterodyning the signal utilizing an acousto-optic modulator, we achieve a signal with a frequency increase of $\delta\nu$ leading to (37):

$$E_{AOM}(x,t) = A(x)e^{j2\,\pi(\nu+\delta\nu)\,t} \tag{37}$$

On the other hand, if we use an electro-optic modulator (optical phase modulator) [8], we obtain (38):

$$E_{EOM}(x,t) = A(x)e^{j2\,\pi\nu\,t}e^{j\,z\,sin(\phi)} \tag{38}$$

In which the last multiplying term represents the phase modulation induced by the phase modulator. z is the rate between the amplitude of the sinusoidal function injected into the modulator and the pi-voltage (V_π) of the device as defined in chapter 2.

If we assume that an interferometric mixing of the coherent combs [38] [39] is happening on the output coupler of a dual optical frequency comb generator we can obtain the general equation of the interference of two light beams at the output of the optical coupler (as it is shown in Fig. 34).

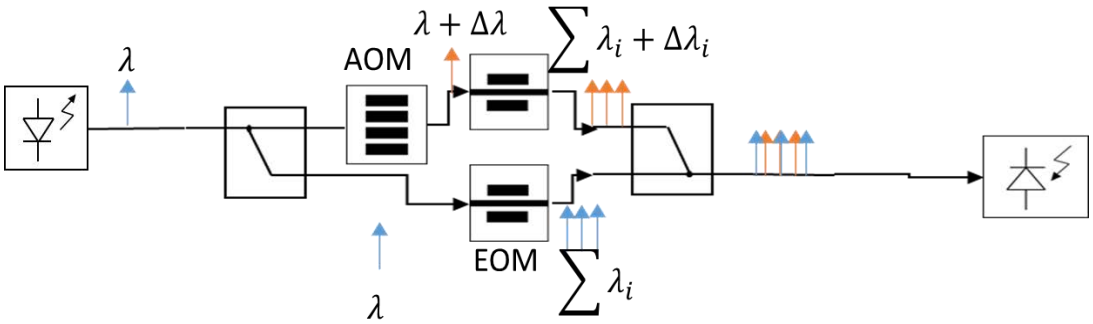

Fig. 34 Setup of a dual optical frequency comb.

Let the electric field on the first arm be E_1 and the electric field of the second arm be E_2. We can obtain the irradiance I at the output photo detecting stage as (39):

$$
\begin{aligned}
I_{DOFCG} &= (E_1 + E_2)^*(E_1 + E_2) \\
&= \left(\|A_1\| e^{j(-\phi_1(x,t))} e^{-j2\,\pi\nu_1\,t}\right. \\
&\quad \left. + \|A_2\| e^{j(-\phi_2(x,t))} e^{-j2\,\pi\nu_2\,t}\right)\left(\|A_1\| e^{j\phi_1(x,t)} e^{j2\,\pi\nu_1\,t}\right. \\
&\quad \left. + \|A_2\| e^{j\phi_2(x,t)} e^{j2\,\pi\nu_2\,t}\right) \\
&= \|A_1\|^2 + \|A_2\|^2 \\
&\quad + 2\|A_1\|\|A_2\| \left(\frac{e^{-j\phi_1(x,t)} e^{-j2\,\pi\nu_1\,t} e^{j\phi_2(x,t)} e^{-j2\,\pi\nu_2\,t}}{2}\right. \\
&\quad \left. + \frac{e^{-j(\phi_2(x,t)-\phi_1(x,t)+2\,\pi t(\nu_2-\nu_1\,))}}{2}\right) \\
&= \|A_1\|^2 + \|A_2\|^2 + 2\|A_1\|\|A_2\| cos\,(\phi_2(x,t) - \phi_1(x,t) \\
&\quad + 2\,\pi t(\nu_2 - \nu_1\,))
\end{aligned}
\tag{39}
$$

As stated before, we are modulating both arms in phase besides we have a frequency shift denoted by $(\nu_2 - \nu_1\,) = \Delta\nu$. The amount of phase the light is varying along the first arm [9] of the dual-comb can be expressed as (40).

$$\phi_1(x,t) = \beta_1\, sin(\omega_1 t) + \phi_1(x) \tag{40}$$

Besides, on the second arm, the amount of phase that the light is varying is (41)

$$\phi_2(x,t) = \beta_2\, sin(\omega_2 t) + \phi_2(x) \tag{41}$$

Thus, if we substitute the phase modulation into (39) we obtain (42):

$$
\begin{aligned}
&I_{DOFCG} \\
&= \|A_1\|^2 + \|A_2\|^2 \\
&+ 2\|A_1\|\|A_2\|\, cos(\,\beta_2\, sin(\omega_2 t) - \beta_1\, sin(\omega_1 t) + 2\,\pi t(\nu_2 - \nu_1\,) + \phi_2(x) \\
&- \phi_1(x)) \\
&= \|A_1\|^2 + \|A_2\|^2 \\
&+ 2\|A_1\|\|A_2\| Re(e^{j(\,\beta_2\, sin(\omega_2 t) - \beta_1\, sin(\omega_1 t) + 2\,\pi t(\nu_2 - \nu_1\,) + \phi_2(x) - \phi_1(x))} \\
&= \|A_1\|^2 + \|A_2\|^2 + 2\|A_1\|\|A_2\| Re(\sigma)
\end{aligned}
\tag{42}
$$

We can see how the irradiance of the dual-comb is dependent on the parameters of the modulations those are the depth modulations of the first and second arms (β_1 and β_2) and the

frequency of the electro-optic modulation signals (ω_2 and ω_1). We take into consideration the phase term of the dual-comb electrical mapping process as (43):

$$\sigma = e^{j(\,\beta_2\, sin(\omega_2 t))} e^{j(\,-\beta_1\, sin(\omega_1 t))} e^{j(\,2\,\pi t(\nu_2 - \nu_1\,))} e^{j(\phi_2(x) - \phi_1(x))} \tag{43}$$

We apply the Jacobi-Anger expansion to rewrite the above equation and we consider the trigonometric identity (44):

$$e^{-j\,\beta\, sin(\phi)} = e^{j\,\beta(\,-sin(\phi))} = e^{j\,\beta(\,sin(-\phi))} \tag{44}$$

We obtain (45):

$$\begin{aligned} \sigma = e^{j(\,2\,\pi t(\nu_2 - \nu_1\,))} \cdot \sum_{n=-\infty}^{\infty} J_n(\beta_2) e^{j\,n\,\omega_2 t} \\ \cdot \sum_{h=-\infty}^{\infty} J_h(\beta_1) e^{j\,h\,(-\omega_1 t)} \cdot e^{j(\phi_2(x) - \phi_1(x))} \end{aligned} \tag{45}$$

Afterward, we define γ as (46):

$$\gamma = \sum_{n=-\infty}^{\infty} J_n(\beta_2) e^{j\,n\,\omega_2 t} \cdot \sum_{h=-\infty}^{\infty} J_h(\beta_1) e^{j\,h\,(-\omega_1 t)} \tag{46}$$

We rearrange sums and separate the results between equal indexes ($n = h$) and different indexes ($n \neq h$) we obtain that for all ($n \neq h$) The frequency lies outside of the photo-detecting diode bandwidth and therefore those terms can be neglected (γ_{HF}) as (47):

$$\begin{aligned} \gamma &= \sum_{n=-\infty}^{\infty} \sum_{h=-\infty}^{\infty} J_n(\beta_2) J_h(\beta_1) e^{j\,((n\,\omega_2 - h\,\omega_1)t)} \\ &= \sum_{k=-\infty\ \forall\ n=h}^{\infty} J_k(\beta_2) J_k(\beta_1) e^{j\,((\,\omega_2 - \,\omega_1)kt)} \\ &+ \sum_{n=-\infty}^{\infty} \sum_{h=-\infty\ \forall\ n\neq h}^{\infty} J_n(\beta_2) J_h(\beta_1) e^{j\,((n\,\omega_2 - h\,\omega_1)t)} \\ &= \gamma_{PDBW} + \gamma_{HF} \approx \gamma_{PDBW} \end{aligned} \tag{47}$$

where n, k and h are integers. The simplification leads to the following identity (48):

$$\sigma \approx \sum_{k=-\infty}^{\infty} \sum_{\forall n=h} J_k(\beta_2) J_k(\beta_1) e^{j\,(\,2\,\pi t(\nu_2-\nu_1+(\,\omega_2-\,\omega_1)k\,))} \cdot e^{j(\phi_2(x)-\phi_1(x))} \tag{48}$$

That can be substituted into (39) to obtain the waveform of the photo-detected current as (49).

$$\begin{aligned} & I_{DOFCG} \\ & = \|A_1\|^2 + \|A_2\|^2 \\ & + 2\|A_1\|\|A_2\| Re\left(\sum_{k=-\infty}^{\infty} J_k(\beta_2) J_k(\beta_1) e^{j\,(\,2\,\pi t(\nu_2-\nu_1)+t(\,\omega_2-\,\omega_1)k\,)} \right. \\ & \left. \cdot e^{j(\phi_2(x)-\phi_1(x))} \right) \\ & = \|A_1\|^2 + \|A_2\|^2 \\ & + 2\|A_1\|\|A_2\| \left(\sum_{k=-\infty}^{\infty} J_k(\beta_2) J_k(\beta_1) cos\,(\,2\,\pi t(\nu_2-\nu_1) \right. \\ & \left. + t(\,\omega_2-\,\omega_1)k\,)+\phi_2(x)-\phi_1(x)) \right) \end{aligned} \tag{49}$$

If a spectrum analysis is used and the DC terms are eliminated, the following term is obtained as (50):

$$\begin{aligned} I_{DOFCG,ESA} = 2\|A_1\|\|A_2\| & \left(\sum_{k=-\infty}^{\infty} J_k(\beta_2) J_k(\beta_1) cos\,(\,2\,\pi t(\nu_2-\nu_1) \right. \\ & \left. + t(\,\omega_2-\,\omega_1)k\,)+\phi_2(x)-\phi_1(x)) \right) \end{aligned} \tag{50}$$

where $2\|A_1\|\|A_2\|J_k(\beta_2)J_k(\beta_1)$ represents the optical amplitude of the adjacent modes. Accordingly, the frequency difference $(\nu_2-\nu_1)$ is the frequency of the electrical carrier and $(\,\omega_2-\,\omega_1)k$ corresponds to the sidebands that are generated at integer multiples of $(\omega_2-\,\omega_1)$ which is the difference between the electrical frequencies at which the modulators are driven. Finally, $\phi_2(x)-\phi_1(x)$ is the term related to the optical phase difference of the interferometer that constitutes the dual-comb architecture.

As a summary, we can extract from the above equations that the electronic mapping is a one-to-one process between each pair of optical modes in the wavelength domain. These equations do not contain any nonlinearity effect nor dispersion effects that happen in the fiber.

4.2.2 Three modulation stages with sinusoidal signals

If three-phase modulators are used, the Jacobi-Anger identity should be applied three times once for each phase modulation (51). It is assumed that the two first modulations happen in one arm and the third happens on the second arm of the interferometer.

$$\begin{aligned} I_{DOFCG} &= \|A_1\|^2 + \|A_2\|^2 \\ &+ 2\|A_1\|\|A_2\| \cos((\beta_3 \sin(\omega_3 t) + \beta_2 \sin(\omega_2 t)) - \beta_1 \sin(\omega_1 t) \\ &+ \phi_2(x) - \phi_1(x)) = \|A_1\|^2 + \|A_2\|^2 + 2\|A_1\|\|A_2\| Re(\sigma) \end{aligned} \quad (51)$$

Similar to what it has been done in (42), we can find the relationship (52):

$$\begin{aligned} \sigma = \sum_{m=-\infty}^{\infty} J_m(\beta_3) e^{j\, m\, (\omega_3 t)} \cdot \sum_{n=-\infty}^{\infty} J_n(\beta_2) e^{j\, n\, \omega_2 t} \\ \cdot \sum_{h=-\infty}^{\infty} J_h(\beta_1) e^{j\, h\, (-\omega_1 t)} \cdot e^{j(\phi_2(x) - \phi_1(x))} \end{aligned} \quad (52)$$

For simplicity, we operate just with the term (53):

$$\begin{aligned} \gamma &= \sum_{m=-\infty}^{\infty} J_m(\beta_3) e^{j\, m\, (\omega_3 t)} \cdot \sum_{n=-\infty}^{\infty} J_n(\beta_2) e^{j\, n\, \omega_2 t} \cdot \sum_{h=-\infty}^{\infty} J_h(\beta_1) e^{j\, h\, (-\omega_1 t)} \\ &= \sum_{m=-\infty}^{\infty} J_m(\beta_3) e^{j\, m\, (\omega_3 t)} \\ &\cdot \left(\sum_{k=-\infty\, \forall\, n=h}^{\infty} J_k(\beta_2) J_k(\beta_1) e^{j\, ((\omega_2 - \omega_1) k t)} \right. \\ &\left. + \sum_{n=-\infty}^{\infty} \sum_{h=-\infty\, \forall\, n \neq h}^{\infty} J_n(\beta_2) J_h(\beta_1) e^{j\, ((n\, \omega_2 - h\, \omega_1) t)} \right) \\ &= \gamma_{PDBW} + \gamma_{HF} \approx \gamma_{PDBW} \end{aligned} \quad (53)$$

For convenience, we eliminate the harmonics that lie outside the photodetector bandwidth γ_{HF}.

That leads to (54):

$$\begin{aligned}
&\sigma \\
&\approx \sum_{m=-\infty}^{\infty} J_m(\beta_3) e^{j\, m\, (\omega_3 t)} \\
&\cdot \left(\sum_{k=-\infty \,\forall\, n=h}^{\infty} J_k(\beta_2) J_k(\beta_1) e^{j\,((\,\omega_2 - \,\omega_1) k t)} \right) e^{j(\phi_2(x) - \phi_1(x))} \\
&= \sum_{m=-\infty}^{\infty} \left(\sum_{k=-\infty \,\forall\, n=h}^{\infty} J_m(\beta_3) J_k(\beta_2) J_k(\beta_1) e^{j\,((\,\omega_2 - \,\omega_1) k t + m\, (\omega_3 t))} \right) \\
&\cdot e^{j(\phi_2(x) - \phi_1(x))}
\end{aligned} \tag{54}$$

Finally, the result of the signal photo-detected in a spectrum analysis is the AC term of the waveform. As shown in (55):

$$\begin{aligned}
I_{DOFCG,ESA,T} = 2\|A_1\|\|A_2\| \sum_{m=-\infty}^{\infty} \left(\sum_{k=-\infty}^{\infty} J_m(\beta_3) J_k(\beta_2) J_k(\beta_1) cos\,((\,\omega_2 \right. \\
\left. - \,\omega_1) k t + m\, (\omega_3 t) + \phi_2(x) - \phi_1(x)) \right)
\end{aligned} \tag{55}$$

4.2.3 Transfer function approach

We can see the dual-comb modulation as an operation over an electrical field phasor. Therefore, we can consider the generating systems as a nonlinear system black box as shown in Fig. 35.

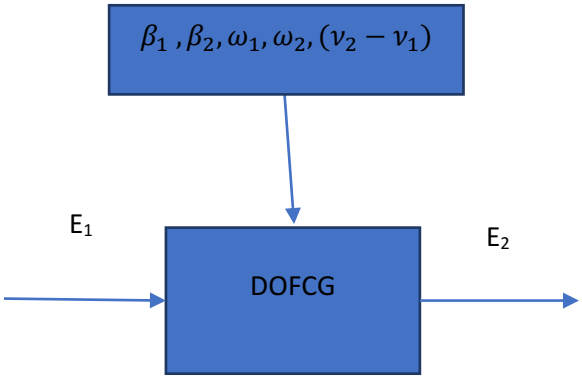

Fig. 35 One stage modulation of the dual-comb scheme as the transfer function.

If we assume a phasor to be the input, the electric field is (56):

$$E_1(x,t) = \|A\| e^{j\,\phi(x,t)} e^{j(2\,\pi\nu_1\,t - kx)} \tag{56}$$

The output electric field at the block is of the form of (57):

$$\begin{aligned} E_2 = {} & \frac{\|A\|}{\sqrt{2}} e^{j\,\phi_1'(x,t)} e^{j(2\,\pi\nu_1 t - kx)} e^{j\,\phi(x,t)} e^{j(\,\beta_1\,sin(\omega_1 t))} \\ & + \frac{\|A\|}{\sqrt{2}} e^{j\,\phi_2'(x,t)} e^{j(2\,\pi\nu_2 t - kx)} e^{j\,\phi(x,t)} e^{j(\,\beta_2\,sin(\omega_2 t))} \\ & = \frac{E_1}{\sqrt{2}}\, e^{j(\,\beta_1\,sin(\omega_1 t))} + \frac{E_1}{\sqrt{2}}\, e^{j(\,\beta_2\,sin(\omega_2 t))} e^{j(2\,\pi(\nu_2 - \nu_1)t)} \end{aligned} \tag{57}$$

$e^{j\,\phi_1'(x,t)}$ and $e^{j\,\phi_2'(x,t)}$ represent the phase injected by the system. Therefore, the transfer function between phasors in the block (output phasor over input phasor) is (58) and it constitutes a generalization of the behavior of the system:

$$\frac{E_2}{E_1} = \frac{e^{j(\,\beta_1\,sin(\omega_1 t))}}{\sqrt{2}} + \frac{e^{j(\,\beta_2\,sin(\omega_2 t))} e^{j(2\,\pi(\nu_2 - \nu_1)t)}}{\sqrt{2}} \tag{58}$$

The expression in (58) indicates the system generates two electric field phasors that have independent phase modulation.

This constitutes a non-linear system as $\frac{E_2}{E_1}$ transfer function affects the frequency of the input laser signal.

4.3 The acousto-optic comb

The acousto-optic comb is generated by simply feeding-back an acousto-optic modulator [40]–[42]. This way the generated spectra are a set of optical tones separated in optical frequency. This separation is equal to the frequency injected into the acousto-optic modulator. We can consider therefore that each tone is added up to the output spectra as the seed beam travels along the feedback loop. This process is conceptually depicted in Fig. 36. It is noteworthy to mention that amplification is needed in the feedback as the attenuation between each loop is high for each iteration of the feedback.

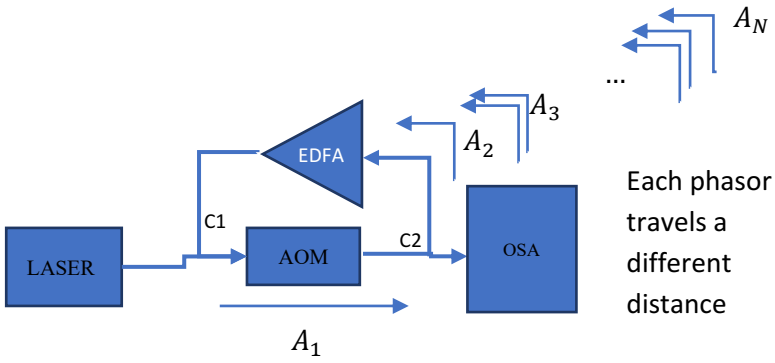

Fig. 36 Acousto-optic comb arrangement. The monochromatic seed beam travels along with the feedback that is composed of the beam splitters C1 and C2.

Therefore, the superposition of each phasor leads to a sum of phasors with different frequencies, path lengths and optical phases according to (59).

$$E_{comb}(t,z) = E_0 \sum_{a=1}^{N} A_a e^{j\left((\omega_0 + a\Delta\omega_{AOM})\, t - \frac{2\pi n}{\lambda + a\Delta\lambda}(z + (a-1)\Delta L) + \phi_a\right)} \tag{59}$$

where ω_0 is the initial pulsation of the light wave, E_0 denotes the electric field in the C1 coupler input, A_a symbolizes an attenuation factor specific to the tone a, which depends on the gain of the optical amplifier (EDFA), on the insertion losses of the couplers C1 and C2 and on the AOM insertion losses. $\Delta\omega_{AOM}$ is the frequency shift produced by the AOM; equivalently, $\Delta\lambda$ is the wavelength shift of the light caused by the AOM. ΔL is the delay of fiber length that the light travels in the feedback loop, n is the refractive index of the fiber, ϕ_a is the initial phase of tone a and z is the space coordinate where the electric field is evaluated at the time t.

This kind of combs has the advantage of being easy use and build; however, they require a highly coherent laser source in order to make it interfere at each iteration of the feedback loop.

Moreover, the span of the acousto-optic combs depends on the amplifier gain and the attenuation of the components that integrate the optical loop.

4.3.1 The self-heterodyne comb

Each optical tone of a self-heterodyne comb is mapped into the RF domain. The process occurs due to the mixing between the initial comb and an optical tone which has a mismatched frequency with respect to the first tone of the comb. The process is shown conceptually in Fig. 37 a), where each phasor is mixed with the reference seed. As a consequence, an RF signal is obtained proportional to the amplitude of each comb teeth and the optical phase difference between the seed and the comb teeth.

Fig. 37 b) shows a way of implementing the aforementioned system with building blocks. The requirement of a comb shift is important as it has to be single-band -generated for ensuring that the RF mapping is done one to one and no cross mixing is produced by any symmetric sideband.

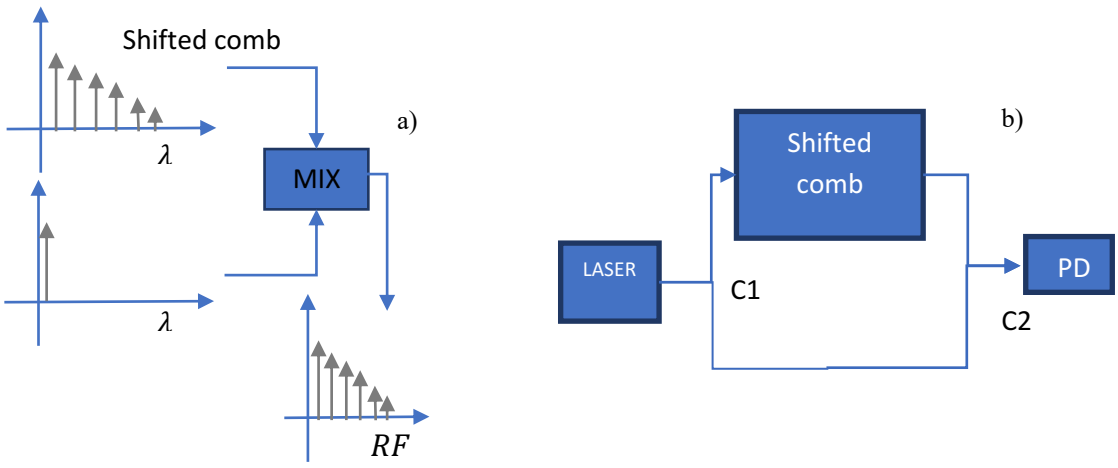

Fig. 37 The mixing process of a self-heterodyne comb, a) diagram interpretation of the comb with the initial seed laser, b) schematic implementation.

4.3.2 The self-heterodyne acousto-optic frequency comb

The self-heterodyne arrangement is easily done with the acousto-optic comb. The mix of the comb with the laser seed leads to a multi-heterodyne mix. The arrangement for producing the self-heterodyne acousto-optic comb is shown in Fig. 38 a). The system delivers an optical comb whose spectra are mapped one to one into an RF comb for example the one shown in Fig. 38 b).

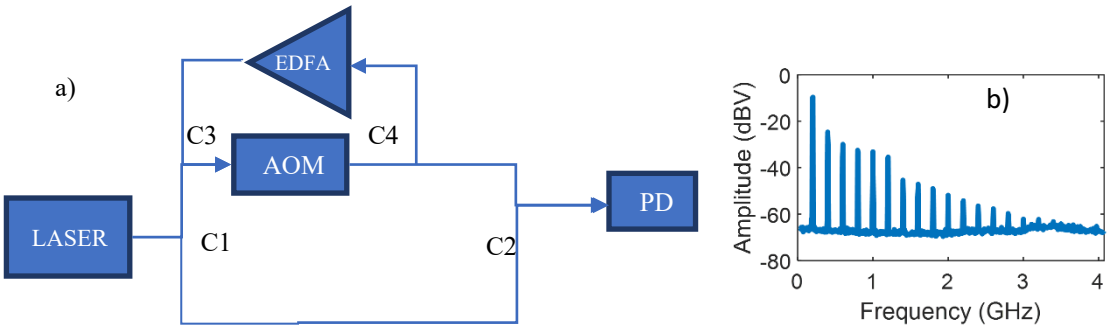

Fig. 38 Self heterodyne acousto-optic frequency comb. a) arrangement set-up based on a feedbacked acousto-optic modulator. b) photo-detected interferogram in the frequency domain.

The photo detected intensity is of the form (60).

$$I(z,t) = \sum_{a=1}^{N} E_0^2 A_a^2 + E_0^2 + 2E_0^2 A_a cos\left(a\Delta\omega_{AOM} t + \frac{2\pi n}{\lambda + a\Delta\lambda}(z + (a-1)\Delta L) - k_1 z_1 + \phi_a - \phi_1\right) \quad (60)$$

where $\Delta\omega_{AOM}$ is the pulsation of the acousto-optic modulator, n is the index of refraction, λ is the wavelength of the laser seed, ΔL is the length of the optical feedback, z is the space coordinate, $E_0^2 A_a^2$ is the power of the a-th mode. (60) shows that the amplitude and phase of the optical tones can be read from the amplitude and phase of the RF image.

4.4 Conclusions

This chapter presents a formulation of the modulation applied to generate dual-combs and self-heterodyne combs. It shows the relationship between the optical domain and the electrical domain. Alternative modulation approaches are also presented and discussed as useful tools for dual-comb generation and multi-heterodyne detection. As a result, a particular overview of the properties of spacing, mapping frequency and the span of the optical frequency combs is obtained, which enables to understand the parameters to optimize when using these kinds of sources in particular applications, such as the interrogation of fiber sensors.

The discussed architectures provide injective mapping and allow direct readout of absorption profiles in the optical domain.

Chapter 5: Electro-optic dual optical frequency comb for fiber Bragg grating readout

“A calm and humble life will bring more happiness than the pursuit of success and the constant restlessness that comes with it."- Albert Einstein

5.1 Introduction

Optical frequency combs (OFC) generated by electro-optic modulation of continuous-wave lasers provide coherent sources that are composed by several optical lines with high power per line. Some of the topologies allow independent control of line spacing as well as the number of lines that are generated. They are suitable for spectroscopy purposes, besides they offer flexible and optimized sources for the interrogation of other sensors based on wavelength change or wavelength filtering, such as fiber Bragg grating (FBG) sensors. In this chapter, a dual-OFC FBG interrogation system based on a single laser, two EOM (phase modulators) and one AOM (frequency shift) is presented. This architecture allows to select and adjust properly the multimode optical source parameters, such as the number of modes and their position within the reflected spectrum of the FBG. A direct read-out is obtained by mapping the optical spectrum onto the radio-frequency spectrum output of the dual-comb. This interrogation scheme is proposed for measuring fast phenomena such as vibrations and ultrasounds.

The main contents of this chapter are published in the journal article: J. E. Posada-Roman, J. A. Garcia-Souto, D. A. Poiana, and P. Acedo, “Fast Interrogation of Fiber Bragg Gratings with Electro-Optical Dual Optical Frequency Combs”, Sensors, vol. 16, no. 12, pp. 2007-2018, 2016. https://doi.org/10.3390/s16122007

5.2 The interrogation method

When we want to read the back-reflection profile of an FBG one can use one single tone as shown in Fig. 39 a). We direct the light beam to port 1 of a circulator and on port 2 we connect the FBG sensor. This way and by careful alignment between the wavelength of the laser and the back-reflection profile, we obtain on port 3 of the circulator the strain information that is applied to the sensor by registering the amplitude of the back-reflected light beam. This alignment should make the laser line coincide with the part of the spectra of interest that is the point in which the derivative of the back-reflected function is maximum. As shown in Fig. 39 b) the understudy set of wavelengths can be approximated to a linear region in a small signal regime. This modulates accordingly the back-reflected line amplitude of the laser.

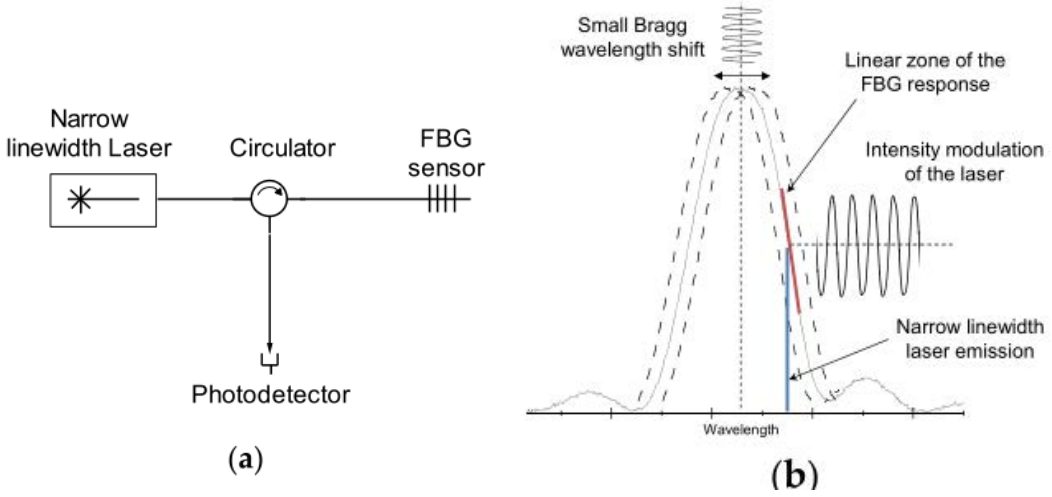

Fig. 39 Single-tone approach for measuring with the reflection response.

The dual combs can be used for the readout of dynamic strain applied to the FBG sensors. The proposed working principle is depicted in Fig. 40 a). In this case, we can operate with two lines of the dual-comb that are placed in the linear region of the FBG reflection profile in order to obtain a linear amplitude modulation of both lines. It is noteworthy to remark that the lines are modulated in counterphase because of the slope that each line is modulated with. In the left line if the Bragg wavelength increases the line diminishes its amplitude due to an increase of attenuation. On the other hand, the right line experiments an increase in amplitude due to the decrease of attenuation when the Bragg wavelength increases due to strain variations. Fig. 40 b) shows the overall implementation where the dual comb generator is injected into the FBG sensor, and the back-reflection is read thanks to a circulator and a photodetector.

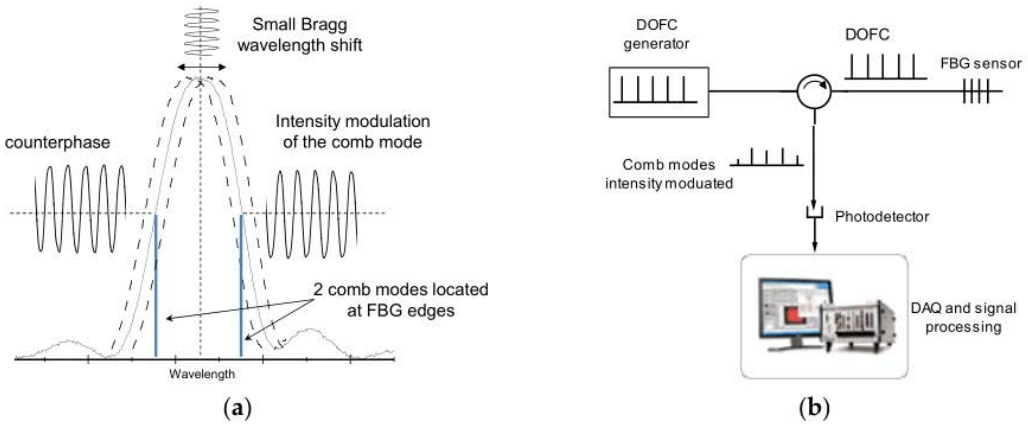

Fig. 40 Working principle of the dual-comb readout applied to a fiber Bragg grating sensor, a) mode placing of the dual-comb, b) general setup schematic.

One can assume that the back-reflection response of a fiber Bragg grating sensor is of the form of (61).

$$I_{out} = \frac{1}{4} R P_0 e^{-4\,ln(2)\left(\frac{\Delta\lambda}{\Delta\lambda_B}\right)^2} \tag{61}$$

where R is the maximum reflectivity of the FBG (a value between 0 and 1), P_0 is the power of the line that is being reflected by the FBG sensor, $\Delta\lambda_B$ is the width of the reflection profile lobe at one-half of the maximum power and $\Delta\lambda$ is defined as the subtraction between the wavelength and the Bragg wavelength of the FBG sensor. To obtain the maximum slope we differentiate the function $I_{out}(\Delta\lambda)$ with respect to $\Delta\lambda$. This result is shown in (62).

$$\frac{dI_{out}}{d\Delta\lambda} = -2RP_0 ln\,(2)\frac{\Delta\lambda}{\Delta\lambda_B^2} e^{-4\,ln(2)\left(\frac{\Delta\lambda}{\Delta\lambda_B}\right)^2} \tag{62}$$

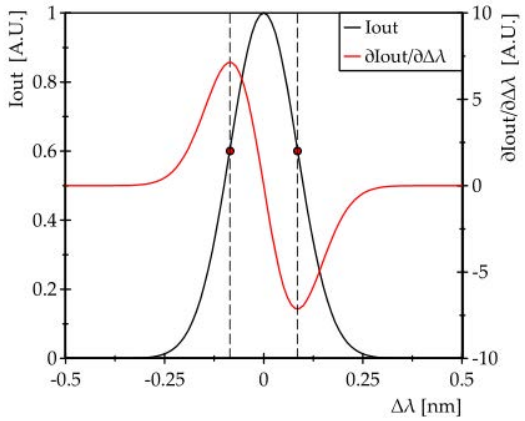

Fig. 41 Simulation of theoretical shape of the back-reflection response.

From the theoretical expressions, it can be graphically seen that the maximum points are at ±80 pm with respect to the Bragg wavelength ($\Delta\lambda$=-0.08 nm and $\Delta\lambda$=+0.08 nm). This result is obtained for $R\ P_o = 0.2$, $\lambda_B = 1540.95\ nm$ and $\Delta\lambda_B = 0.15\ nm$, This is shown in Fig. 41

5.3 Interrogation system implementation

The setup consists of a dual-comb architecture with two electro-optic modulators that are going to generate the sidebands that constitute both combs. Moreover, we use an acousto-optic modulator to ensure frequency shift between the two optical combs, this will enable the injective mapping and the multiheterodyne capability of the source. The sensor is read by means of a circulator. The overall system is depicted in Fig. 42. We use a polarization controller to optimize the visibility of the detected interferogram. The frequency rate of one comb is of 12.5005 GHz while the other comb has a frequency of 12.5000 GHz. The shift between combs is chosen at 42.5 MHz so that we can achieve a frequency of 12.5 MHz when the information is down sampled t 30 MHz. The laser source that is employed to irradiate the FBG sensor is a QDFBLD-1550-20 (QPhotonics). It is a DFB type of laser with a 10 MHz spectral linewidth at full width half maximum. The two electrooptic modulators (EOSpace phase modulators) that are employed to generate the combs were set to a 500 kHz difference to generate an RF comb with enough bandwidth to detect the ultrasounds. The photodetector is a 150 MHz InGaAs device and, finally, a down-sampling is performed with a PXI- 5105 module from National Instruments.

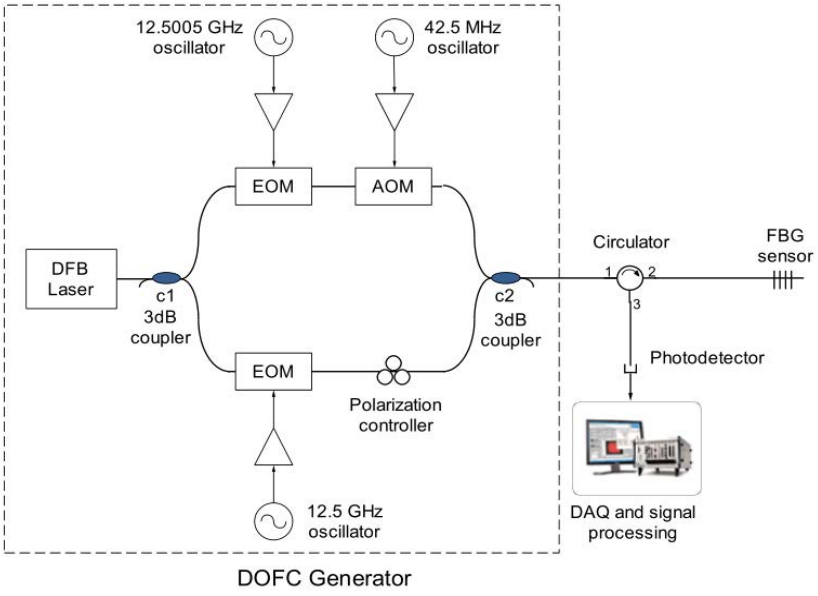

Fig. 42 Setup implementation of the dual-comb applied to fast FBG readout.

The interval of wavelengths in which the behavior is linear corresponds to an 80 pm range centered around the operating point. This corresponds to a 66 με range in strain magnitudes considering that the sensitivity of the FBG is around 1.2 pm/με at 1550 nm.

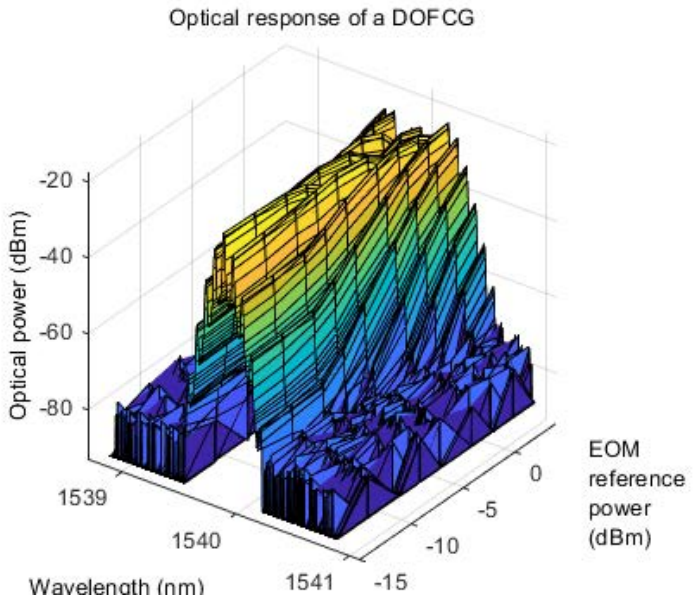

Fig. 43 Parametric sweep of the modulation depth response of a dual-comb optical domain.

The tunable characteristic of the dual-comb is depicted in Fig. 43. In this graph, we can observe how the depth modulation influences the number of lines of the comb and the amplitude of each one of the lines. From all these possibilities we choose the one that has a suppressed value of the order zero line and a maximized value of the order one line. This value corresponds to approximately 0 dBm of EOM power.

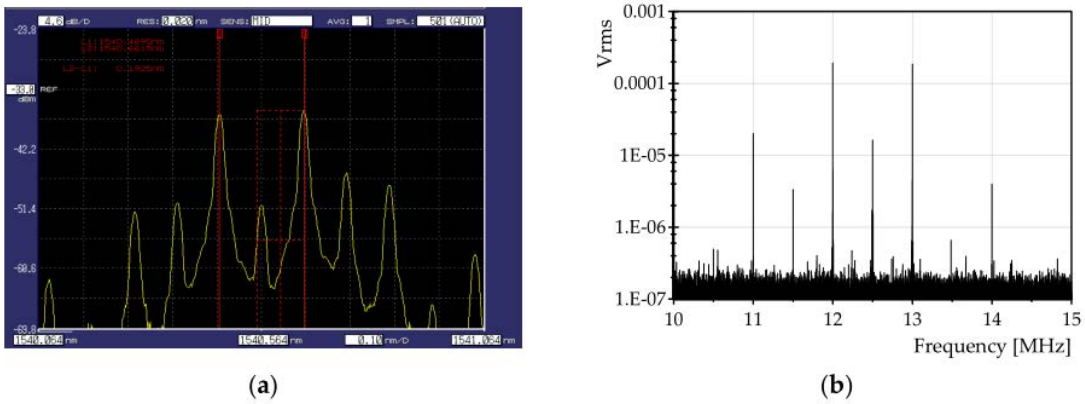

Fig. 44 Optimized dual-comb in the optical domain a), the image of the RF domain after down-sampling b).

The system generates two combs that have high suppression on the carrier and high amplitudes on the first sideband tones. The optimized comb can be seen in Fig. 44 where our goal is to obtain a comb where the comb lines corresponding to the first harmonics are maximized with respect to the other optical lines of the comb. In Fig. 44 a) we can observe the output of the dual-comb system in the optical domain and in Fig. 44 b) we can observe the photodetector readout on the third port of the circulator.

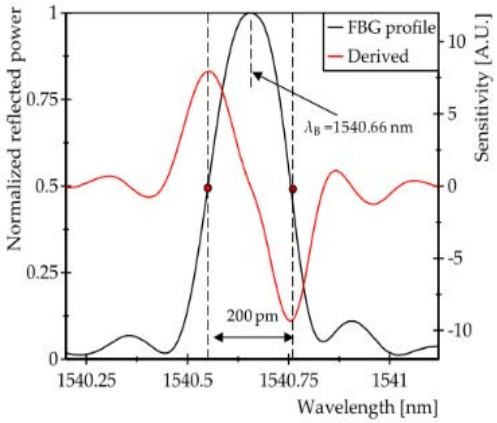

Fig. 45 Graph of the back reflected signal of the FBG and the first derivative in red.

From the real measurement, one can observe that the needed spacing between the optical lines is about 200 pm at 1540.66 nm of Bragg wavelength. The graph was measured with a 20 pm resolution. This figure is used to find the maximum slope points that were found at 25 GHz apart centered in the Bragg wavelength. This requires that the zero-order tone of the comb is aligned with the Bragg wavelength and the first-order harmonics are separated 12.5 GHz each in order to be placed in the correct point of the spectrum (Fig. 45).

5.4 Demodulation system

The detection scheme consists of an AM demodulator implemented digitally. We acquire the photo-detected signal by means of a 12 bits ADC and save a data buffer for future digital processing. We select the two channels of interest that correspond to the specific optical modes. We mix them with a stable frequency reference and finally, we filter the signal with a low pass filter that eliminates the higher harmonics. We finally subtract both signals, scale and plot the result. This process is shown in Fig. 46.

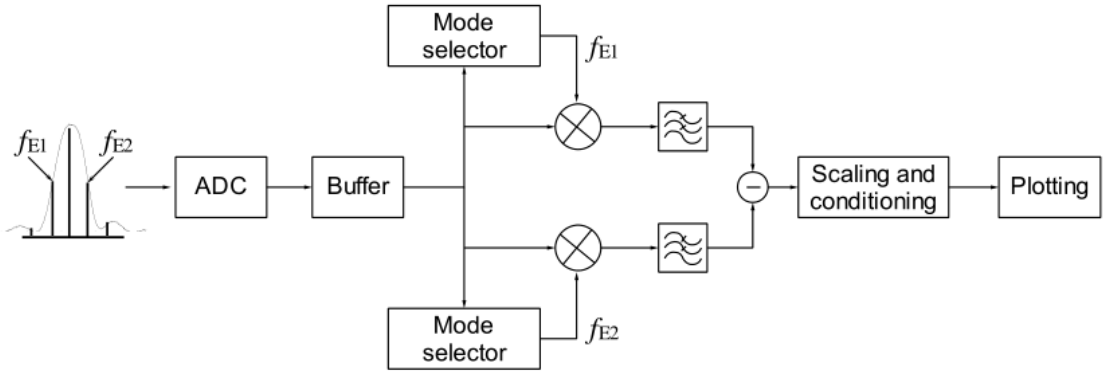

Fig. 46 Demodulation stages for AM recovery of the strain.

This differential measurement technique is useful when we consider the common-mode sources of noise. One common mode source of error is the laser amplitude fluctuation. With the differential measurement, we can take advantage of the fact that the variation has the same sign in both channels and therefore it will be nullified when both channels are subtracted. To demonstrate this, a 200 Hz mechanical vibration was injected with 6.5 kHz of common-mode modulation to simulate the common noise in both channels (this process is shown in Fig. 47 a)). When evaluating the suppression between a single channel operation versus a two-channel differential operation a 16 dB attenuation was observed in the unwanted common-mode harmonic. This attenuation is shown in Fig. 47 b).

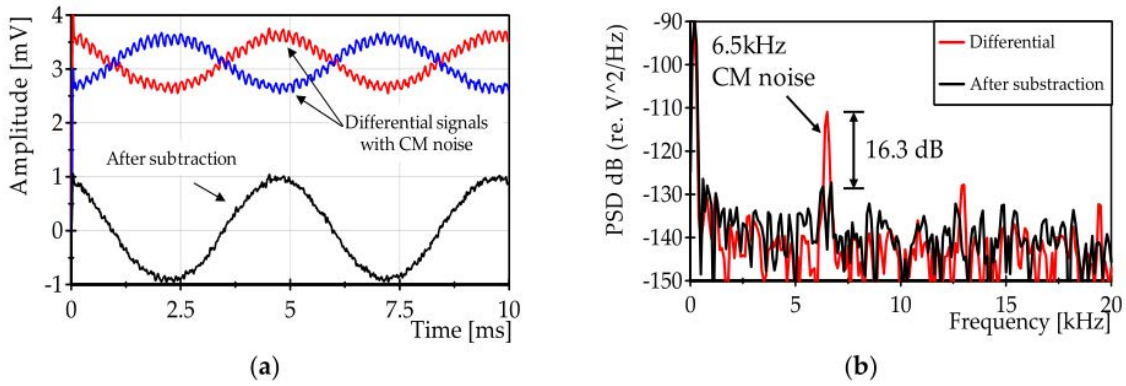

Fig. 47 Common mode error cancelation based on a differential measurement. a) time-domain b) frequency domain.

5.5 Experimental results

Two setups were prepared in order to measure vibrations and ultrasound mechanical signals. The first one consists of a test bench where the FBG is stuck to a moving part on one end and a fixed part on the other end that has specially designed screws that pre-stress the optical fiber sensor.

The length between the extremes of the FBG sensor is 10cm. This setup achieves frequencies of 2 kHz (Fig. 48 a)). In the second setup prepared for ultrasounds, an FBG stuck to a carbon fiber plate of dimensions 7 mm x 150 mm x 210 mm. The FBG was stuck with cyanoacrylate to the surface along 4 cm of the length of the fiber and the total length of the FBG was 2cm.

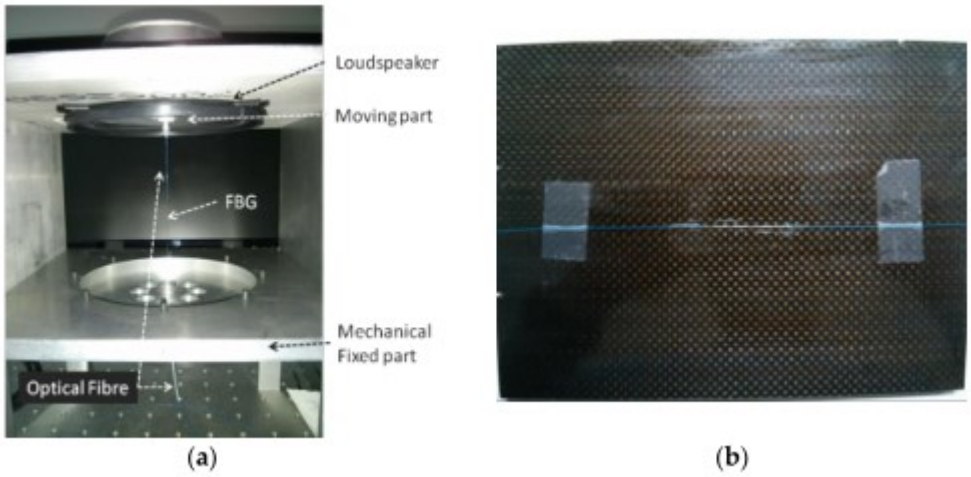

Fig. 48 Vibration measurement setup a) and ultrasound measurement setup b).

Fig. 49 a) shows an example of both differential signals at 1 kHz from two optical lines placed at the maximum slope points of an FBG sensor. And Fig. 49 b) shows the resulting waveform after subtracting both differential signals. It can be seen that the amplitude, and therefore the sensitivity of the resulting signal, is twice the amplitude of each single signal. This effect constitutes an amplification of the measurement without the need for an additional amplifier and at the same time, it provides a high common-mode rejection. The amplitude of the signal is about 28 με.

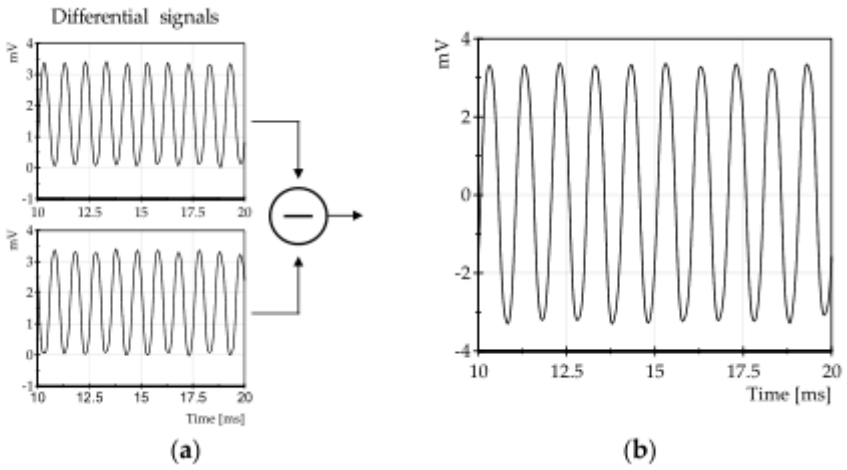

Fig. 49 Differential measurements obtained at 1 kHz of mechanical vibration a), Resulting signal obtained from the subtraction of the differential waveforms b).

To evaluate the maximum resolution of the system two resonance frequencies of two different PZT were tested. The result is a system that can detect ultrasound burst signals from 40 kHz to 120 kHz. The signals are depicted in Fig. 50 and are applied with a piezo-stretcher device. In Fig. 50 a) we can see a 0.4 $\mu\varepsilon$ burst in time domain and in Fig. 50 b) we can observe a 0.34 $\mu\varepsilon$ of detected amplitude also in time domain. And in Fig. 50 c) and Fig. 50 d) show the frequency domain of the detected burst. In the case of the first measurement, we can see a SNR of 30 dB and in the case of the second measurement we can see an SNR of 22 dB. In the first measurement we can observe a burst width of 2 ms while in the second measurement we can see a burst width of 1 ms.

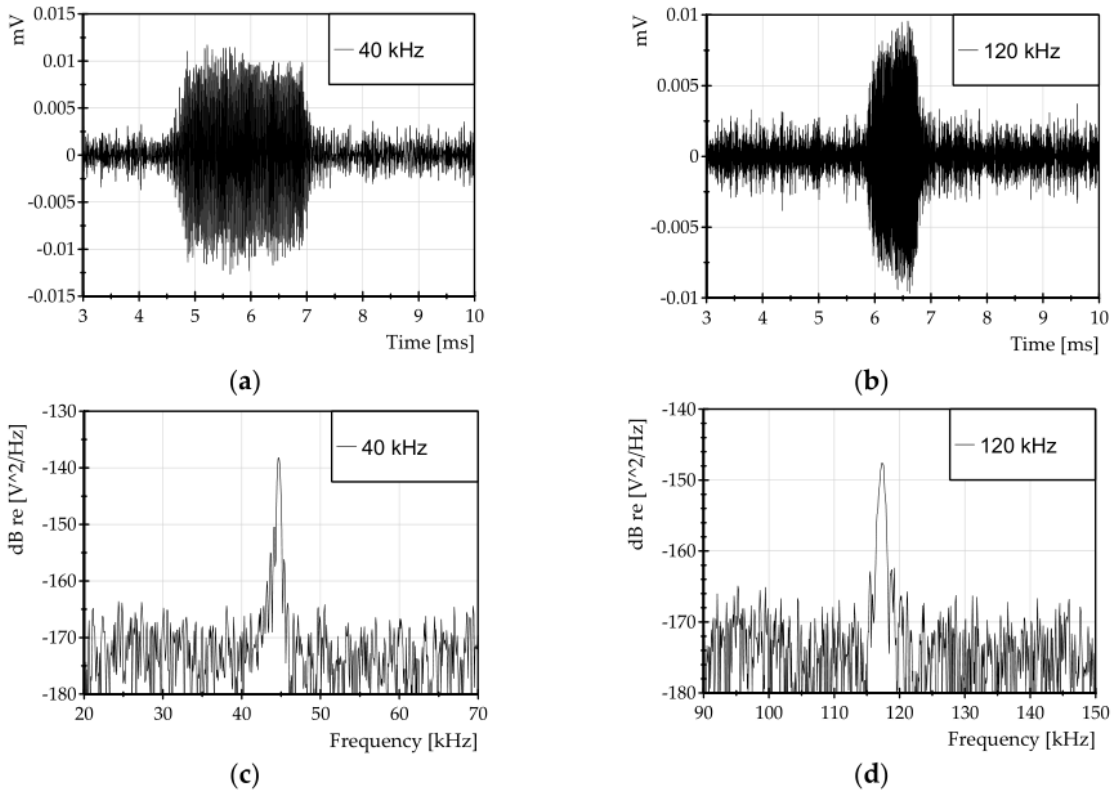

Fig. 50 Measurements of ultrasound bursts.

5.6 Discussion

The back-reflection response of an FBG sensor is dependent on the strain applied. Moreover, if the strain applied to the sensor is not uniform, but a gradient, the shape of the back-reflection response will change accordingly as shown in Fig. 51

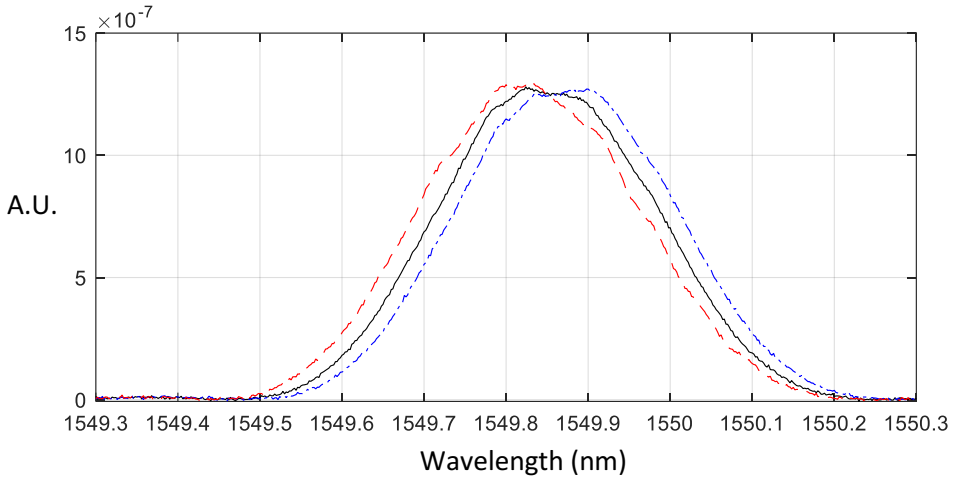

Fig. 51 Back-reflection profile of an FBG sensor supporting strain. Black trace: reference trace that corresponds to the initial position. Red trace: trace correspondent to a compression applied over the FBG, Blue trace: trace correspondent to traction applied to the FBG.

A careful inspection of the graph indicates that besides the displacement of the Bragg wavelength, the gaussian function changes its symmetry. This effect is easily observed as the slope of the reference function is not equal to the slope of the measurement trace.

However, for a uniform strain application with respect to the length, we can assume just the Bragg wavelength shift paradigm of operation. We can, therefore, use a dual optical frequency comb to perform a spectroscopic measurement over the wavelength interval. In this case, 12 GHz sidebands spacing is chosen, a mapping frequency of 1 MHz is employed and a 50 kHz electrical spacing it has been set. The result with arbitrary traction and compression leads to a behavior similar to the one shown in Fig. 52

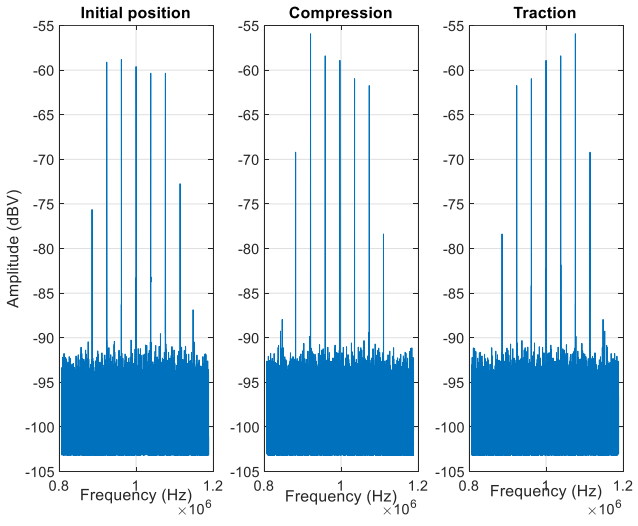

Fig. 52 Dual comb readout of a uniform FBG sensor

It can be seen clearly that the center of gravity of the comb changes with respect to the strain applied. If we register the strain applied to the sensor and we register the frequency of the center of gravity we obtain a calibration curve as the one shown in Fig. 53 a). This procedure can be used to measure over a span of almost 1000 $\mu\varepsilon$ that is measured with a micrometer screw. This is

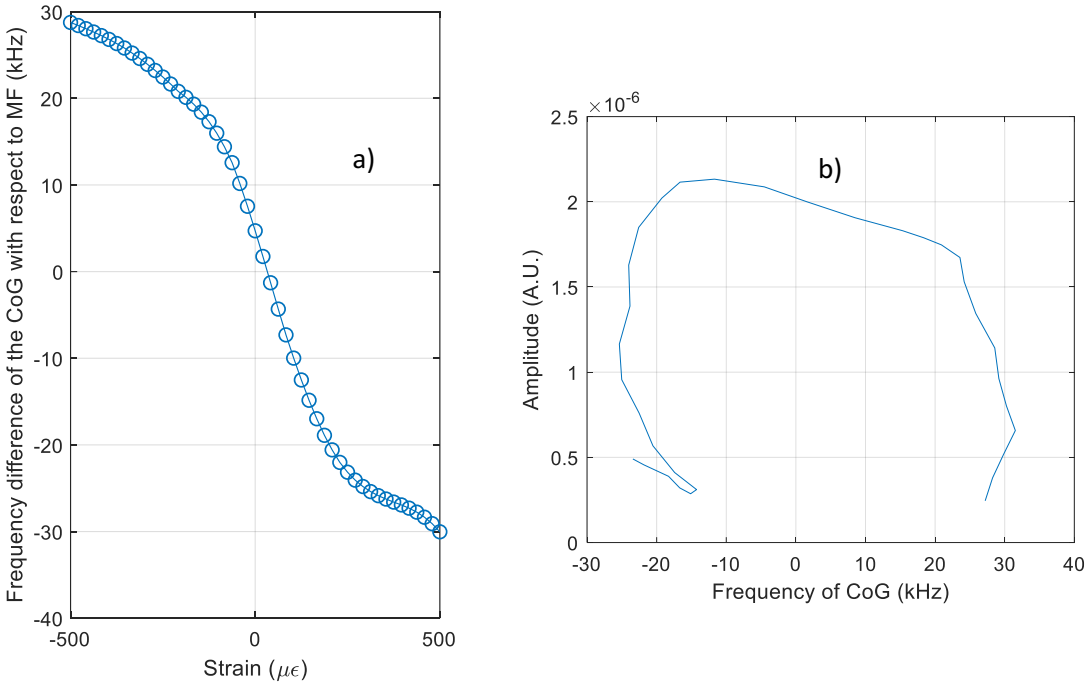

Fig. 53 Center of gravity of frequency a) One dimensional center of gravity of the FFT window b) Two-dimensional center of gravity amplitude and frequency. COG center of gravity, MF mapping frequency.

equivalent to a Bragg wavelength displacement of 1 nm. It can be observed that the range of linearity is almost 500 $\mu\varepsilon$. For extending this range of operation to virtually all the range when the FBG overlaps the comb we can use the power amplitude center of gravity as in Fig. 53 b). Each point of this trajectory can be associated with a particular value of strain, therefore clustering a specific acquisition point into some part of the trajectory provides a specific value of strain applied.

5.7 Conclusions

In this chapter, the implementation of an electrooptic dual optical frequency comb architecture applied to read FBG sensors was presented.

Results were presented for dual-comb operation under optimized control. The optical modes are mapped onto detectable tones that are multiples of 0.5 MHz around a center radiofrequency tone (40 MHz). Measurements of ultrasounds (40 kHz and 120 kHz) are demonstrated with this

sensing system. Ultrasounds induce dynamic strain onto the fiber, which generates changes in the reflected Bragg wavelength and, hence, modulates the amplitude of the OFC modes within the reflected spectrum. The amplitude modulation of two counterphase tones is detected to obtain a differential measurement proportional to the ultrasound signal.

The FBG sensors behave in a different way if gradients are applied to the sensing part of the sensor. This translates into changes in the linear-zone-slopes of the back-reflection profile and at the same time a shift in the Bragg wavelength.

The drawbacks of this system are its complexity and the fact that the acousto-optic modulator is a non-integrable device. In next chapters it will be shown how to implement the same functionality with the use of a serrodyne modulation / phase generated carrier (PGC) modulation to shift the optical frequency. These approaches result into more compact setups, and they will be done by using a single modulating device.

Chapter 6: Phase generated frequency shifted dual comb implementation

“If you want to go fast, go alone. If you want to go far, go together.” —African Proverb

6.1 Introduction

This chapter discusses the use of a serrodyne modulation or phase generated carrier to generate an optical frequency shift that is necessary for unambiguous detection with electro-optic dual optical frequency combs. Several measurements are presented: the dependence of the optical output and electrical output with the modulating parameters of the source, the output dependence with the bias voltage, and the frequency mapping dependence with the serrodyne modulation, among others. Stability is also discussed, and the harmonic distortion is shown for the case of an all-electro-optic dual optical frequency comb.

Dual drive modulation for dual-comb generation is presented and its limitations and advantages are discussed. This is done by using two modulating signals that generate the optical sidebands and an auxiliary signal that performs a frequency shift to the electrical comb that allows to read the information from the electrical domain.

6.2 Pseudo multiheterodyne generator

The process of generating an electro-optical dual optical frequency comb generator involves the need of three modulating signals that are intended to generate the optical sidebands and the electrical signal needed to generate a displacement over one of the combs to have the multiheterodyne source.

In the case of the serrodyne translation [43], we use one phase modulation to generate a frequency translation over one of the combs and, this way, to obtain a multiheterodyne signal between the unshifted and the shifted comb.

6.2.1 Principle of operation

The dual-drive MZM can be used to generate a comb [9], [44]–[46]. It is normally used to control the flatness and usually as an extra modulating stage to broaden the optical comb. However, due to their internal structure, those devices may be used for dual-comb generation. The acousto-optic effect may be functionally substituted by a shifting process [47] with an independent signal which can be either a saw-tooth signal or a sinusoidal function.

Those implications have the result of being able to reproduce the functionality of a dual-comb with either two-phase electro-optic modulators or a single dual drive Mach-Zehnder-modulator if we choose an integrated setup.

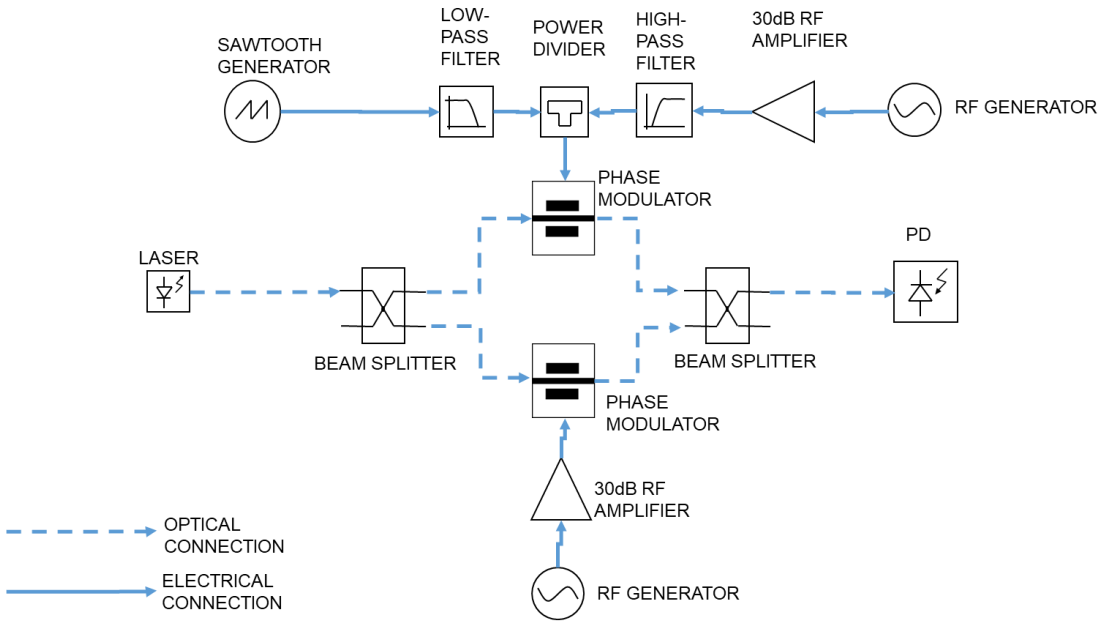

Fig. 54 Discrete implementation of all electro-optical dual optical frequency comb with discrete optical components.

The discrete implementation uses the architecture of Fig. 54. It is composed of two phase-modulators. Each one has a sideband generating a signal of 12 GHz approximately. One of them has also its pseudo-carrier generating signal that allows the one-to-one electrical mapping signal. At the photo detected output, we can see the electrical comb associated with the optical dual comb. The spacing of the optical combs is imposed by the frequency of each RF generating signal. While the frequency spacing of the electrical comb is controlled with the difference between the RF frequency. The mapping frequency is a function of the repetition rate of the saw-tooth signal or the phase generated carrier. And can be adjusted in terms of visibility at each frequency depending on the phase difference of the interferometer and its polarization. Each electrical tone carries information about the optical amplitude and phase of the optical wavelengths.

In Fig. 55 a) we can see a typical behavior of a dual-comb in the optical domain. It is noteworthy, to remark that the two combs are not seen as two entities as the resolution of the device is 20 pm and the spacing frequency homolog tones is 10 kHz for modes +1 and –1. In Fig. 55 b) We can find the response of the electrical tones corresponding to each pair of optical tones. The central wavelength of the combs is imposed by the wavelength of the laser seed and in this case,

coincides with 1539.9 nm. The optical separation is 0.1 nm in optical domain, and we can observe a total of 17 optical tones

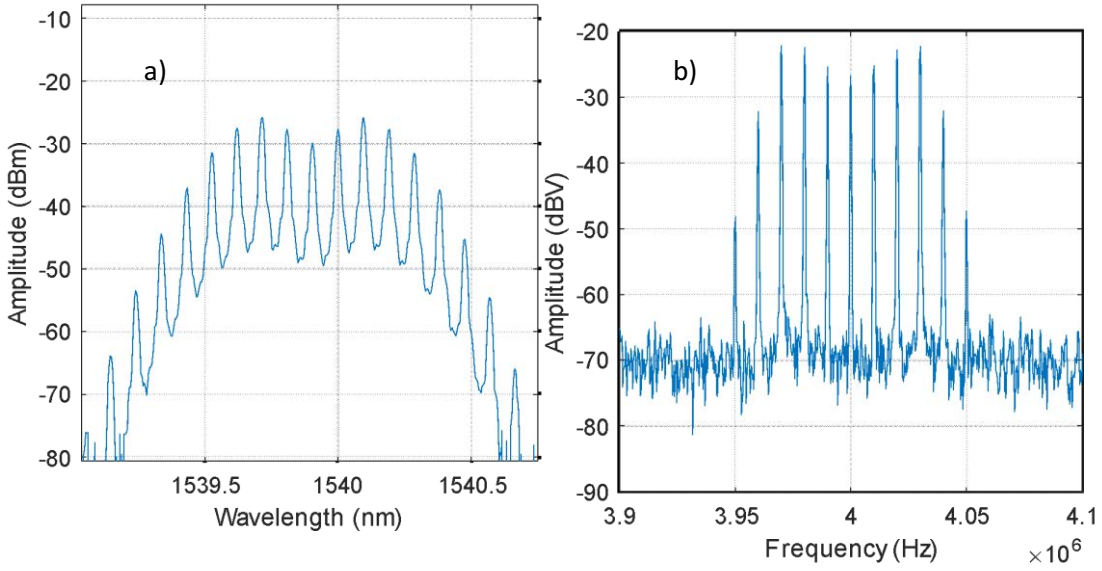

Fig. 55 Response of a dual optical frequency comb in optical domain a) and response of a dual optical frequency comb in electrical domain b).

For the discrete implementation, we can see that several modes are generated in the sideband pseudo carrier generating process. Therefore, the serrodyne shift is not ideal as other integer multiples of the main frequencies are generated from the sawtooth injected signal. This process is performed in the case of the discrete implementation with a certain efficiency with a total harmonic distortion of 0.05%. This corresponds to a 15 dBc considering as carrier the first-order harmonic of the highest amplitude. In Fig. 56 a) we can observe the process of optical shifting at a frequency of 4 MHz and in Fig. 56 b) we can see the frequency domain of the optical photo-detected signal.

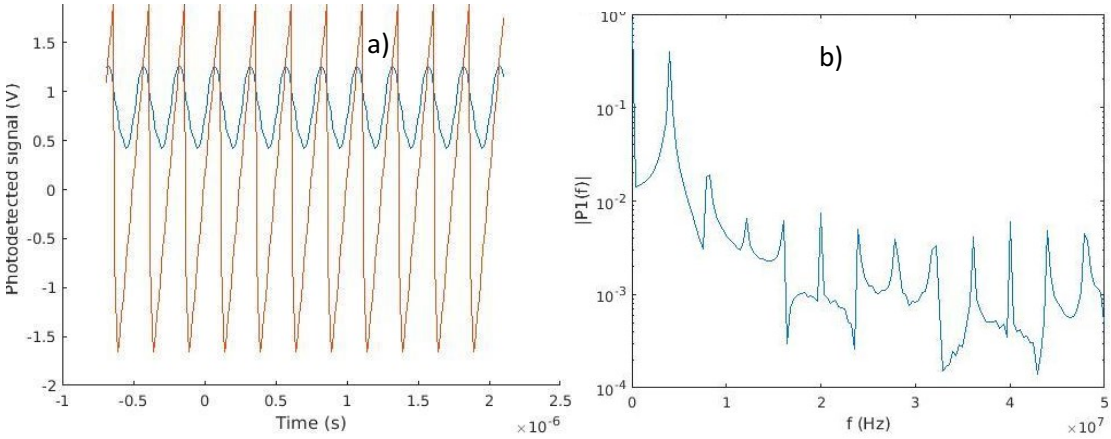

Fig. 56 Serrodyne frequency shift implemented with discrete components. a) Time-domain b) frequency domain.

6.2.2 Simulation of a pseudo multiheterodyne generator

I. Electrical implicit form

Assuming that the electro-optical dual-comb behaves as a multimode multiheterodyne Mach-Zehnder interferometer [48] one can easily reach an expression for the electrical signal. (63) shows the dependence on the electrical signal with the optical parameters of the light, and radiofrequency input signals.

$$I_{DOFCG} = \|A_1\|^2 + \|A_2\|^2 + 2\|A_1\|\|A_2\| \cos\left(\beta_2 \sin(\omega_2 t) - \beta_1 \sin(\omega_1 t) + 2\pi t(\nu_2 - \nu_1) + \phi_2(x) - \phi_1(x)\right) \quad (63)$$

$\|A_1\|$ and $\|A_2\|$ is the electrical field amplitude of each of the beams that correspond to each one of the arms of the interferometer. $\beta_2 \sin(\omega_2 t)$ the term corresponds to the sideband generating a signal of the second arm of the interferometer. β_2 represents the amplitude of the phase modulation also known as depth modulation and ω_2 represents the frequency of the oscillation of the phase modulation. Similarly, $\beta_1 \sin(\omega_1 t)$ the term corresponds to the sideband generating a signal of the first arm of the interferometer. β_1 represents the amplitude of the phase modulation

also known as depth modulation and ω_1 represents the frequency of the oscillation. $(\nu_2 - \nu_1)$ is the frequency difference of the beams of the interferometer. And $\phi_2(x) - \phi_1(x)$ is the optical phase difference of the light beams.

(63) allows us to see the dependence between the optical modes and the electrically generated spectra.

II. Electrical explicit form

If we apply simplification of Jacobi-Anger expression, we can relate (64) with its Fourier expansion (64). This expression is more useful as every frequency $((\nu_2 - \nu_1) + 2\pi(\omega_2 - \omega_1)k)$ can be associated with a phase difference $\phi_2(x) - \phi_1(x)$ which is the same as the optical phase.

$$I_{DOFCG,ESA} = 2\|A_1\|\|A_2\|\left(\sum_{k=-\infty}^{\infty} J_k(\beta_2)J_k(\beta_1)cos\,(\,2\,\pi t((\nu_2 - \nu_1) + 2\pi(\,\omega_2 - \omega_1)k\,) + \phi_2(x) - \phi_1(x))\right) \quad (64)$$

$J_k(\beta_1)\ \|A_1\|$ is related with the k-th optical teeth amplitude of the first optical comb and accordingly $J_k(\beta_2)\|A_2\|$ is related to the k-th optical teeth amplitude of the second optical comb. (64) is a more generic form of dual-wavelength interferometry response.

III. Simulation as a dual optical frequency comb

The dual comb can be simulated to see typical behavior. The electrical domain reproduces the behavior of the optical domain and as the modulation depth increases the broadness of the comb also does. In Fig. 57 different depth modulation states of the dual-comb can be seen. The depth modulation β is considered the same in both arms and it is increased in steps of 0.125 V_π, which corresponds to 0.3 V in amplitude variation. Therefore, the broadness of the optical source is fully controllable with the modulation depth of the modulators.

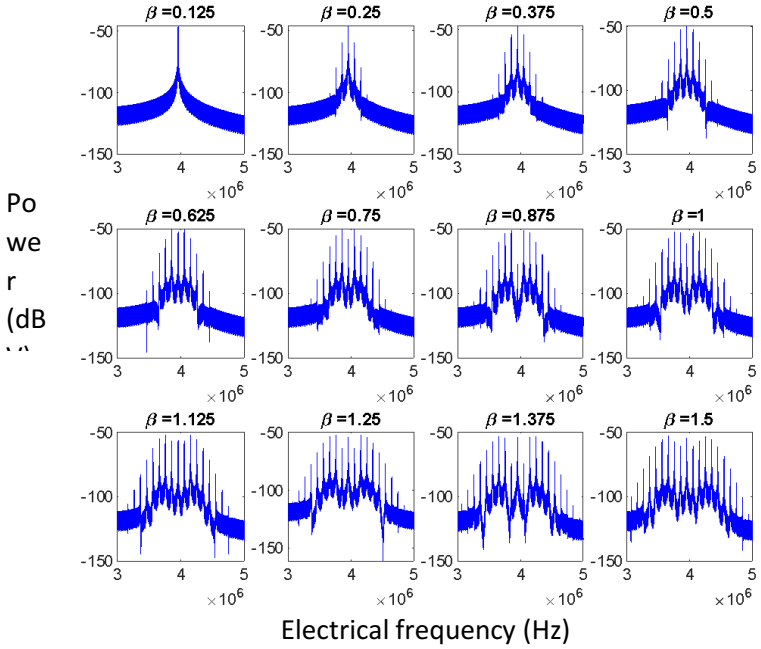

Fig. 57 Simulation of dual optical frequency comb electrical frequency domain for different depth modulations.

On the other hand, the difference between the modulating RF signal imposes the comb teeth separation. This separation Δf is equal to the difference between the first and second modulator frequencies. This fact can be seen in Fig. 58. In this figure, the number of teeth does not change but the electrical comb lines separation changes accordingly.

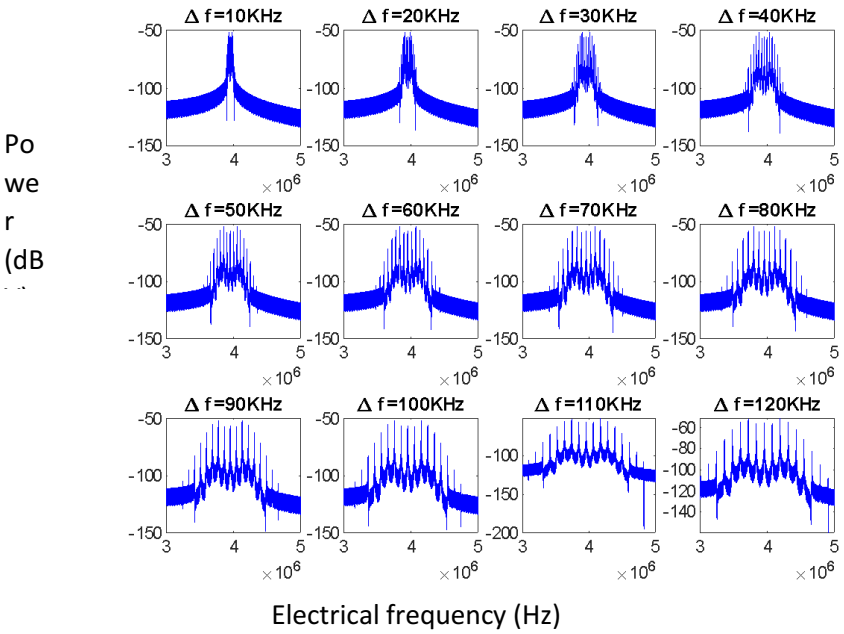

Fig. 58 Frequency difference variation simulation of the electrical response of a dual optical frequency comb.

It is noteworthy to point out that the optical combs do not change significantly compared to the initial position as the kHz range changes are insignificant with the absolute frequencies of tenths of GHz.

The degree of freedom that is added to our setup is the ability to choose the mapping frequency, which is not available in classical acousto-optic implementation. If the sawtooth signal frequency is changed, it will reflect a change of the electrical mapping frequency as shown in Fig. 59.

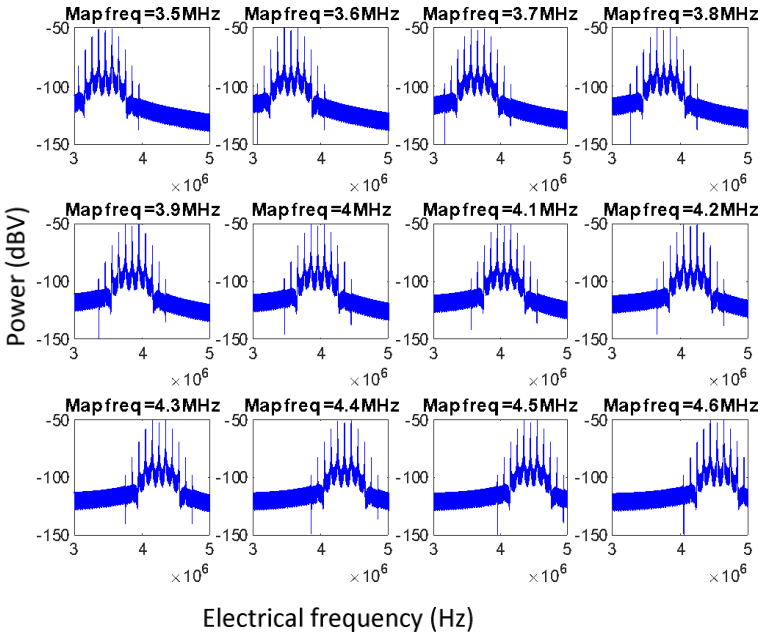

Fig. 59 Frequency mapping variation of a serrodyne implementation of a Dual optical frequency comb (simulation).

6.3 Dual drive Mach-Zehnder compact implementation

The saw-tooth signal is injected into a power splitter employing a filter that can load the generator and avoid at the same time RF losses from loading the sawtooth generator with the high-frequency signal. The discrete component implementation is substituted by the dual drive MZM which has internally the Mach-Zehnder with individual arm modulation capability. The setup is shown in Fig. 60.

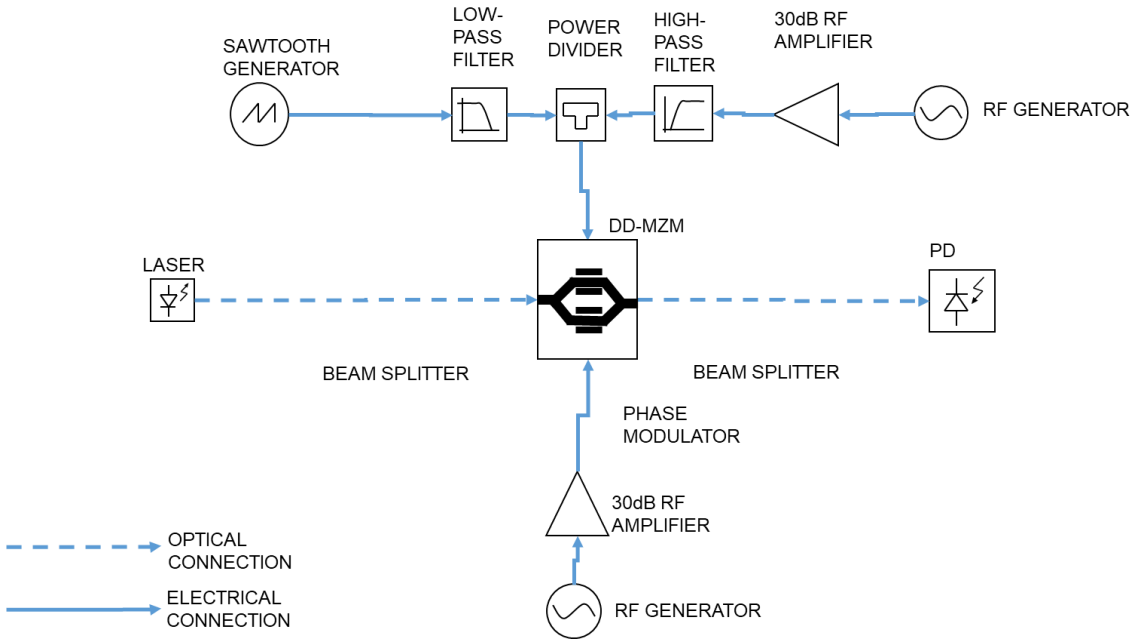

Fig. 60 Discrete implementation of all electro-optical dual optical frequency comb with in-chip optical component.

Another important fact is that the pseudo carrier approach allows choosing the mapping frequency on demand and adds another degree of freedom to the classical dual-comb implementation system whose mapping frequency is usually fixed. If we change the pseudo carrier parameters either frequency or amplitude, we can change on wish the mapping frequency and at the same time maintain the optical spectrum unchanged. As seen in Fig. 61 a) the dual-comb, generated at 1311.5 nm remains unchanged in the optical domain as the mapping frequency changes in value as shown in Fig. 61 b).

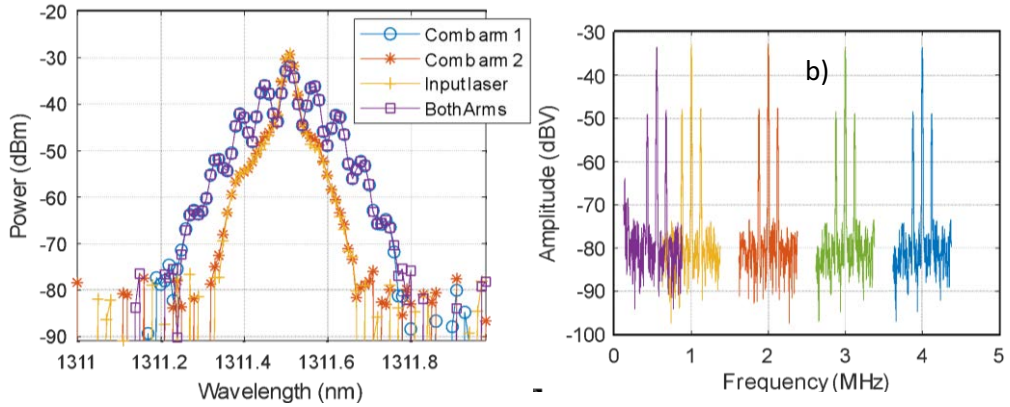

Fig. 61 Dual comb response and the independent combs a) optical response b) electrical response of the dual comb mapping process for different pseudo carrier frequency.

When the pseudo carrier signal is generated with a saw-tooth generator, the photo detected response is as the one shown in Fig. 62. If we maintain constant the frequency and amplitude of the saw-tooth signal and we vary the frequency difference between the RF signals, we obtain a variation in the width of the electrical teeth separation.

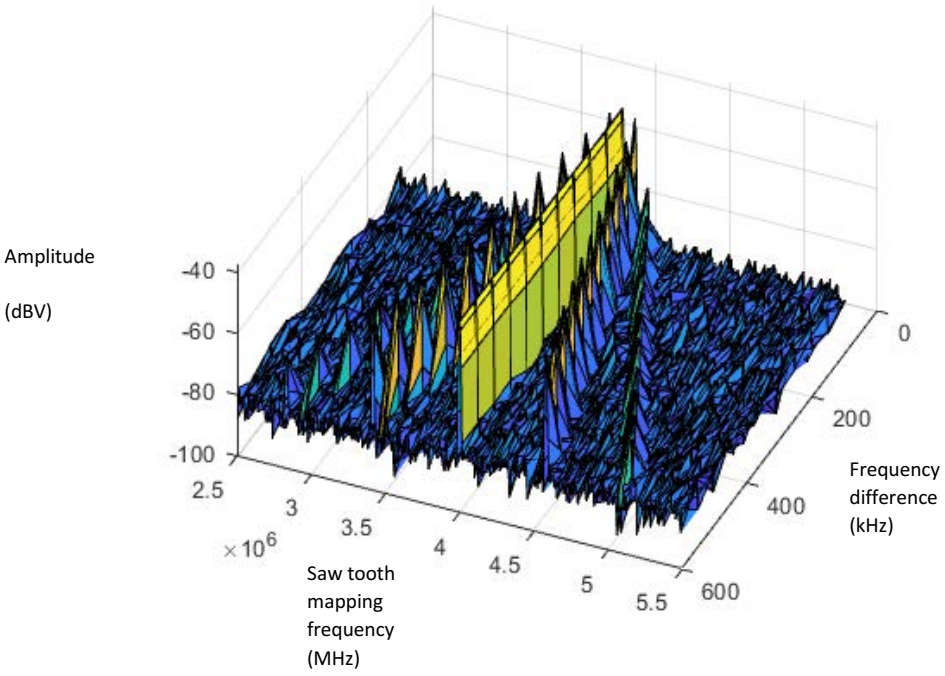

Fig. 62 Response to the serrodyne implementation of an electro-optical dual-optical frequency comb to changes in sideband frequency modulation.

For a sinusoidal input signal, we obtain a phase generated carrier which is a single band modulation around DC. A sweep in the RF frequency difference was made and the response can be seen in

Fig. *63*. We can observe that the repetition frequency is 4 MHz for the PGC pseudo-carrier. When the frequency difference of the RF signals is greater than the pseudo-carrier the electrical comb invades their adjacent images and intermixing can happen. In this case, it happens at frequencies of 4 MHz/8 as we have 2 sideband modes on each of the sides of the carrier.

The repetition frequency of the pseudo carrier coincides with multiples of the primary generated frequency in this case 4 MHz.

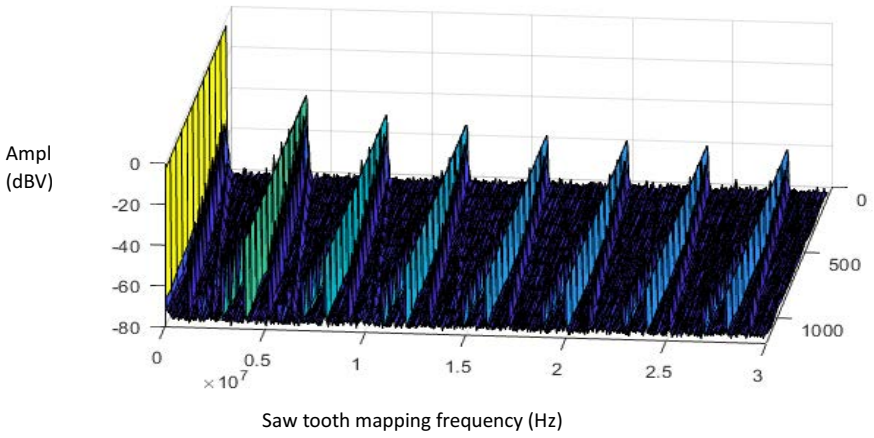

Fig. 63 Response to the serrodyne implementation of an electro-optical dual-optical frequency comb to changes in sideband frequency modulation

.

One might want to know the amplitude fluctuations of the electrical frequencies of the teeth of the combs with changes in the wavelength. To evaluate this parameter, we maintain the modulating values constant, and we vary the wavelength of the laser in steps sweeping a total interval of 4 nm over the optical span, the results are seen in Fig. 64.

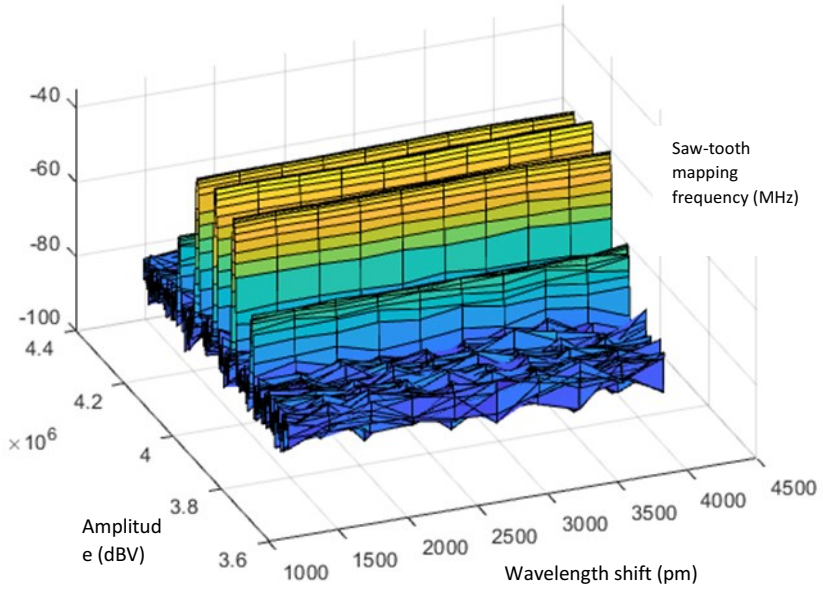

Fig. 64 Response to the serrodyne implementation of an electro-optical dual-optical frequency comb to changes in wavelength in the laser.

One may want to know the dependence between the optical phase difference of the two paths and the amplitude of the modes. To obtain that characterization we can register the amplitude of the electrical tones and we vary the bias voltage of the device in steps of 250mV, which is equivalent to approximately $\pi/10$ rad of optical phase difference. The dependence can be seen in Fig. 65. As can be seen, for certain phase differences of $\pi/5$ rad with respect to the path balance at 0 mV it can be seen that approximately 5 dB of fluctuation happens to all of the modes. And therefore, this parameter is far more important for amplitude stability than the optical wavelength for the particular case in which the optical paths are balanced as is the case of this photonic integrated circuit. The optimization can, therefore, be done by setting a point in which the derivative of the amplitude function with respect to phase difference is low. As it is at 0 mV or near 2500 mV or in radians 0 rad or π rad respectively.

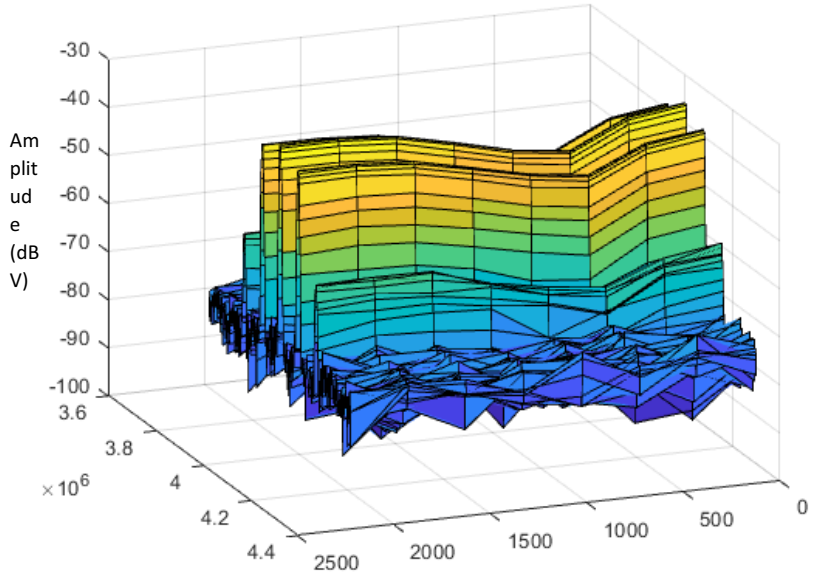

Fig. 65 Response to the serrodyne implementation of an electro-optical dual-optical frequency comb to changes in bias voltage of the modulator.

Another very important characterization is the dependence of the depth modulation and the amplitude of the electrical mapping domain. This characterization permits us to know the number of optical tones that are generated and at the same time the broadness of the optical source that is generated. In this case, it is done by varying the mean RF power defined as (65)

$$\underline{P_{RF}[dBm]} = \frac{P_{RF,1}[dBm] + P_{RF,2}[dBm]}{2} \tag{65}$$

The results can be seen in Fig. 66. As the RF modulation average power increases, the broadness also does. That is because the depth modulation increases in value.

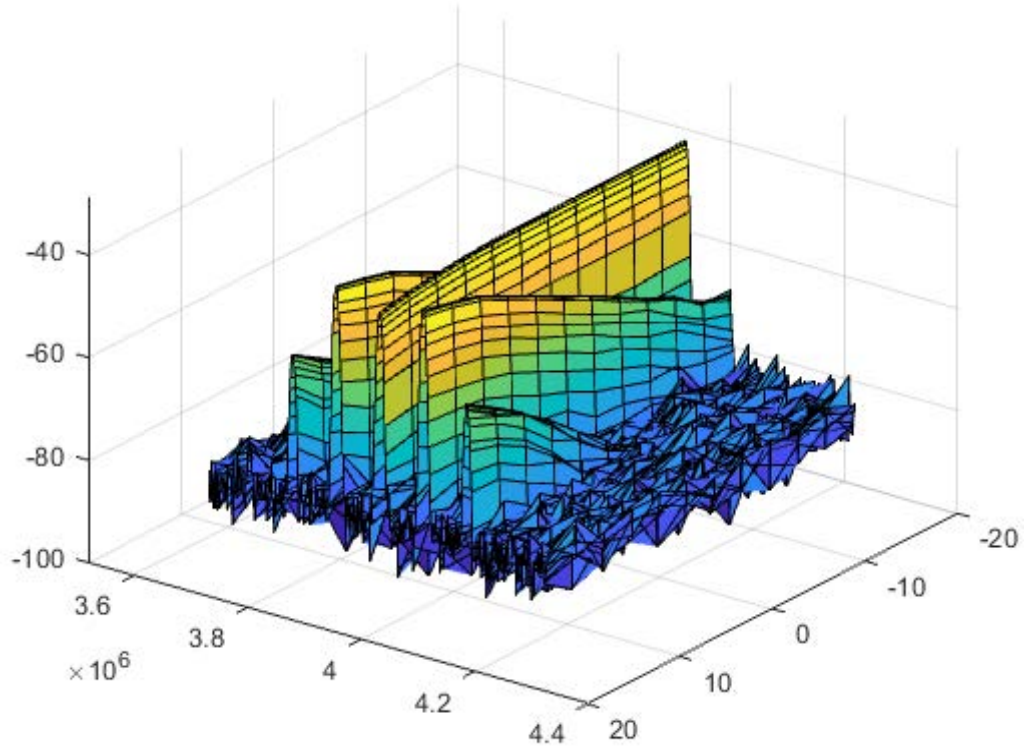

Fig. 66 Response to the serrodyne implementation of an electro-optical dual-optical frequency comb to changes in the average modulating power.

6.4 Stability of compact implementation

Any perturbation in the input values due to noise or environmental parameters such as vibrations in the setup or temperature changes may vary the properties of the optical source. This mainly translates into amplitude fluctuations or phase differences.

The homodyne stabilization of phase using an active device such as a piezoelectric actuator over one of the arms can be done easily with an integrator or low pass filter [49]. The reference signal is compared with any of the RF harmonics mixed with a local oscillator of the seam frequency that allows us to read the phase difference directly in DC. Under unstable conditions (Open Loop) the phase fluctuates randomly according to phase and strain environmental variations see the hashed line of Fig. 67. On the other hand, once the closed-loop control is activated the error tends to stability (0 V level of Fig. 67). For all the seven arbitrary perturbations induced on purpose over one of the arms, the system recovers the stability compensating the phase difference towards zero error signal.

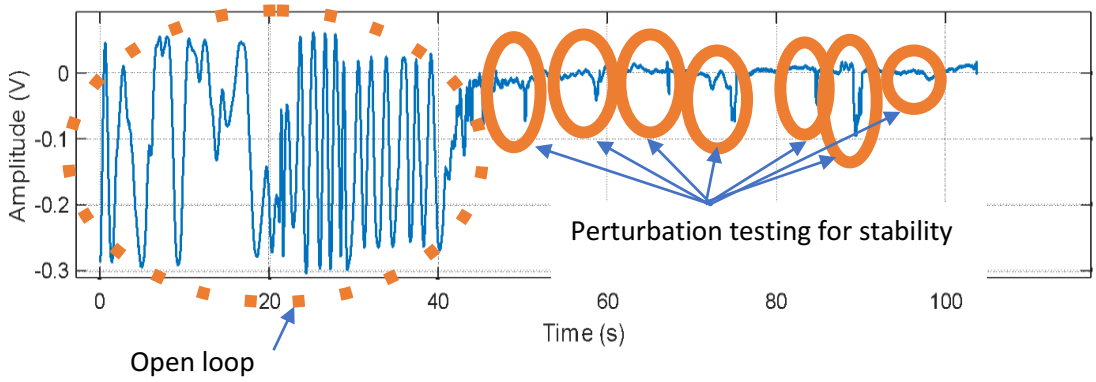

Fig. 67 Time response of a stabilized optical phase modulation discrete implementation of dual optical frequency comb.

When the in-chip implementation is used no PZT actuator can be included in the path difference. However, even if a freewheeling operation is considered, the phase stability is higher in the case of the discrete freewheeling implementation. As for the same interval of time, we have less fluctuation in the case of the in-chip implementation of the architecture than the architecture based on discrete components. The fluctuations of the central mode are registered over one-hundred-minute interval in Fig. 68. Those fluctuations are of less than 1 dB for the in-chip implementation and about 2.5 dB maximum value in the case of the discrete implementation.

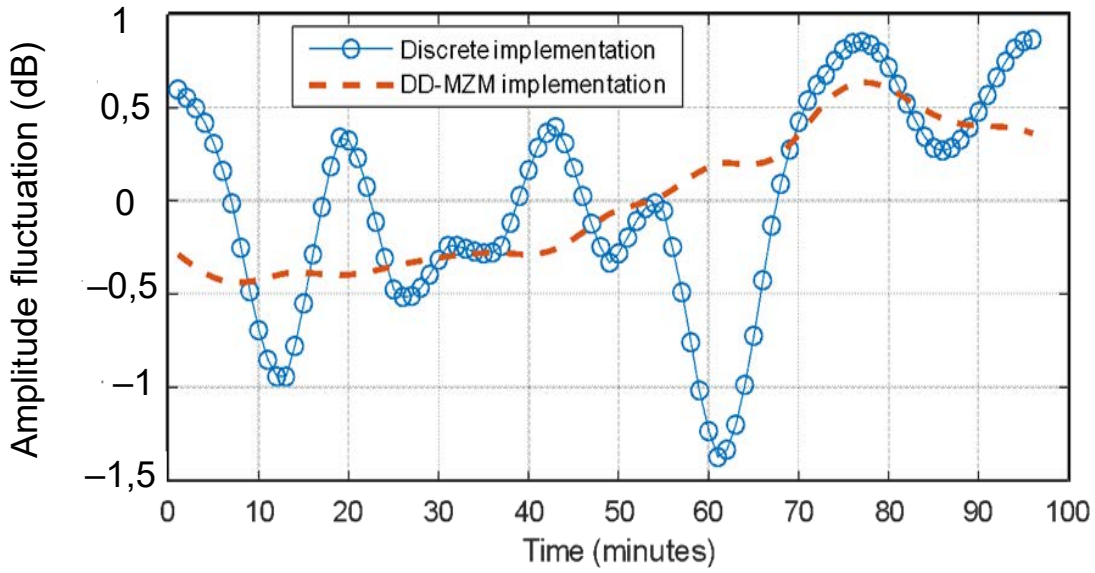

Fig. 68 Amplitude stability in time domain.

In the case of the in-chip implementation, we can observe that the total harmonic distortion is different depending on the frequency of the sawtooth signal and different depending on the RF input that is used. Therefore, we can conclude that the device, by fabrication, is not symmetrical and the same input signal does not produce the same output signal. A higher signal-to-noise ratio is obtained at 4 MHz for the second RF input. The best-achieved configuration is obtained for 30 dBc and 60 dB of signal to noise ratio. Fig. 69 a) shows the different outputs of the system for different excitation frequencies applied to the first arm of the device and on the other hand in Fig. 69 b) the same signals applied over the second arm of the device. The best configuration is obtained in the last case.

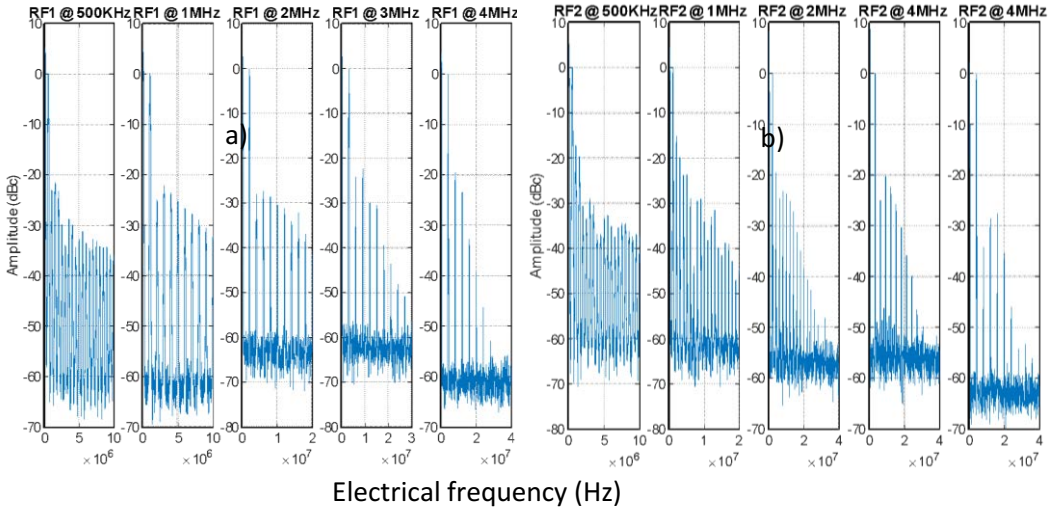

Fig. 69 Serrodyne frequency shift implemented within- chip implementation. a) First RF input, b) Second RF input.

Another noteworthy aspect is that the bias voltage of the device also modifies the conditions of signal to noise ratio and dB with respect to carrier and therefore at each frequency bias voltage should be swept to find the best conditions of operation.

The process of phase generating carrier (PGC) is considerably different from the serrodyne phase generating carrier as it leads to several pseudo carriers. The first seven clouds of harmonics created on a dual-comb PGC can be seen in Fig. 70. The 0 dBc harmonic is considered the principal carrier. In this case, the total harmonic distortion is higher as the suppression of the secondary, tertiary and other N carriers is lower than in the optimized case of the saw-tooth signal.

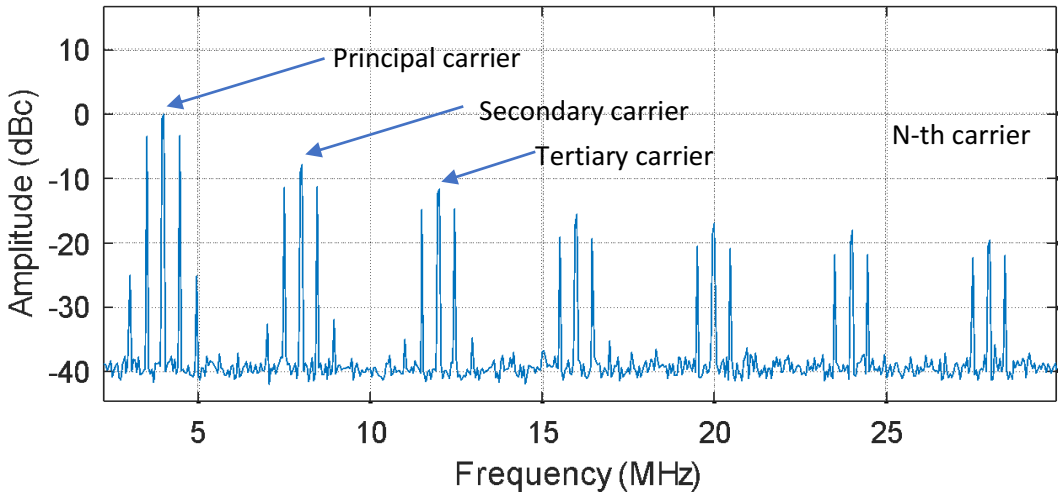

Fig. 70 Behavior of a phase generated carrier electrical spectra of a dual comb.

It can be easily seen that in the case of the serrodyne implementation the suppression between the principal carrier and the others is about 30 dB in the best case. While in the case of PGC is less than 10 dB. It is noteworthy, to see that the relationship between the carrier and the sidebands is maintained in each cloud of harmonics. This is because the same optical spectra are mapped to each different carrier. This process is expressed as (66).

$$I_{DOFCG,ESA,T} = 2\|A_1\|\|A_2\| \sum_{m=-\infty}^{\infty} \left(\sum_{k=-\infty}^{\infty} J_m(\beta_3) J_k(\beta_2) J_k(\beta_1) cos\left((\omega_2 - \omega_1)kt + m\left(\omega_3 t\right) + \phi_2(x) - \phi_1(x)\right)\right) \tag{66}$$

m-th index of the infinite sum represents the different carriers generated. While the k-th index represents the side-band harmonics associated with the depth modulation β_1 and β_2.

6.5 Calibration of the wavelength based on an HCN cell reference

To determine whether the phase generated carrier technique (PGC) constitutes a useful technique to disambiguate mapping from the optical domain to the optical domain we can consider its application to recover an absorption line of an HCN gas cell. Considering that those absorption lines can be used as the absolute reference in many applications we can try to recover those lines to demonstrate that the multiheterodyne process that happens on this kind of system is not ambiguous. That is, we have an injective relationship (one to one rule) between the optical comb structure and the electrical mapping comb.

The absorption profile that we want to study is shown in Fig. 71. The goal is to place the

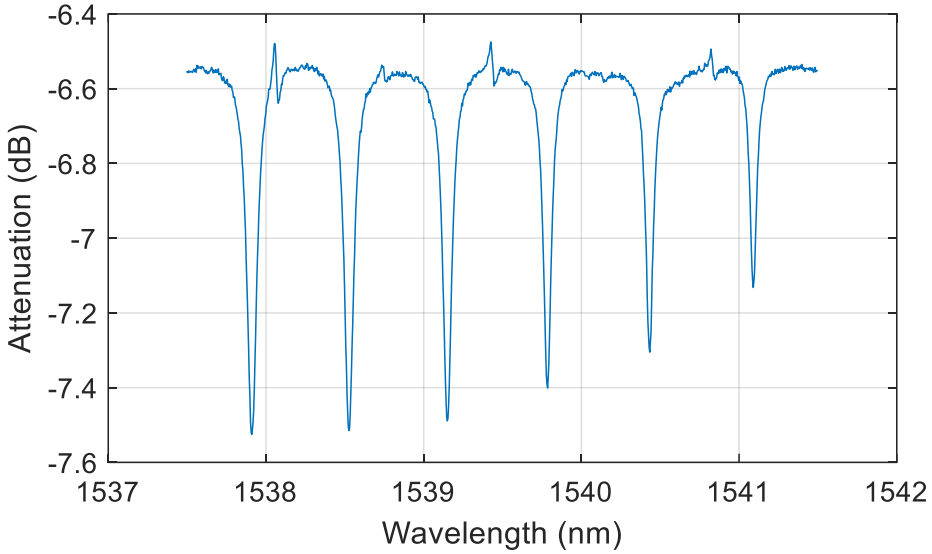

Fig. 71 Absorption profile of an HCN cell used as the absolute reference.

wavelength of the laser in different parts of it and try to recover the shape of the under-study wavelength interval. The ability to recover nonsymmetrical shapes from the electrical mix of the comb ensures an injective mix of the optical domain to the electrical domain.

For our proposed experiment we use a small a big signal approach in the first measurement and a small signal approach in the second one.

As we will see, the small-signal approach can deliver much more information on the differential slope of the under-study absorption profile and at the same time provides information on the optical attenuation.

6.5.1 Set-up of the system

The proposed system is shown in Fig. 72 a continuous laser is injected into a dual-drive Mach-Zehnder modulator to obtain two optical frequency combs in the 'a' input of the optical switcher. The signal, therefore, has one particular path for each of the states of the optical switch. For the idle state, input a is directed to output c and the PD will have the information of the calibration trace. That is without the influence of the absorption of the HCN cell therefore this trace constitutes the power reference that is compared with the measurement trace.

For the cross-state of the optical switcher, we will have the same dual-comb once it has passed through the HCN cell. Accordingly, the amplitude of each optical tone is modified by the absorption profile of the HCN cell.

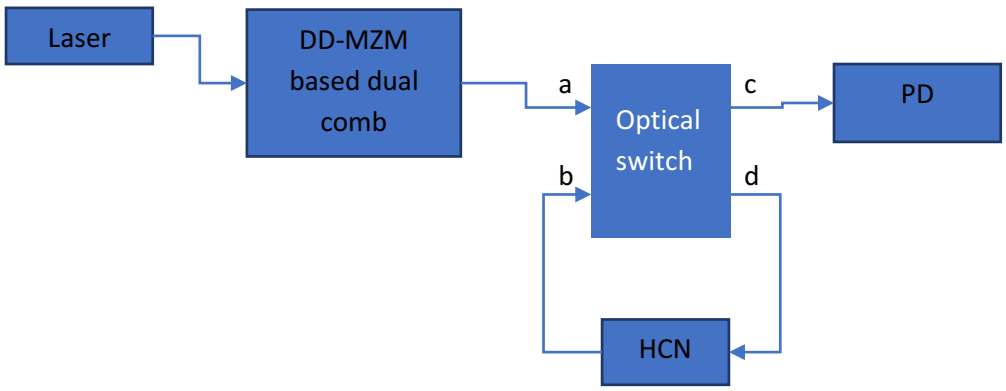

Fig. 72 Set up of the implementation of the Dual optical frequency comb based on dd-MZM applied to HCN gas absolute absorption line readout.

The result is a difference in amplitude with respect to the calibration trace obtained on the parallel state of the optical switch.

6.5.2 Asymmetry study

Even though, we are not using the small-signal approach we can see how the electrical response is changing its shape if the electrical domain absorption is varying. As seen in Fig. 73, if the central wavelength of the laser is placed in a different part of the absorption line, we can see that the power distribution in the optical domain tilts either to the low frequencies or to the high frequencies depending on the position of the laser wavelength with respect to the center of the absorption line. In Fig. 73 a) we can see a right tilt when the laser is placed on the lower wavelengths of the absorption line (Fig. 73 b)). In the case that the wavelength of the laser is placed on the center of the absorption line of the HCN (Fig. 73 c)) we can see how the electrical amplitudes of the comb remain symmetrical (Fig. 73 d)). Finally, in the case of the left side tilt of the electrical spectrum (Fig. 73 e)), the optical wavelength of the laser is placed on the right side of the absorption line of the HCN (Fig. 73 f)).

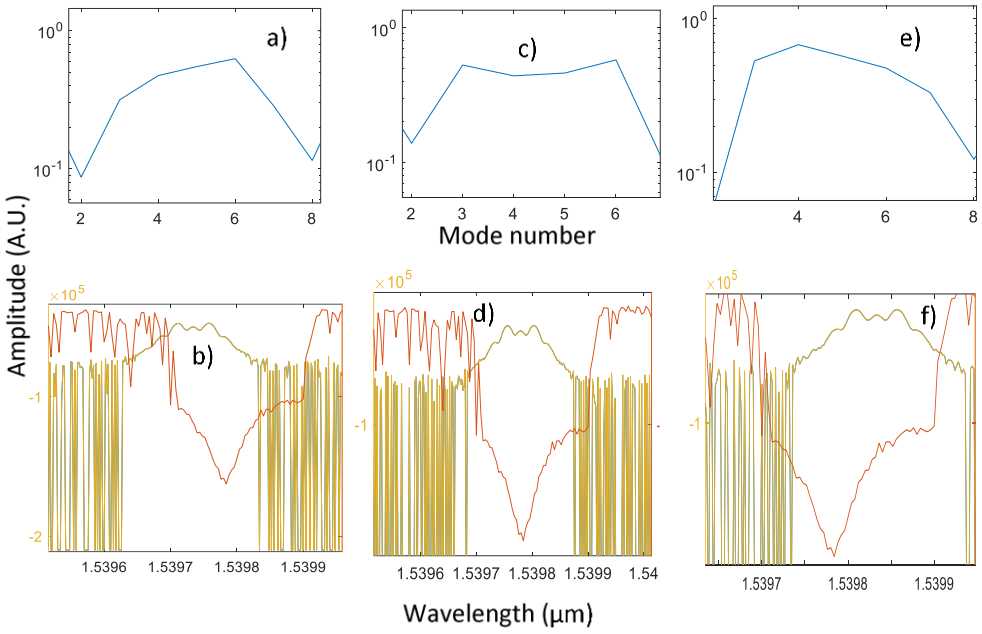

Fig. 73 Asymmetry test for absolute reference in HCN cell. a) Left asymmetry in electrical domain b) centered in electrical domain c) right asymmetry in electrical domain d) Left asymmetry in optical domain b) centered in optical domain c) right asymmetry in the optical domain. Red line: absorption profile, yellow line: comb signal, blue line: normalized electrical spectrum.

6.5.3 Small signal approach

For the small-signal approach we assume two hypotheses:

- The slope of the absorption interval that we are studying is the same on all the lines of the comb
- The frequency of the phase generated carrier is very small with respect to the optical one

Those two hypotheses allow us to obtain an inverse transformation from the electrical to the optical domain. In Fig. 74 a) we can observe the overall setup that was implemented. We used a single mode laser that was modulated in current by a PGC signal. The resulting light beam is injected into a dual drive MZM to obtain the optical sidebands for both combs and finally we read the sample by bypassing it with an optical switch. Finally, we connect a photodetector to the output. In Fig. 74 b) we observe the electrical domain of the generated comb that is constituted by optical modes. In Fig. 74 c) we can observe the structure of a dual drive Mach-Zehnder modulator and in Fig. 74 d) we can observe the reconstruction of the absorption line with a total of 25 points of the spectra. The procedure consists of placing the laser at five equally spaced locations of the spectrum of interest and register the 5 amplitudes of the generated comb at each optical wavelength.

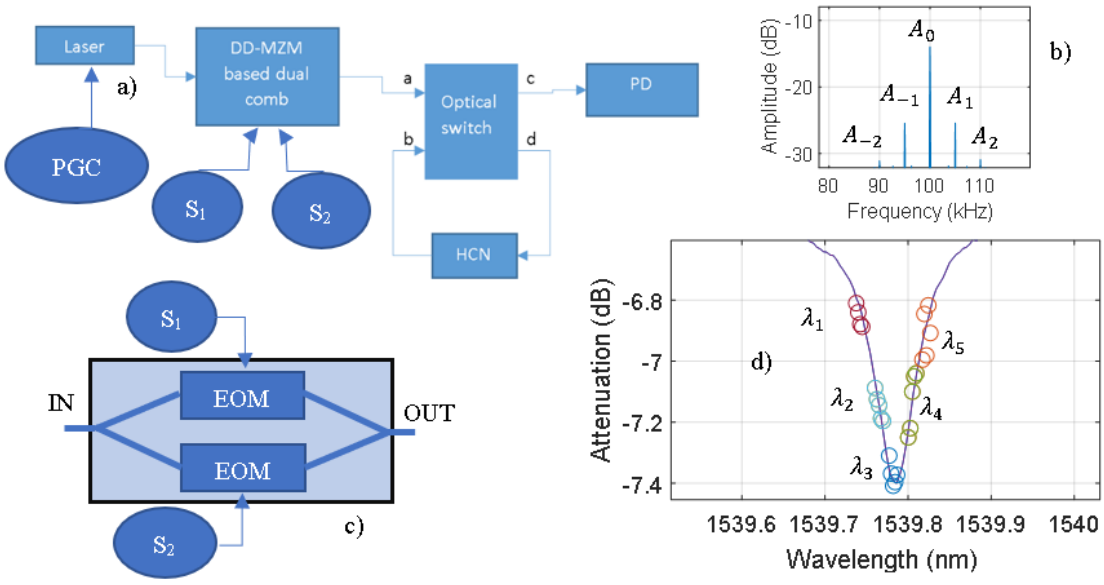

Fig. 74 Small signal implementation detail of the system, a) optical setup, b) photo-detected output of the system, c) inside view of the dual-drive Mach-Zehnder modulator, d) the recovering process of the profile of an absorption line of HCN.

6.6 Conclusions

This chapter relies on the hypothesis that it is possible to generate a multiheterodyne and multimode source that maps optical information with just one electrooptical dual-drive Mach-Zehnder modulator. With this approach, we can operate at either 1310 nm or 1550 nm or both, as we have no restriction from the acousto-optic devices.

The chapter also introduces the spectroscopy technique used to recover the absorption profile of an HCN gas cell as a case study to characterize the multimode multiheterodyne source. The working principle is focused on a particular small-signal simplification to obtain the readout of the absorption profile.

There are several advantages and drawbacks of using all electro-optical implementations of the dual-comb. The main advantages are:

- Wavelength: the operation wavelength can be chosen in a band wider than for the acousto-optic frequency shifted implementation. This is due to the acousto-optic modulator is designed to work at a certain wavelength (for instance, 1310 nm or 1550 nm). Whereas the all-electro-optical modulation allows a wider range of wavelengths. It is noteworthy to mention that the insertion loss of the device is dependent on the wavelength in our case 9.15 dB at 1310 nm and 8.83 dB at 1550 nm.
- Compactness: the compactness achieved is very advantageous, particularly for the operation out of the laboratory.
- Change in phase drift: as the design is done in an integrated device, the optical paths are operating under lower gradients of temperatures. In addition, the effect of the strain on the optical path change is negligible. This ensures that the phase changes and consequently the fluctuations are lower.
- Frequency mapping eligibility: the all-electro-optical frequency comb allows to select the carrier in the readout electrical spectra and therefore it can be fitted to the user needs of bandwidth.
- The phase noise of the source (the effect of any change of wavelength) is lower than in a discrete implementation case because the path imbalance of the in-chip device is lower than the one achievable in a discrete implementation.

On the other hand, the main disadvantages are:

- The broadness of the dual-comb is limited to the maximum signal power that can be applied to the modulator. In the case of the single dual drive modulator, it is lower than for the case of two independent modulators.
- No direct optical access is available to each of the arms of the device due to the fabrication architecture.

The overall results lead to a versatile configuration useful to sample a few points of the optical spectra. As it will be presented in chapter 8, the narrow band detection with this multimode multiheterodyne source becomes practical for the readout of the FBG sensors with a dispersive interferometer.

Chapter 7: Acousto-optic self-heterodyne readout of grating sensors

“If you can trust yourself when all men doubt you, yours is the Earth and everything that’s in it"- Rudyard Kipling

7.1 Introduction

This chapter proposes the use of an acousto-optic self-heterodyne comb to interrogate random fiber grating sensors. These sensors are used to detect surface acoustic waves of frequencies above 20 kHz and up to 1 MHz.

Random fiber gratings are devices that can be used to detect strain or temperature. They have a sensitivity to strain of 1.2 pm / με and a sensitivity to temperature of 10 pm / K. However, unlike the uniform FBG sensors, the random fiber grating sensor have a degenerated back reflection response with a random attenuation with respect to the wavelength. This behavior extends over 200 nm or 300 nm of optical span, making the aligning process of the reading laser unnecessary in comparison with FBG devices.

Despite the random behavior, the whole spectrum shifts when strain or temperature change is applied to the sensor. The sensor can be interrogated with a broadband source and with an optical spectrum analyzer by calculating the correlation between a reference trace and a measurement trace.

However, the time response is limited in this case. The interrogating system that we propose is based on an acousto-optic device that is fed-backed to generate an optical comb. This multiheterodyne source is inserted into the random fiber grating sensor to obtain its changes with dynamic strain.

All these results are presented in the article: Poiana, D.A.; Garcia-Souto, J.A.; Bao, X. “Acousto-Optic Comb Interrogation System for Random Fiber Grating Sensors with Sub-nm Resolution”. Sensors, 2021, 21, 3967. https://doi.org/10.3390/s21123967

7.2 Self-heterodyne setup

The self-heterodyne comb is a kind of multi-heterodyne source that maps the image of the spectra to the RF domain. The multiheterodyne process happens with respect to one optical mode instead of a comb as it is the case of the dual comb [40], [41], [50].

This multiheterodyne process is achieved with more simplicity compared to the dual-comb architecture as in this case fewer components are needed compared to the acousto-optic dual-comb arrangement. In the case of the acousto-optic self-heterodyne comb, the achievable SNR is higher compared to the electro-optic implementation and at the same time, more power-efficient in terms of the consumption of the modulating process. The only drawback is that the mapping frequency and comb-line spacing is not controllable, but a fixed value determined by the frequency operation of the acousto-optic modulator. The main mixing process is shown in Fig. 75 a), On the left part of Fig. 75 a) we can observe the multiheterodyne process between the acousto-optically generated comb and the optical laser seed that serves us as a phase and amplitude reference. This mix results on a photo-detected signal that contains the information of the optical domain.

Fig. 75 b) shows the random fiber grating back-reflection profile that modulates the amplitude of the optical comb. Finally, Fig. 75 c) shows the frequency domain of the photo-detected signal.

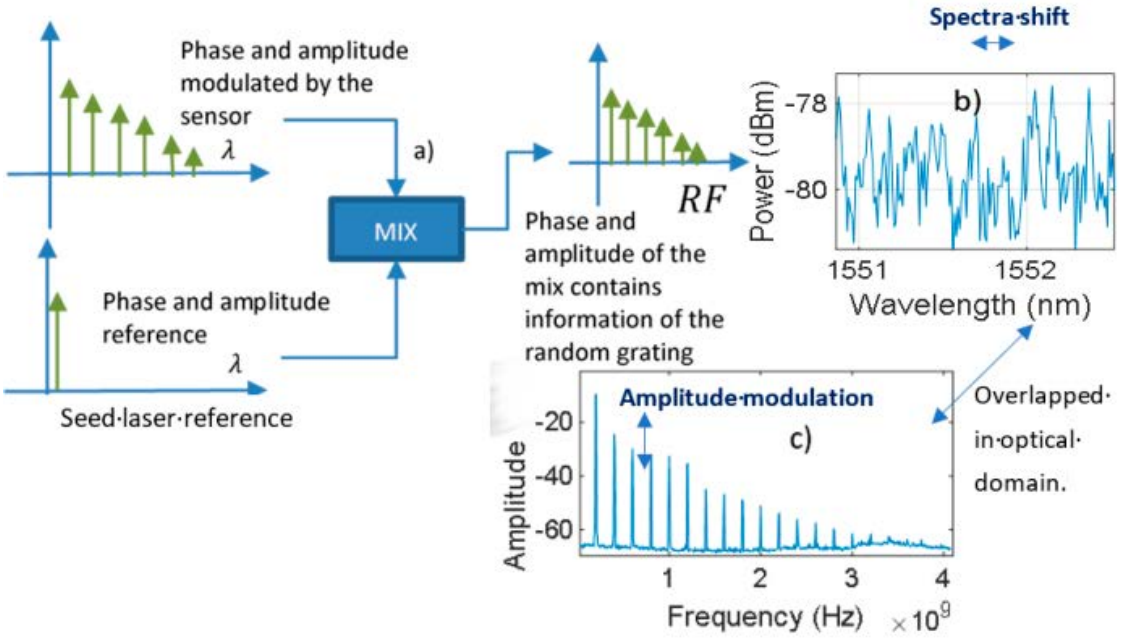

Fig. 75 Self heterodyne working principle, a) optical mixing process, b) random fiber grating spectrum, c) photo-detected RF output.

The implementation of the system can be seen in Fig. 76. A high-quality laser is used to feed the system. The light beam is split into two optical paths by means of the beam-splitter C1. One of the light beams feeds the acousto-optic feedback and the other one feeds the reference arm. The acousto-optic feedback is composed by two beam splitters C1' and C2' that allow to redirect the output light again towards the input of the acousto-optic modulator by means of an EDFA. The resulting acousto-optic comb is directed towards the random fiber grating by means of a circulator and finally, the back-reflection obtained on the third port is directed to the C2 beam splitter.

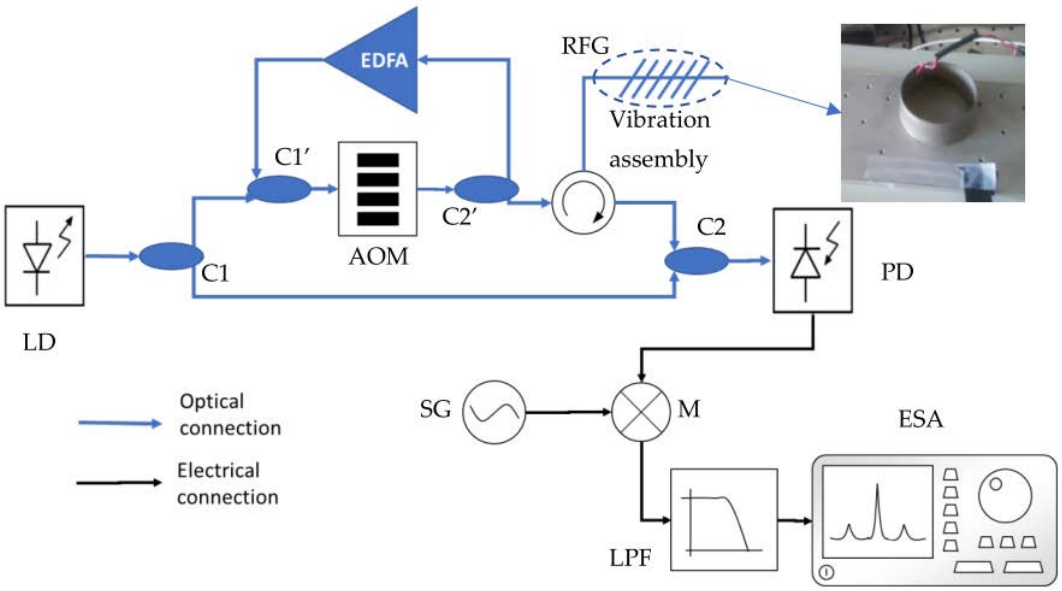

Fig. 76 Selfheterodyne implementation together with view of the mechanical assembly.

The photo-detected signal is mixed with a signal generator SG and low pass filtered to obtain the amplitude of the desired optical line of the comb. The optical line of the laser is placed at 1551.8 nm, and we use a 1.6 pm spacing between the optical lines. The resulting acousto-optic comb has a SNR of 60 dBc over a bandwidth of 4 GHz.

A small signal regime enables linear operation and therefore a linear amplitude modulation over the amplitudes of the optical lines of the comb. And therefore, we should use synchronous demodulation to extract the amplitude information of the desired line of the comb. In Fig. 77 we can observe the demodulation process of the photodetected signal. We mix the RF comb with a reference whose frequency is equal to the frequency we want to extract from the electrical domain and finally we low pas filter the signal. The result is a frequency linearized signal that has the parameters of the input mechanical vibration signal.

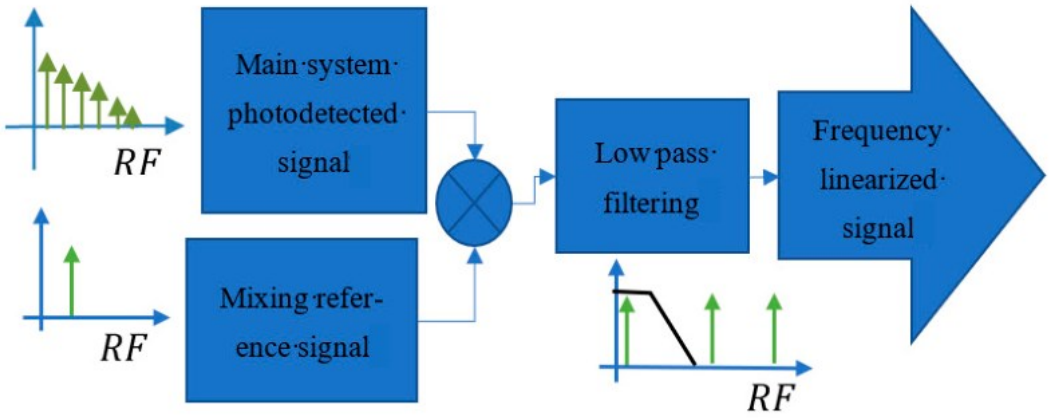

Fig. 77 Demodulation process of the photodetected signal.

7.3 Calibration of the system

One of the most important parts of the system is the calibrating interferometer. This secondary, system allows the absolute calibration of the displacement in terms of amplitude with the prerequisite assumption of having a pure frequency excitation on the PZT. In Fig. 78 we can observe the whole system and particularly the calibrating interferometer that is circled with a dashed line.

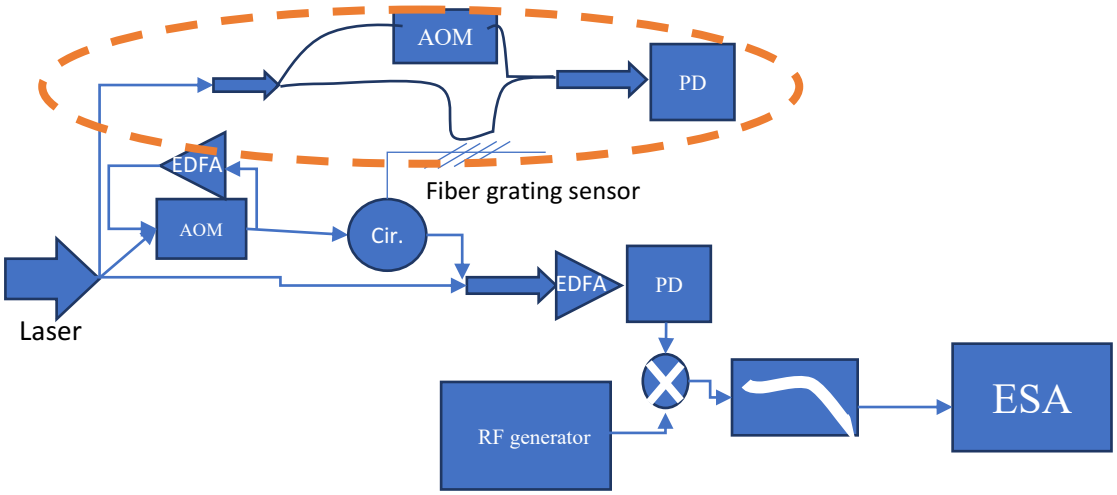

Fig. 78 Complete mounted setup.

The interferometer is used to calibrate the system. The same stimuli are applied to the active part of the interferometer and the fiber grating sensor for determining what is the value of strain applied.

The algorithm for demodulating is based on the one shown in [51]. The steps are the following:

1. Perform the FFT over the photo-detecting signal
2. Calculate the ratio between the carrier and the sidebands generated around the carrier (see Fig. 79).
3. Calculate the modulation depth with the Bessel function relationship (67).

$$10log\ (\ J_n(\phi_m)/J_{n+1}(\phi_m)\ )\ -\ \alpha = 0 \tag{67}$$

where α is the measured relationship between n-th and n +1 electrical domain tone in decibel units (dB). $J_n(\phi_m)$ represents the Bessel function of the first kind and order n. z represents the depth modulation.

4. From modulation depth calculate the equivalent phase-amplitude ϕ_m as (68)

$$\phi_m = \frac{2\pi n K_f}{\lambda_0}\ z \tag{68}$$

were n is the effective refractive index of the fiber, λ_0 is the wavelength of the laser z is the modulation depth. K_f is the strain-optic coefficient.

5. Finally, express the phase as a wavelength related unit ε_m as (69)

$$\varepsilon_m = \frac{\frac{\phi_m}{2\pi n K_f}\lambda_0}{L_{eff}} \tag{69}$$

were L_{eff} is the length over which the strain is applied. The resolution of the applied strain (ε_m) is dependent on the signal-to-noise ratio (SNR) of the photo-detected signal and therefore the better the quality of the laser the lower the noise floor. On the other hand, there is a high dependence of the SNR on the imbalance of the interferometer therefore the arms should be adjusted carefully.

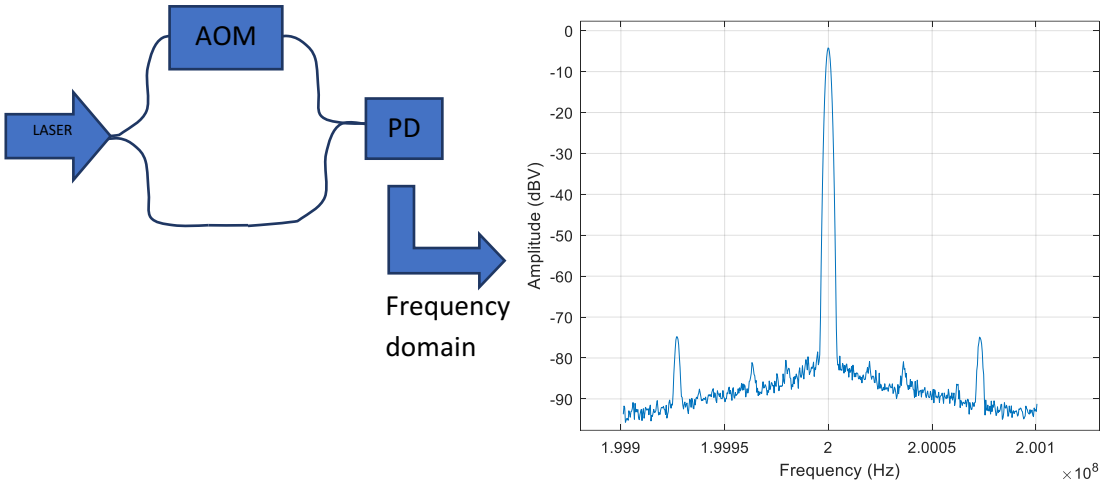

Fig. 79 Heterodyne interferogram in frequency domain for the heterodyne interferometer.

For solving (67) for z we can choose to do it numerically. The reason is that there is no inverse analytical function for $J_n(z)$ function as it is a non-injective function. The plots for different intervals of z are shown in Fig. 80. Therefore, with just the attenuation between $J_n(z)$ and $J_{n+1}(z)$ calculated in the interferogram frequency domain we can obtain a known value of z or mechanical displacement. That value, then, can be used during the other steps of the algorithm. For 100 dB of attenuation, we have less than microradians and therefore achieve less than a part per billion of the laser wavelength value, in this case, less than one part per billion 1550 nm. Here it is clear that the higher the signal-to-noise ratio the better the resolution of the algorithm. The signal-to-noise ratio is very dependent on the bandwidth FFT window as well as the step of the FFT algorithm. However, there is a very important physical dependence on the phase noise of the laser and the path imbalance of the interferometer. The higher the path imbalance the higher the noise floor for the same bandwidth.

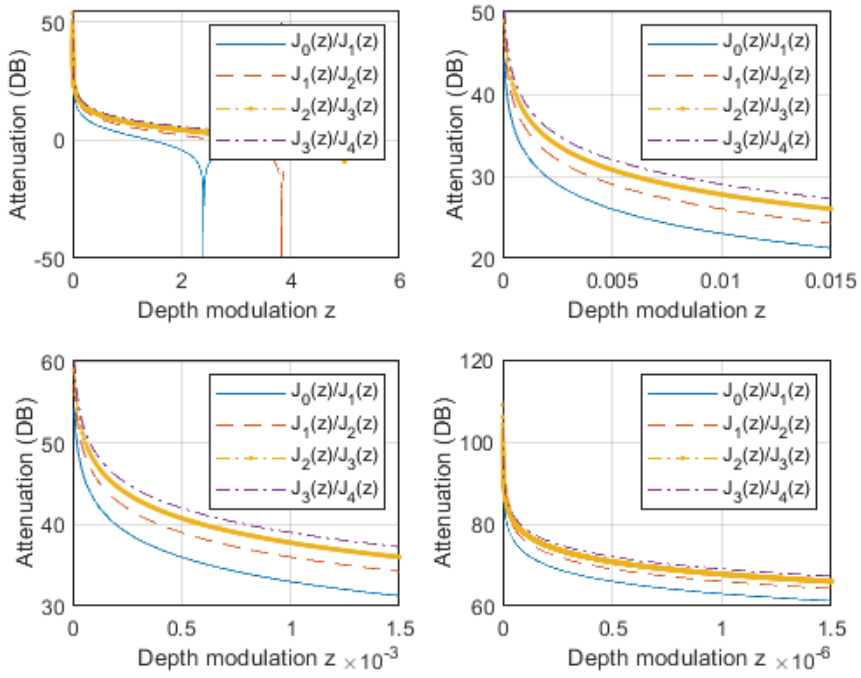

Fig. 80. Calibration curve for the measurement algorithm for different depth modulation intervals.

The result of applying a vibration over the calibrating system results in a sideband modulation in the heterodyne system. In the case of a heterodyne interferometer, the sidebands are placed around the acousto-optic modulation frequency and therefore, a pure sinusoidal wave will generate several spikes spaced each an amount equal to the frequency of excitation. Their amplitudes and the number of lines will depend, as mentioned before on the amplitude of the vibration stimulus.

One can register the amplitude of the applied stimulus vibration signal and refer it to the amplitude distribution of the generated sidebands. In Fig. 81 we can see how the variation of the interfering signal depends on the amplitude of the mechanical vibration.

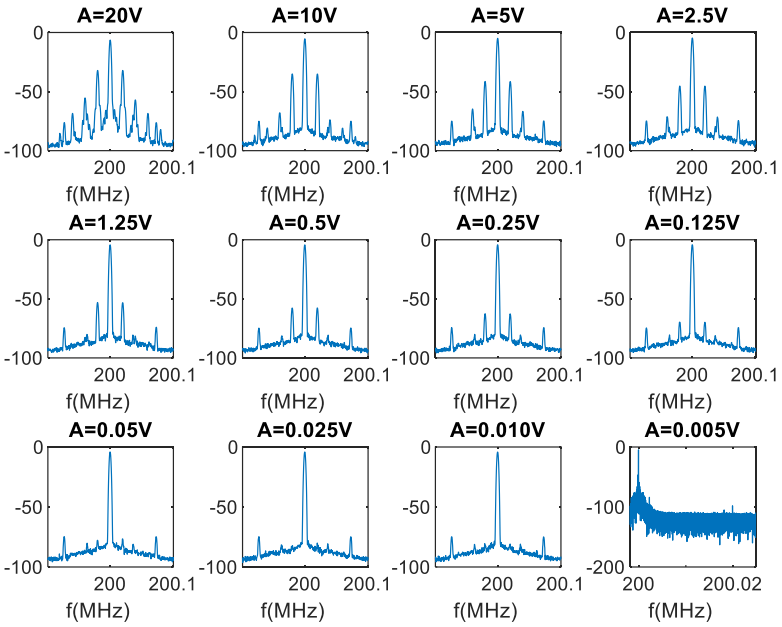

Fig. 81 Interferogram response over a 200 kHz bandwidth around the electrical carrier to a 20 kHz signal at different amplitudes.

Analyzing the ratio between the first and second harmonics one can reach an equivalent displacement for each depth modulation in meter units.

7.4 Experimental results and discussion

Once the applied strain is calibrated with the interferometer, we can apply it to our fiber grating interrogating system. For understanding the working principle, we can consider two electric fields. We consider $E_{comb}(t,z)$ as the electric field that is traveling along the arm of the feed-backed acousto-optic arm and $E_1(t,z)$ as the electric field of the other arm with no acousto-optic modulation. $E_{comb}(t,z)$ can be written as (70). And therefore, it is a set of N optical tones separated in the optical domain an amount that is equal to the acousto-optic modulating frequency [42].

$$E_{comb}(t,z) = E_0 \sum_{a=1}^{N} A_a e^{j\left((\omega_1 + a\Delta\omega_{AOM})\, t - \frac{2\pi n}{\lambda + a\Delta\lambda}(z + (a-1)\Delta L) + \phi_a\right)} \tag{70}$$

where E_0 is the electrical field amplitude at the input of the optical acousto-optic loop. A_a is an attenuation that is dependent on the optical loop iteration and it is a function whose value depends

on the insertion loses of the acousto-optic modulator as well as the couplers and connectors, ω_1 is the pulsation of the light carrier, $\Delta\omega_{AOM}$ is the acousto-optic modulator driving pulsation, n is the effective refractive index, λ is the optical wavelength of the laser, $\Delta\lambda$ Is the wavelength shift associated to the acousto-optic output optical order, ΔL is the length of the optical loop that the light beam has to travel each iteration, ϕ_a is the modulation of the optical phase of each a-th phasor.

For the reference tone that is traveling through the second arm, we assume it behaves as (71)

$$E_1(t,z) = E_0 e^{j\,(\omega_1\, t - k_1 z + \phi_1)} \tag{71}$$

where k_1 is the wavenumber of the laser seed and ϕ_1 is the initial phase. The photo detected intensity of the mix of (70) and (71) is of the form of (72)

$$I(z,t) \propto \sum_{a=1}^{N} 2E_0^2\, A_a cos\,(a\Delta\omega_{AOM} t + \frac{2\pi n}{\lambda + a\Delta\lambda}\,(z_c + (a-1)\Delta L) - k_1 z_1 + \phi_a - \phi_1) \tag{72}$$

As we can see we obtain a multi-heterodyne mix, whose amplitude is proportional to the optical amplitude and whose instantaneous phase is proportional to the instantaneous phase difference between the reference tone $E_1(t,z)$ and the a-th tone of the $E_{comb}(t,z)$ function.

The fiber sensor will modulate the amplitude and phase of (72) A_a and $\phi = \phi_a - \phi_1$ change. If we assume small signal approach for very small amplitude vibrations the change in modulations is linear therefore there is transduction between the vibration to the optical domain and then to the electrical domain. We can write those variations as (73) for the amplitude variations and (74) for the phase variations.

$$\delta A_a = K A_{vibration} cos\,(\omega_{vibration} t) \tag{73}$$

where K is a constant and $A_{vibration} cos\,(\omega_{vibration} t)$ is the mechanical vibrating signal.

$$\delta\phi = \phi_m\, cos(\omega_{vibration} t) \tag{74}$$

where ϕ_m is the depth modulation of the mechanical signal.

For the demodulation, we choose to mix the interferogram analogically with a pure tone of variable frequency $b\omega_{AOM}$ and amplitude A as (75).

$$f(t) = A\,cos\,(b\omega_{AOM}t) \tag{75}$$

The result of the mix between (72) and (75) is of the form of (76)

$$\begin{aligned}\Gamma(A_{vibration}, t) &= \sum_{a=1}^{N} 2E_0^2\,A_a\,A\,cos\left(\frac{2\pi n}{\lambda + a\Delta\lambda}\,(z_c + (a-1)\Delta L) - k_1 z_1 + \phi_a\right. \\ &\left. - \phi_1 + (a-b)\Delta\omega_{AOM}t\right) \\ &+ \sum_{a=1}^{N} 2E_0^2\,A_a A\;cos\left(\frac{2\pi n}{\lambda + a\Delta\lambda}\,(z_c + (a-1)\Delta L) - k_1 z_1 + \phi_a\right. \\ &\left. - \phi_1 + (a+b)\Delta\omega_{AOM}t\right)\end{aligned} \tag{76}$$

For $a = b$ and low pass filtering with a high attenuation on $2\Delta\omega_{AOM}$ we obtain (77).

$$\begin{aligned}\Gamma(A_{vibration}, t) &= AKA_{vibration}cos\,(\omega_{vibration}t)\;cos\left(\frac{2\pi n}{\lambda + a\Delta\lambda}\,(z_c + (a\right. \\ &\left. - 1)\Delta L) - k_1 z_1 + \phi_a - \phi_1\right) \\ &\approx A\,KA_{vibration}cos\,(\omega_{vibration}t)\;cos(\phi_m cos\,(\omega_{vibration}t))\end{aligned} \tag{77}$$

Experimentally, it can be demonstrated that the dispersion term of phase modulation can be negligible, and phase-modulated is very small compared with the noise floor. This is seen from the sideband generated by the term $\cos(\phi_m \cos(\omega_{vibration}t))$ if the sidebands are over the noise floor, we can conclude that the dispersion influences the output response. However, in our case we do not have any, therefore it means that $\phi_m \to 0$. Analytically, it can be demonstrated by applying limits to (77). Thus, (77) simplifies to (78)

$$\Gamma(A_{vibration}, t) \propto A\,KA_{vibration}\,cos(\omega_{vibration}t) \tag{78}$$

(78) demonstrates that the output signal is proportional to the mechanical vibration signal $A_{vibration}\cos(\omega_{vibration}t)$.

The vibration is applied with a PZT similar to the one shown in Fig. 82 a). A set of different cases were acquired at 300 kHz, 400 kHz, 500 kHz, 600 kHz, 700 kHz, 800 kHz, 900 kHz and 1 MHz.

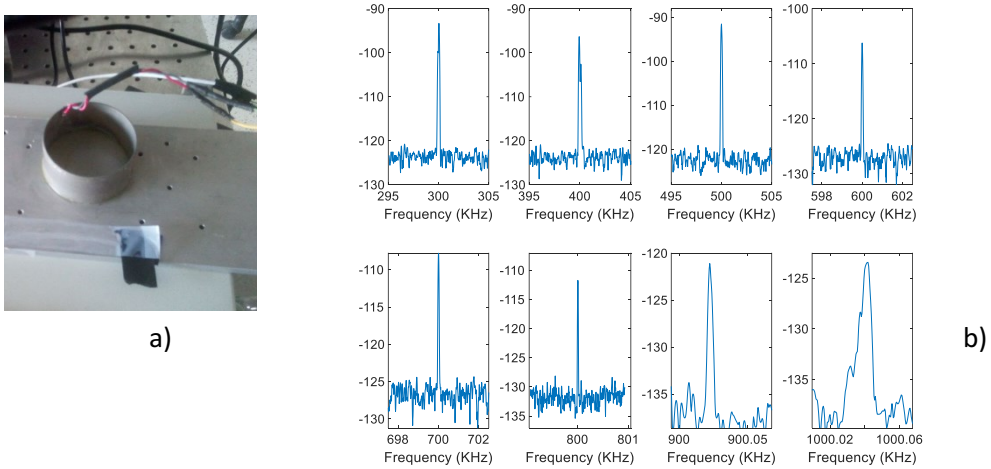

Fig. 82 Implementation of the readout system with random fiber grating a as a sensing device. a) piezoelectric actuator placed at 5 cm distance of the fiber, b) results of the demodulation signal at different frequencies.

Those results are shown in Fig. 82 b).

For measuring the minimum resolution of the implementations, we use the arbitrary criteria of having a minimum of 3 dB signal-to-noise ratio. This means that we diminish the applied amplitude to a point in which 3 dB signal with respect to the noise floor is detected. For the interferometer implementations and afterward we register the minimum amplitude for each of the implemented systems.

The heterodyne calibration system is the best performer. This is due to the high concentration of the power in the carrier used for the calibrating algorithm. It is noticeable that the homodyne calibration has a lower noise floor than the heterodyne, however, the power of the carrier is noticeably smaller and therefore the minimum detectable amplitude is worse than in the heterodyne case.

For determining the detection bandwidth, we can evaluate the signal to noise ratio with respect to frequency. Therefore, for a parametric sweep of the frequency, the detectability of the system falls very fast over 1 MHz. In the case of the calibrating systems, the detectability falls dramatically over 200 kHz and therefore absolute calibration cannot be performed after that point. Thus, our system outperforms the calibrating systems in frequency response.

The signal-to-noise ratio can be seen in terms of frequency in Fig. 83. The uniform fiber Bragg grating slightly outperforms the random fiber grating at high frequencies.

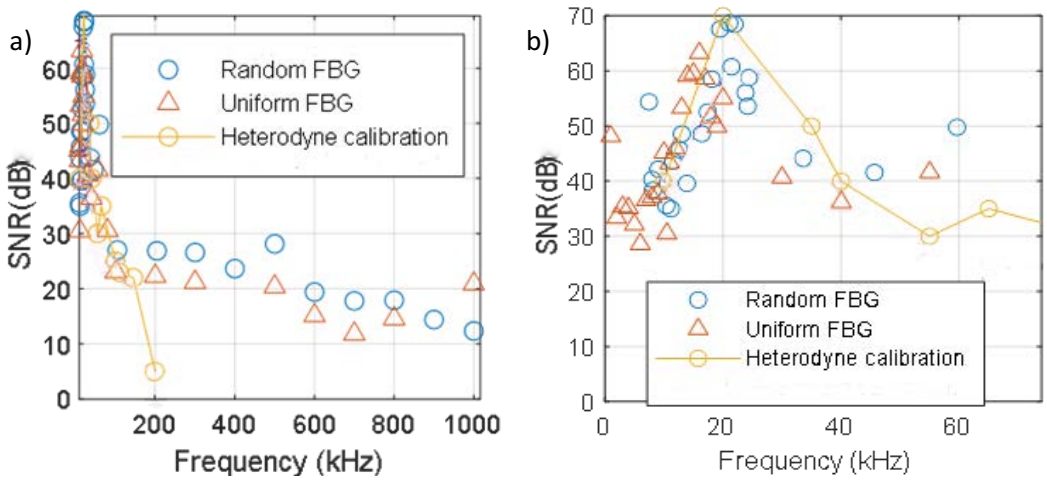

Fig. 83 Signal to noise ratio measured for different frequencies with Random fiber grating and uniform fiber Bragg grating sensors a) whole spectra, b) detail of the resonance peak of the system.

7.5 Conclusions

In this chapter, a system for interrogating random fiber grating sensors has been presented. The design uses an acousto-optic self-heterodyne comb that is injected into the under-test sensor. The sensor modulates the amplitude of the comb lines, and this magnitude is read in the electrical spectrum domain.

The proposed system can detect small-amplitude dynamic strain vibrations and ultrasounds up to 1 MHz which overperforms the frequency response of the calibration system based on a fiber optic heterodyne interferometer. The measurement resolution within the calibration interferometer bandwidth (200kHz), is two times better than the resolution achieved with the grating sensing system.

A very important advantage of the random fiber grating compared with a uniform fiber Bragg grating is that there is no need to fit the laser wavelength with any particular point on the spectra. That is because the random spectra extend over a broad range of wavelengths of about 200 nm-300 nm.

Chapter 7: Acousto-optic self-heterodyne readout of grating sensors

Chapter 8: Compact interrogation of grating sensors based on multiheterodyne dispersion interferometry for dynamic strain measurements

“If you can keep your head when all about you are losing theirs, yours is the Earth and everything that’s in it"- Rudyard Kipling.

8.1 Introduction

An alternative to measuring the reflection spectrum of an FBG is to use the dispersion profile (Section 3.5). In this chapter, we present a dispersion-based approach applied to fiber Bragg grating sensors in which the dual comb is compacted into a single dual-drive-unit optical modulator (Chapter 6) and the fiber sensor is part of a dispersion interferometer.

This reading technique allows to increase the overall sensitivity of the system compared to the case of the reflected amplitude reading as in Chapter 5.

A common drawback of dual-comb spectroscopy is the need for a broad-band amplitude-resolved absorption or reflection measurement, which increases the complexity of the dual-comb and requires precise calibration of the optical detection.

The proposed system uses a narrow-band dual comb that is achievable by using a single DD-MZM and it is applied to the measurement of surface vibrations and ultrasounds with weak FBG sensors.

The main contents of this chapter are part of the journal article published in Sensors: Dragos A. Poiana, Julio E. Posada-Román and José A. García-Souto, “Compact Interrogation System of Fiber Bragg Grating Sensors based on Multiheterodyne Dispersion Interferometry for Dynamic Strain Measurements”. Sensors, 2022, 22, 3561. https://doi.org/10.3390/s22093561

8.2 Set-up of the experiment

The experiment setup system is seen in Fig. 84. The first one is the one that is measuring the strain and that we want to characterize in terms of performance and the second one is a heterodyne interferometer that is intended for calibrating the measurements and for obtaining a reference of the order of magnitude that the main system is measuring [51], [52]. The main system uses a continuous wave laser TSL210 at 1310 nm that operates at 12 dBm of output optical power. It is injected into the DOFC dual-drive MZM modulator that generates the multiheterodyne source and afterward, it is injected into the Michaelson interferometer that will read the dispersion information of the uniform FBG sensor [53]–[55]. The resulting dispersion profile is read in PD1 in the frequency domain.

The calibrating interferometer operates as discussed in previous chapters. The absolute magnitude is obtained with sideband generation ratios. The seed laser for the calibrating interferometer is a Qdfb-ld-1550-50 and the chosen setup is a Mach Zehnder interferometer.

The dispersion profile of the FBG sensor can be read in terms of wavelength on the output of the interferometer. The form of this function is pseudo-periodic [2], [3] and has information of the strain applied to the sensor encoded in its amplitude with respect to the wavelength. For uniform, and therefore no gradient strains, applications the spacing between the pseudo periods or fringes is constant in uniform FBGs. However, if constant gradients are applied to the sensors a chirp in the dispersion profile can be seen.

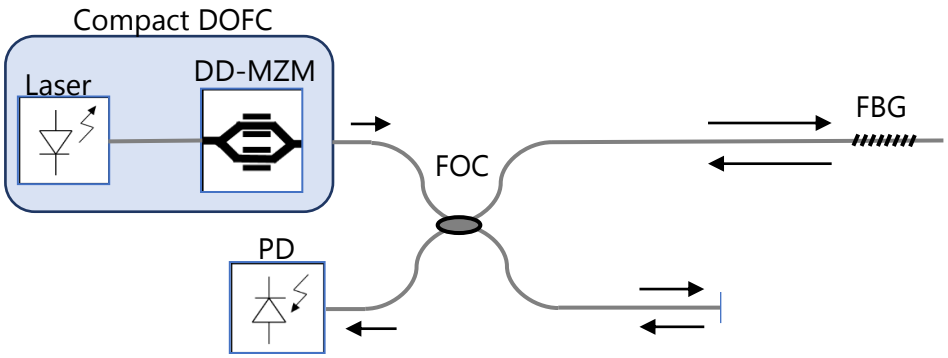

Fig. 84 Set up arrangement of the proposed system.

Those periods can be read in a dynamic regime. By using the DD-MZM we can observe each of the periods independently by aligning the wavelength of the seed laser with the wavelength of the period we want to study.

The main system is composed, as seen in Fig. 84, by the LD1 laser which is a 1310 nm TSL210. That is injected into a DD-MZM that modulates the light to obtain a serrodyne modulated dual comb. The resulting set of tones is injected into a Michaelson interferometer built with a 50:50 beam splitter, a refractive terminal and a low reflectivity uniform FBG sensor (12% reflectivity). The reference arm has a reflective terminal at its end and the measuring arm has the FBG carefully installed to match the length of the reference arm.

On the other hand, the calibrating interferometer is a Mach Zehnder interferometer operating at 1550nm in a heterodyne regime. It has LD2 as a seed laser at 1550 nm and an output signal PD2 that contains the interferogram calibration measurement. It is built with two 50:50 ratio beam splitters and an acousto-optic modulator. The arm difference is less than 1cm to ensure optimal interference quality.

The generation of the dual-comb can be seen in Fig. 85. Four signals drive the DD-MZM. S_{d1} and S_{d2} generate the optical sidebands. PGC is a sinusoidal signal that generates the pseudo carrier, and the "Bias" signal is a DC signal that controls the set point of the device. S_{d1} and S_{d2} are chosen to be 1.0000 GHz and 1.0005 GHz to cover a full semi-period with three tones. The PGC signal is imposed to be at 4 MHz to obtain a mapping frequency of the same value as the amplitude of modulation is less than $2V_\pi$.

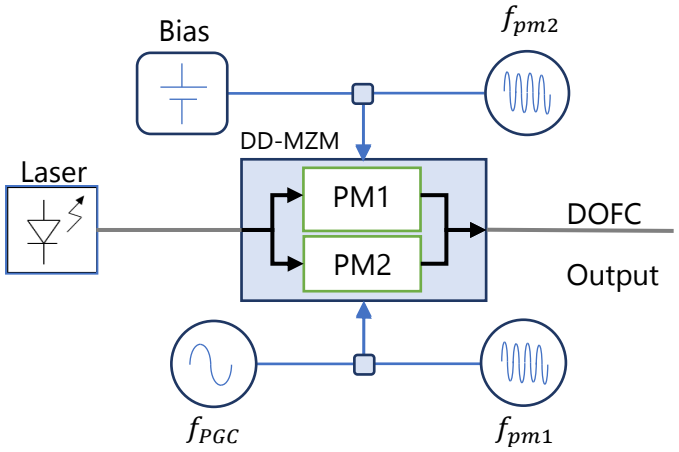

Fig. 85 PGC generation of a dual optical frequency comb with a dual drive MZM.

An example of the optical output of the DOFC is shown in Fig. 86 detected with an OSA (model Yokogawa AQ6370B). In this case, the modulation frequencies applied to the DD-MZM are higher in order to distinguish the different tones with the limited resolution of the OSA (10 pm resolution).

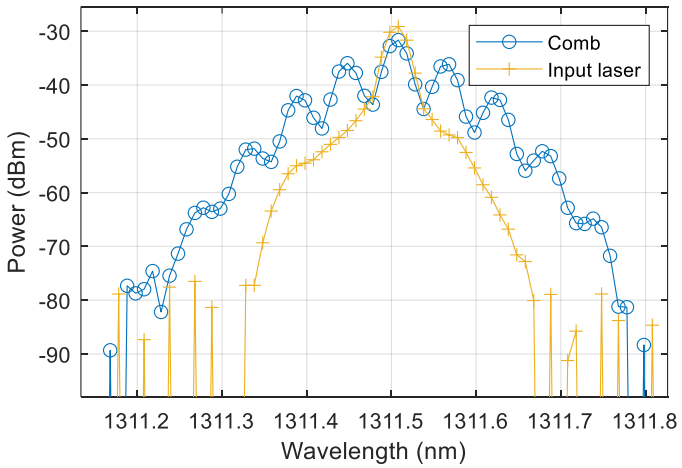

Fig. 86 Generated dual optical frequency comb detected in an OSA

8.2.1 Dispersion reading

For dispersion reading, we can use a Michelson interferometer. We adjust the arms of the interferometer and make the back-reflection response interfere and read the interferogram with an optical spectrum analyzer. Accordingly, if we apply a uniform strain on the FBG sensor we can observe the dispersion behavior of the sensor with strain. The result leads to a response like the one shown in Fig. 87.

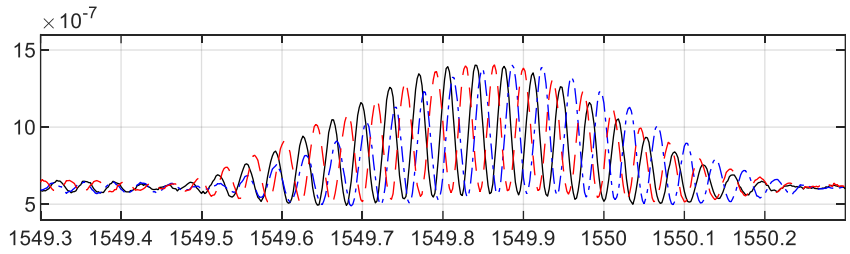

Fig. 87 Dispersion profile of a uniform fiber Bragg grating sensor supporting different values of constant strain.

This dispersion profile is measured for traction (blue) and compression (red). We can see how for uniform strain stimulus; the periods of the dispersion pattern remain constant as each plane of the FBG sensor moves the same quantity.

However, if we apply a gradient over the sensor both in traction and compression, we can expect a function similar to the one shown in Fig. 88. The main difference compared with the previous case is that the period of each fluctuation is variable. Therefore, a gradient of strain in the FBG sensor implies a chirp in the dispersion profile [2], [3].

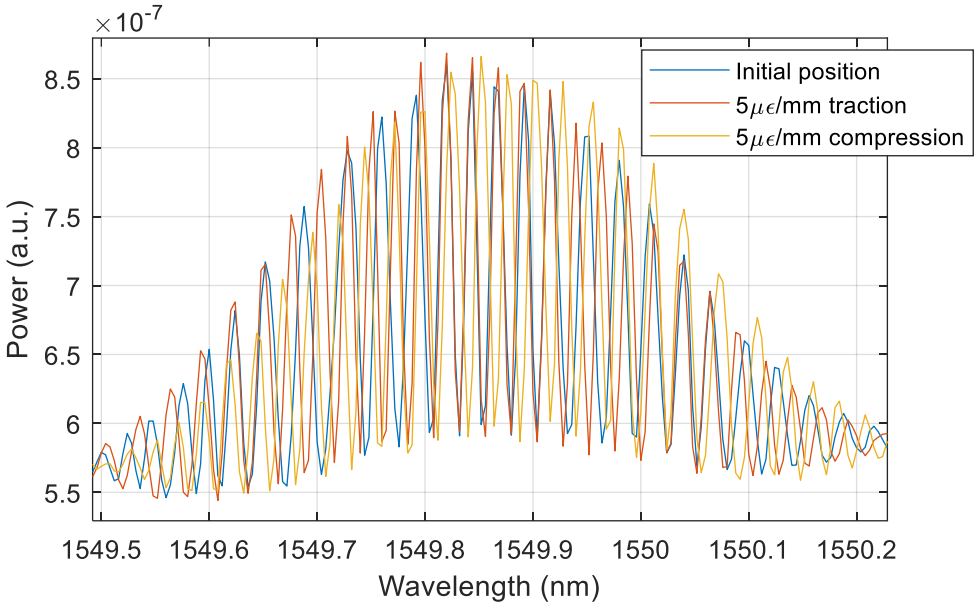

Fig. 88 Dispersion profile of uniform FBG sensors behavior on strain gradient application.

.

8.2.2 Hariharan five-points algorithm

The five-point algorithm of Hariharan allows us to measure a phase difference between two interferograms in the time domain [52], [56], [57]. It allows the measurement of relative phase with just five values of amplitude for a $\frac{\pi}{2}$ delay between each other. The I_i amplitude can be expressed $\forall\, i \in [1, 5]$ in (79) for each value of interferogram amplitude $\frac{\pi}{2}$ spaced.

$$I_1 = A + B + 2\sqrt{AB}cos(\theta - \pi) \tag{79}$$

$$I_2 = A + B + 2\sqrt{AB}cos\left(\theta - \frac{\pi}{2}\right)$$

$$I_3 = A + B + 2\sqrt{AB}cos(\theta)$$

$$I_4 = A + B + 2\sqrt{AB}cos\left(\theta + \frac{\pi}{2}\right)$$

$$I_5 = A + B + 2\sqrt{AB}cos(\theta + \pi)$$

Where A and B are the intensities of each arm of the interferometer and θ is the value of the phase. Therefore, solving for θ we can obtain the value of the phase depending on the values of photo detected intensities I_1, I_2, I_3, I_4 and I_5. We obtain a value of phase as (80).

$$\theta = tan^{-1}\left(\frac{2(I_2 - I_4)}{2I_3 - I_5 - I_1}\right) \tag{80}$$

Although the Hariharan algorithm is supposed to be applied in the time domain for five values separated in time one-fourth of the period, we can apply the mathematical expressions (79) and (80) for the wavelength domain. The result is that we need samples that are spaced one-fourth of the understudied period.

This paradigm enables the use of a dual optical frequency comb for sampling the dispersion of the FBG. The dual comb behaves as a sampling device for specific points over the spectra. By setting the appropriate modulation depth we can generate five lines with the goal of sampling along the wavelength interferogram of the system.

In Fig. 89 a) we can observe the generated comb with five lines, this allows the Hariharan algorithm reading process. In Fig. 89 b) we can see the readout result in the central period of the spectra shown Fig. 88.

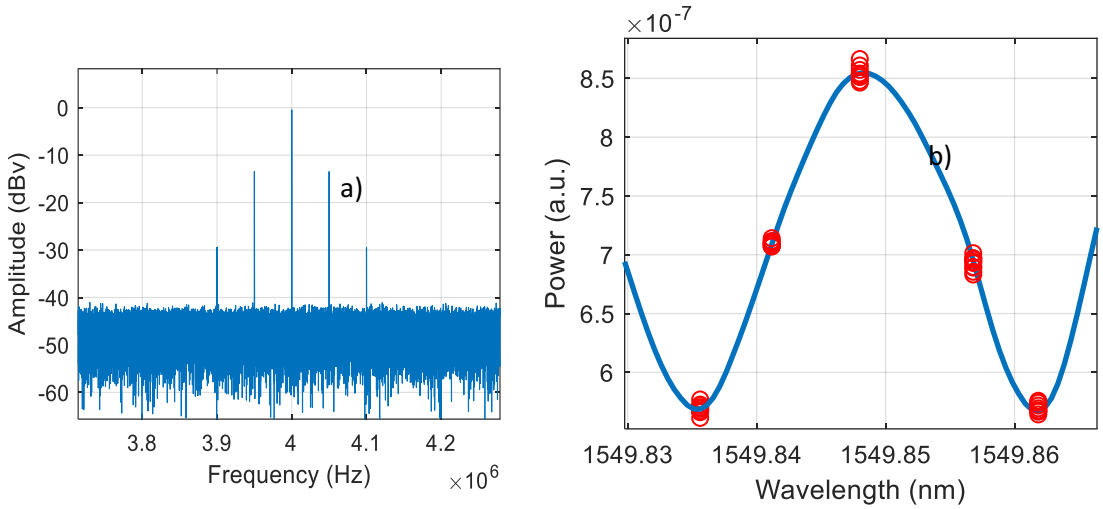

Fig. 89 Readout of dispersion profile via a dual optical frequency comb and the five points algorithm of Hariharan.

This approach allows the readout of FBG in dispersion with all the advantages of a dual optical frequency comb. We obtain a very quick readout that allows high-speed vibration measurements. The Hariharan phase can be translated easily into wavelength displacement and therefore Bragg wavelength can be tracked to obtain a strain or temperature measurement

8.2.3 Reduced Hariharan algorithm

The working principle of the main system is based on a reduced version of the five points Hariharan algorithm. If we place just three comb lines in the period that we want to study and we trim the spacing to impose a 90º spacing between the read points, we can achieve an optimized configuration that has maximum sensitivity. As shown in Fig. 90 a) the middle tone is aligned with the maximum reflectivity of the period and the other two tones I_3 and I_5 are aligned with the -90º and +90º points respectively. Fig. 90 b) shows how if any perturbation is applied to the FBG sensor, the period will shift and accordingly the amplitude of the tones is modulated.

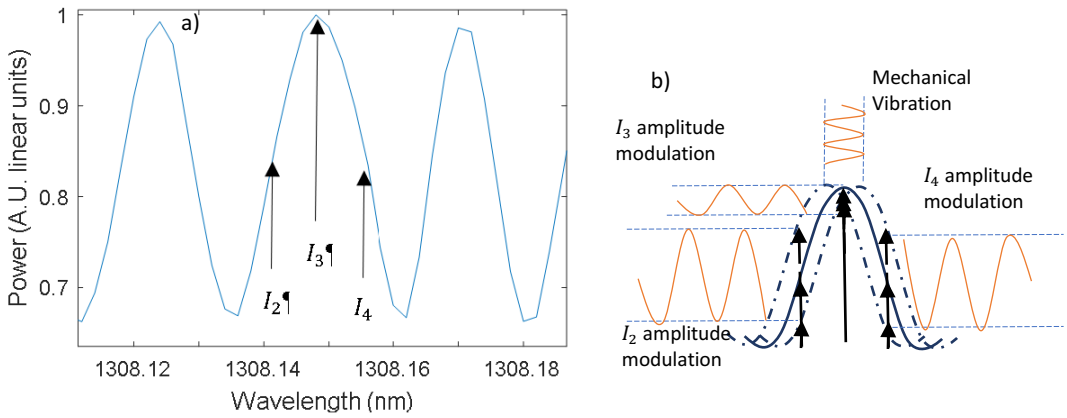

Fig. 90 Principle of measurement: a) three mode approach measurement in a static regime, b) three mode measurement in dynamic regime

For each one of the modes, an optical mix will be produced between the reference arm and the FBG arm of the interferometer as shown in Fig. 91. The tone reflected on the reference arm will travel backward and will mix with the tones that are reflected in the FBG sensor. As the mixes will happen for all the tones, theoretically, we will have multiple mixes for each reference tone. However, and due to the photodetector bandwidth, just the homolog tones will have an image in the RF domain.

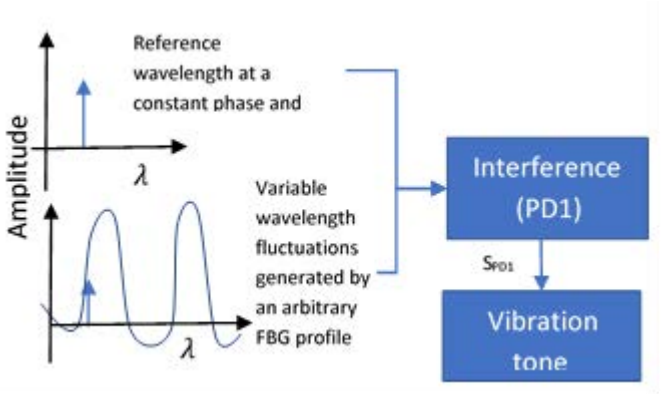

Fig. 91 Optical mix of the sensing mode and the reference mode of the dispersion readout.

The result is a multiheterodyne set of harmonics with injective mapping from the optical domain to the electrical domain. They can be read directly from the frequency domain and, therefore, their amplitude can be recovered accordingly by means of synchronous demodulation. This is achieved by mixing the interferogram with a signal corresponding to the tone I_3 and subtract it from the value of amplitude modulation of the I_5 tone. In the case of 4 MHz frequency mapping and spacing of 500 kHz between RF images, we can use a demodulating scheme like the one

shown in Fig. 92. I_3 amplitude information can be extracted from 3.5 MHz harmonic tone and I_5 information can be extracted from the 4.5 MHz harmonic tone.

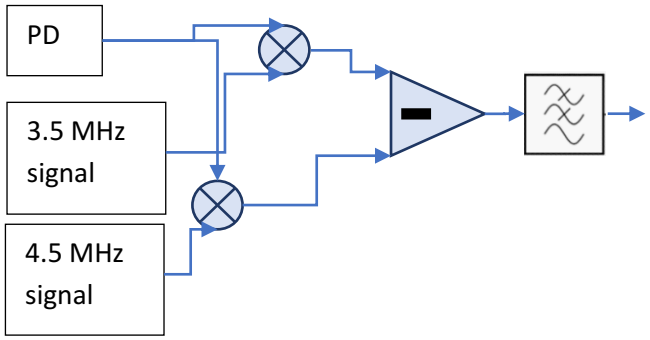

Fig. 92 Synchronous demodulation scheme for vibration recovery

8.3 Results

We measured the noise levels for different bandwidth resolutions in order to determine the quality of the measuring signal. We observe in Fig. 93 that for a higher sampling rate (x-axis) we obtain lower noise being able to reach levels of 20 pV^2/Hz for the case of the Santec laser and of about 10 pV^2/Hz in the case QDFB-LD-1550-50.

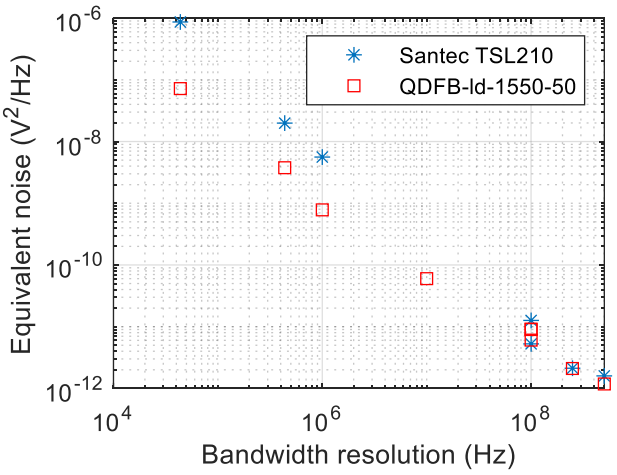

Fig. 93 Equivalent noise as a function of the bandwidth resolution for both lasers.

The result at the output of the synchronous demodulation we directly obtain a differential measurement that corresponds to the applied vibration in a small-signal regime. The main system can detect up to 140 kHz with a detection amplitude in the range of 215 nε. In Fig. 94 it can be observed a set of acquisitions correspondent to different mechanical vibrations measured with the main system.

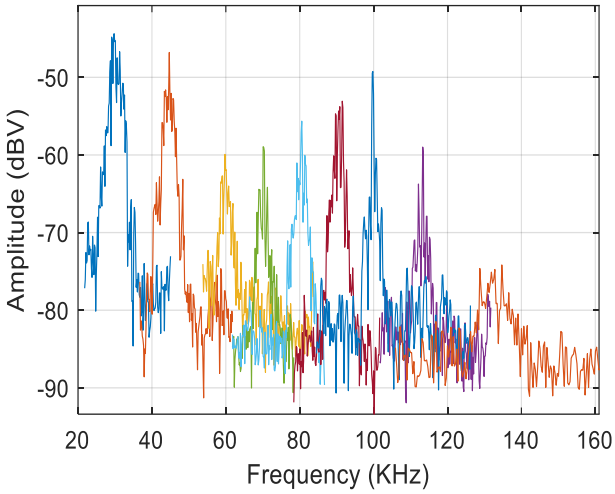

Fig. 94 Detected signals for different mechanical vibrations applied at different frequencies.

The detection range of the system was measured at 20 kHz and with the calibration interferometer. In our case the vibration range at this frequency corresponds to an inter-tone attenuation of 25 dB of attenuation as seen in Fig. 95 a). This corresponds to a depth modulation

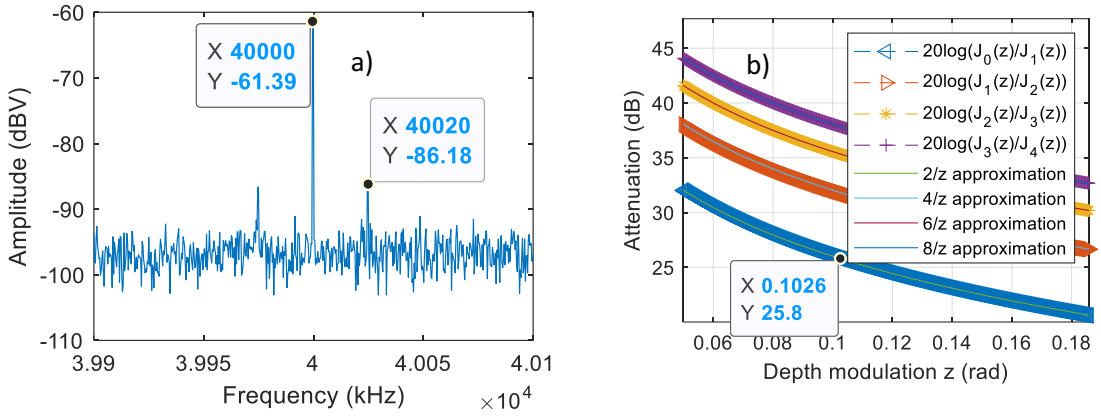

Fig. 95 Calibrating signal for the 20 kHz mechanical vibration signal: a) frequency domain of the interferogram of the calibration point b) theoretical calibration curve.

of 0.1 rad as shown in Fig. 95 b), which corresponds to 215 nε signal amplitude (see chapter 7.3).

8.4 Discussion

The performance comparison of the proposed system with respect to previous architectures of this thesis is presented in Table 2.

The theoretical limits depend on the bandwidth of the measurement system, the visibility of the interferometer and the operating wavelength. The ideal values are shown in Fig. 96 For the case of phase noise limits, we observe a linear relationship in logarithmic axis (Fig. 96 a)) as well as in absolute length imbalance measurement Fig. 96 b))

In the red dashed line, we can observe the operating zone of the interferometer built with the high-quality laser (KOHERAS ADJUSTIK E15) in terms of bandwidth and maximum achievable resolution and the black dashed line represents the operation region of the interferometer built with laser QDFB-LD-1550-50.

System implemented	**Electro-optic dual optical frequency comb**	**Acousto-optic comb**	**DD-MZM dual comb and dispersion interferometer**	**Calibration interferometer**	
Laser seed	QDFB-LD-1550-50	KOHERAS ADJUSTIK E15	Santec TSL 210	QDFB-LD-1550-50	KOHERAS ADJUSTIK E15
Minimum strain	50 nε	814 pε	215 nε (20 dB SNR)	250 nε	57 pε
Detection bandwidth	120 kHz	1 MHz	135 kHz	40 kHz	200 kHz

Table 2 Comparison between the main architectures implemented in the thesis

The quality difference between both lasers is about three orders of magnitude in resolution terms and of measurement resolution and about one decade in terms of frequency bandwidth.

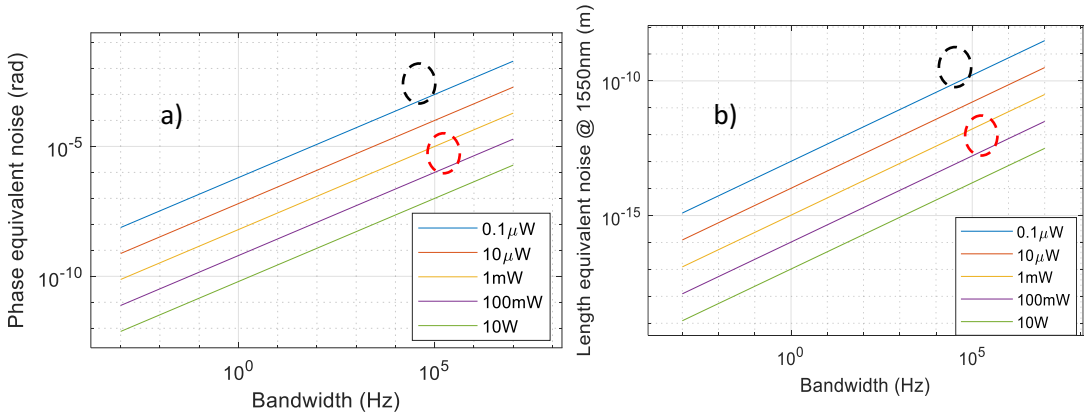

Fig. 96 Theoretical limits for interferometry sensors a) Phase equivalent noise, b) Length equivalent noise (both adapted from [58]*).*

8.5 Conclusions

In this chapter, we have shown a new architecture for reading FBG sensors in a dispersion regime. The variation of the optical phase has been measured in terms of wavelength in order to measure ultrasonic vibrations. The measurements were carried out with a multimode multiheterodyne source implemented with a dual-drive Mach-Zehnder modulator.

This chapter demonstrates:

- The viability of the new proposed scheme of the multiheterodyne source to perform spectroscopy over FBG sensors.
- The readout of dispersion characteristics of a low reflectivity FBG [59] that can be potentially used for array readout of multiple FBG sensors.
- The over-performance of this technique compared with its homolog interferometer.
- The viability to generate a multimode multiheterodyne source at 1310 nm and 1550 nm with the same optical device.
- A comparison between some of the techniques used in this thesis.

The proposed system exploits the lower optical span of a dual-comb based on a single DD-MZM and, at the same time, obtains better results than our previous implementation in Chapter 5.
The incident dual-comb samples several points in the spectrum that are sensitive to Bragg wavelength changes through the optical phase. The spectra reading is improved due to the external interferometer. The narrow-band detection of the fiber sensor dispersion changes that we demonstrate will enable compact, cost-effective, high-resolution multiheterodyne interrogation of high-throughput interferometric fiber sensors. These characteristics open its application both to the detection of fast phenomena such as ultrasound and to the precise measurement at high speed of chemical / biological sensing samples. The results with a low reflectivity fiber Bragg grating showed detection of dynamic strain in the range of 215 nε with better than 20 dB signal to noise ratio and up to 135 kHz (ultrasonic range).

Chapter 9: Conclusions and future work

“Who taught you all this, doctor?"

The reply came promptly:

"Suffering.”

— Albert Camus

9.1 Conclusions

This thesis shows different techniques based on multimode multiheterodyne sources and optical fiber sensors for measuring acoustic waves and ultrasound waves. It uses interferometrical tools and optical fiber sensors to study the applications of these techniques on complete instrumentation systems that can perform better than their homolog interferometer.

The presented approaches cover self-heterodyne combs, acousto-optic combs, electrooptic dual optical frequency combs, and a new implementation variant: the pure electrooptical dual-comb based on phase-generated carrier and serrodyne frequency shifting. All those types of sources are applied to the interrogation of the following sensors: uniform fiber Bragg gratings, random fiber gratings, chirped fiber Bragg gratings, and low reflectivity fiber Bragg gratings. The whole discussion focuses on how to implement those techniques and how to check some of the system properties that are important for the implementations, such as the optical broadness, the optical tunability, the RF mapping frequency, the RF broadness, the number of tones, etcetera. Moreover, calibration processes are shown for characterizing the capabilities in dynamic strain measurements and the wavelength resolution in the case of an HCN calibration cell. It is proven that the proposed fiber-optic sensing systems overperform the fiber-optic calibration systems.

These new architectures lead to a simpler arrangement compared with the previous systems built, as the final proposed systems are implementable with just a single compact component. Either an acousto-optic modulator for generating the self heterodyne source, or a dual-drive Mach-Zehnder modulator for generating the multiheterodyne source only electro-optically.

We can point out that most of the proposed interrogation systems can operate at several wavelengths in the window of 1310 nm and 1550 nm. This characteristic can lead to more complete functionalities and even multi-wavelength operation, as opposed to the huge immensity of state-of-the-art proposals, that focus on wideband optical comb generation, but they mainly dismiss a wideband wavelength operation due to the possibility of multiple input sources.

The achievements of this thesis are summarized as follows:

- Implementation and characterization of optical frequency combs and dual optical frequency combs for fiber sensors readout at 1310 nm and 1550 nm.
- Design and set up of prototypes based on a set of different multiheterodyne techniques for fiber sensing implementation: electro-optic dual optical frequency comb with acousto-optic frequency shift, all electro-optical dual optical frequency comb based on PGC and serrodyne modulation and finally, self-heterodyne optical frequency comb based on acousto-optic feedback.
- Vibrations measurements at ultrasound frequencies with the aforementioned optical sources and optical fiber sensors based on FBG.

In chapter 5 it was presented a dual-comb readout system for fast fiber Bragg grating interrogation. It is based on the architecture of the dual-comb composed of two electro-optical modulators and an acousto-optic modulator. The proposed system can detect up to 120 kHz with an amplitude of 340 nε and resolution of 50 με.

In chapter 6 an alternative implementation method was presented for generating a dual-comb based on a single chip dual-drive Mach Zehnder modulator. The setup was tested with an absolute reference based on an HCN cell.

In chapter 7 a system based on a self-heterodyne acousto-optic comb was presented. The system can read random fiber grating sensors in a small signal regime. It can reach 1 MHz bandwidth of mechanical vibration stimulus and resolution of 814 pε.

In chapter 8 a system able to read dispersion in FBG was presented. The device is based on a single chip implementation of the dual-comb and a dispersion interferometer. It was applied to the measurements of ultrasounds up to 135 kHz of mechanical frequencies, amplitude of 215 nε with SNR better than 20 dB.

9.2 Future work

The future investigation lines of this work are very broad because the techniques shown here can be expanded and used for other types of fiber sensors. Moreover, multiple-stage and multiple-seed expansion techniques can be used to obtain more wavelength coverage on the optical domain of the multimode sources.

Overall, this thesis presents general spectroscopic techniques for the specific goal of sensor interrogation. Therefore, the application of these tools can be explored for other problems that involve absorption/attenuation changes due to the fiber sensor or dispersion changes in the fiber sensor.

A specific example of application is to extend the use of the compact dual-comb implementation for long period grating (LPG) sensors by injecting several lasers to the same modulation device. This implementation allows to extract the transmission attenuation profile of the LPG in several wavelength regions at the same time, as it is shown in Fig. 97. In addition, it could be also adapted to obtain the dispersion profile of the sensor and its changes with a measurement target.

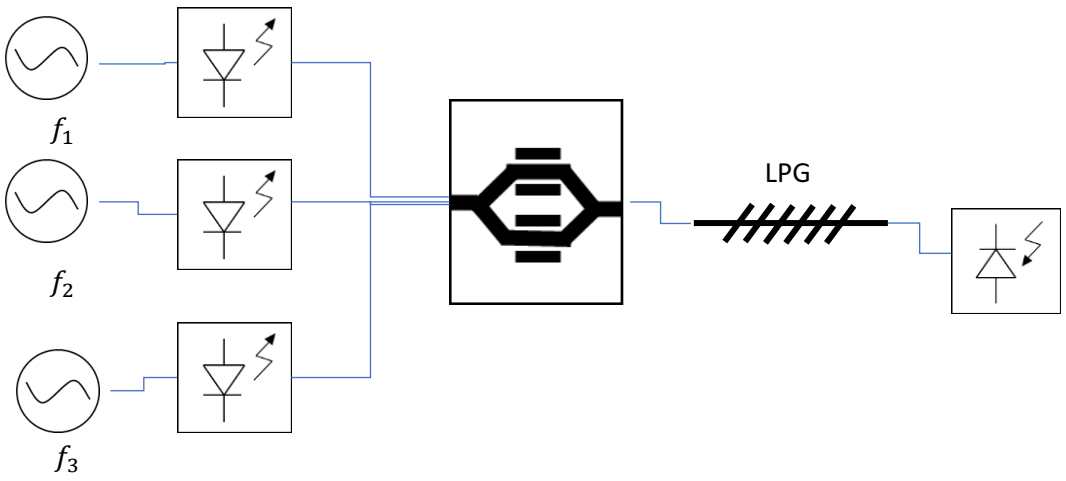

Fig. 97 Implementation of multiple wavelength operation dual optical frequency comb.

Truly distributed optical sensing along an optical fiber may be also done with non-functionalized fiber and multiheterodyne sources by applying mixed interferometers as Mach-Zehnder-Sagnac layouts [60], [61].

The evolution of different implementations throughout the thesis culminates in very compact schemes based on a single device. As a consequence, great possibilities of application in field open up due to their size and their robustness for these environments, compared with others based on fiber optic interferometric schemes. The main challenges in this case are to expand the density of sampled points in the optical spectrum (optical comb tones) and/or to expand the separation between consecutive sample points. These limitations are primarily imposed by the dual drive Mach-Zehnder modulator, whose modulation depth is limited. It is possible to explore the expansion in comb density by means of multiple cascade modulators [62], [63], the separation of comb tones by means of non-linear fiber [64] and the sampling of various regions of the optical spectrum by means of multi-wavelength seeds (laser arrays). These last open the possibility of inhomogeneous sampling of the optical spectrum adapted to the characteristics of the interferometric fiber sensor.

Glossary

ADC	*Analog to Digital Converter*
AOM	*Acousto-Optic Modulator*
AM	*Amplitude Modulation*
DD-MZM	*Dual Drive Mach-Zehnder Modulator*
DOFC	*Dual Optical Frequency Comb*
DOFCG	*Dual Optical Frequency Comb Generator*
DOFS	*Distributed Optical Fiber Sensors*
EOM	*Electro-optic modulator*
ESA	*Electrical Spectrum Analyzer*
FBG	*Fiber Bragg Grating*
MZM	*Mach-Zehnder Modulator*
NDE	*Nondestructive Evaluation*
OSA	*Optical Spectrum analyzer*
PGC	*Phase Generated Carrier*
RF	*Radio Frequency*
SHM	*Structure Health Monitoring*

SNR	*Signal to Noise Ratio*
VCSEL	*Vertical Cavity Surface Emitting Laser*

Bibliography

[1] A. Barrias, J. R. Casas, and S. Villalba, “A review of distributed optical fiber sensors for civil engineering applications,” *Sensors (Switzerland)*, vol. 16, no. 5, 2016, doi: 10.3390/s16050748.

[2] A. Othonos, “Fiber Bragg gratings,” *Rev. Sci. Instrum.*, vol. 68, no. 12, pp. 4309–4341, Dec. 1997, doi: 10.1063/1.1148392.

[3] A. D. Kersey *et al.*, “Fiber grating sensors,” *J. Light. Technol.*, vol. 15, no. 8, pp. 1442–1463, 1997, doi: 10.1109/50.618377.

[4] N. H. Pinkowski, Y. Ding, C. L. Strand, R. K. Hanson, R. Horvath, and M. Geiser, “Dual-comb spectroscopy for high-temperature reaction kinetics,” *Meas. Sci. Technol.*, vol. 31, no. 5, 2020, doi: 10.1088/1361-6501/ab6ecc.

[5] V. Durán, S. Tainta, and V. Torres-Company, “Ultrafast electrooptic dual-comb interferometry,” *Opt. Express*, vol. 23, no. 23, p. 30557, 2015, doi: 10.1364/oe.23.030557.

[6] D. A. Long *et al.*, “Multiheterodyne spectroscopy with optical frequency combs generated from a continuous-wave laser,” *Opt. Lett.*, vol. 39, no. 9, p. 2688, 2014, doi: 10.1364/OL.39.002688.

[7] N. Picqué and T. W. Hänsch, “Frequency comb spectroscopy,” *Nat. Photonics*, vol. 13, no. 3, pp. 146–157, 2019, doi: 10.1038/s41566-018-0347-5.

[8] K. Qu, S. Zhao, X. Li, Z. Zhu, D. Liang, and D. Liang, “Ultra-Flat and Broadband Optical Frequency Comb Generator via a Single Mach–Zehnder Modulator,” *IEEE Photonics Technol. Lett.*, vol. 29, no. 2, pp. 255–258, Jan. 2017, doi: 10.1109/LPT.2016.2640276.

[9] K. Qu, S. Zhao, X. Li, Q. Tan, and Z. Zhu, “Ultraflat and broadband optical frequency comb generator based on cascaded two dual-electrode Mach–Zehnder modulators,” *Opt.*

Rev., vol. 25, no. 2, pp. 264–270, Apr. 2018, doi: 10.1007/s10043-018-0417-4.

[10] L. A. Huancachoque, M. L. M dos Santos, A. I. N B Pereira, D. V G Nascimento, and A. C. Bordonalli, *Optical Frequency Comb Generation by Dual Drive Mach-Zehnder Modulator with Algorithm-assisted Efficient Amplitude Equalization*. .

[11] V. Duran, C. Schnebelin, and H. G. de Chatellus, "Acousto-optic frequency combs for heterodyne interferometry," in *2017 XXXIInd General Assembly and Scientific Symposium of the International Union of Radio Science (URSI GASS)*, Aug. 2017, pp. 1–2, doi: 10.23919/URSIGASS.2017.8105189.

[12] V. Duran *et al.*, "Optical Frequency Combs Generated by Acousto-Optic Frequency-Shifting Loops," *IEEE Photonics Technol. Lett.*, vol. 31, no. 23, pp. 1878–1881, Dec. 2019, doi: 10.1109/LPT.2019.2947655.

[13] B. Jerez, P. Martín-Mateos, F. Walla, C. de Dios, and P. Acedo, "Flexible Electro-Optic, Single-Crystal Difference Frequency Generation Architecture for Ultrafast Mid-Infrared Dual-Comb Spectroscopy," *ACS Photonics*, p. acsphotonics.8b00143, 2018, doi: 10.1021/acsphotonics.8b00143.

[14] P. Martín-Mateos, B. Jerez, P. Largo-Izquierdo, and P. Acedo, "Frequency accurate coherent electro-optic dual-comb spectroscopy in real-time," *Opt. Express*, vol. 26, no. 8, p. 9700, Apr. 2018, doi: 10.1364/OE.26.009700.

[15] P. Martín-Mateos and P. Acedo, "Electro-Optic Dual Optical Frequency Combs: New Architectures and Opportunities Beyond Spectroscopy," *Light. Energy Environ.*, vol. 1, no. January, p. FM4D.3, 2016, doi: 10.1364/FTS.2016.FM4D.3.

[16] P. Martin-mateos, "New Spechtroscopic Techniques and Architectures for Environmental and Biomedical Applications," 2015.

[17] P. Martín-Mateos, A. Porro, and P. Acedo, "Fully Adaptable Electro-Optic Dual-Comb Generation," *IEEE Photonics Technol. Lett.*, vol. 30, no. 2, pp. 161–164, 2018, doi: 10.1109/LPT.2017.2779464.

[18] D. A. Jackson, A. D. Kersey, M. Corke, and J. D. C. Jones, "Pseudoheterodyne detection scheme for optical interferometers," *Electron. Lett.*, vol. 18, no. 25–26, pp. 1081–1083, Dec. 1982, doi: 10.1049/el:19820740.

[19] F. To, S. Yu, and S. Yin, *Fiber Optic Sensors*, vol. 20020456. CRC Press, 2002.

[20] E. Udd and W. B. Spillman, *Fiber optic sensors : an introduction for engineers and scientists*. John Wiley & Sons, 2011.

[21] B. E. A. Saleh and M. C. Teich, *Fundamentals of photonics*. .

[22] A. V. Oppenheim, A. S. Willsky, S. Hamid Nawab, G. Mata Hernández, and A. Suárez Fernández, *Señales y sistemas*. Prentice Hall, 1998.

[23] S. Dewra and A. Grover, "Fabrication and Applications of Fiber Bragg Grating-A Review," *Adv. Eng. Tec. Appl*, vol. 4, no. 2, pp. 15–25, 2015, doi: 10.12785/aeta/040202.

[24] W. Xu, X. Gao, M. Zhao, M. Xie, and S. Huang, "Full duplex radio over fiber system with frequency quadrupled millimeter-wave signal generation based on polarization multiplexing," *Opt. Laser Technol.*, vol. 103, p. Using, S. I. (2008). with a Long Gauge FBG Sensor, 2018, doi: 10.1016/j.optlastec.2018.01.035.

[25] S.-H. Hsu, K.-W. Chuang, C.-S. Chen, C.-Y. Lin, and C.-C. Chang, "Two Interrogated FBG Spectral Linewidth for Strain Sensing through Correlation," *Sensors*, vol. 17, no. 12, p. 2837, Dec. 2017, doi: 10.3390/s17122837.

[26] M. Mądry, K. Markowski, K. Jędrzejewski, and E. Bereś-Pawlik, "Temperature monitoring system using correlated FBGs," in *INTERNATIONAL CONFERENCE ON OPTICAL FIBRE SENSORS (OFS24)*, Sep. 2015, vol. 9634, p. 963477, doi: 10.1117/12.2194812.

[27] P. Han, Z. Li, L. Chen, and X. Bao, "A high-speed distributed ultra-weak FBG sensing system with high resolution," *IEEE Photonics Technol. Lett.*, vol. 29, no. 15, pp. 1249–1252, 2017, doi: 10.1109/LPT.2017.2712182.

[28] C. Campanella, A. Cuccovillo, C. Campanella, A. Yurt, and V. Passaro, "Fibre Bragg Grating Based Strain Sensors: Review of Technology and Applications," *Sensors*, vol. 18, no. 9, p. 3115, 2018, doi: 10.3390/s18093115.

[29] L. a. Ferreira, E. V. Diatzikis, J. L. Santos, and F. Farahi, "Frequency-modulated multimode laser diode for fiber Bragg grating sensors," *J. Light. Technol.*, vol. 16, no. 9, pp. 1620–1630, 1998, doi: 10.1109/50.712245.

[30] L. A. Ferreira, E. V. Diatzikis, J. L. Santos, and F. Farahi, "Demodulation of Fiber Bragg Grating Sensors Based on Dynamic Tuning of a Multimode Laser Diode," *Appl. Opt.*, vol. 38, no. 22, pp. 4751–4759, 1999, doi: 10.1364/AO.38.004751.

[31] J. Posada-Roman, J. Garcia-Souto, D. Poiana, and P. Acedo, “Fast Interrogation of Fiber Bragg Gratings with Electro-Optical Dual Optical Frequency Combs,” *Sensors*, vol. 16, no. 12, p. 2007, Nov. 2016, doi: 10.3390/s16122007.

[32] I. Navruz and A. Altuncu, “Design of a Chirped Fiber Bragg Grating for use in Wideband Dispersion Compensation,” in *New Trends in Computer Networks*, Sep. 2005, pp. 114–123, doi: 10.1142/9781860947308_0012.

[33] Y. Okabe, R. Tsuji, and N. Takeda, “Application of chirped fiber Bragg grating sensors for identification of crack locations in composites,” *Compos. Part A Appl. Sci. Manuf.*, vol. 35, no. 1, pp. 59–65, Jan. 2004, doi: 10.1016/J.COMPOSITESA.2003.09.004.

[34] H. Kogelnik, “Filter Response of Nonuniform Almost-Periodic Structures,” *Bell Syst. Tech. J.*, vol. 55, no. 1, pp. 109–126, 1976, doi: 10.1002/j.1538-7305.1976.tb02062.x.

[35] P. Lu, S. J. Mihailov, D. Coulas, H. Ding, and X. Bao, “Low-Loss Random Fiber Gratings Made with an fs-IR Laser for Distributed Fiber Sensing,” *J. Light. Technol.*, vol. 37, no. 18, pp. 4697–4702, Sep. 2019, doi: 10.1109/JLT.2019.2917389.

[36] Y. Xu *et al.*, “Optical fiber random grating-based multiparameter sensor,” *Opt. Lett.*, vol. 40, no. 23, p. 5514, Dec. 2015, doi: 10.1364/OL.40.005514.

[37] M. Abramowitz and I. A. Stegun, *Handbook of mathematical functions, with formulas, graphs, and mathematical tables,*. Dover Publications, 1965.

[38] I. Coddington, N. Newbury, and W. Swann, “Dual-comb spectroscopy,” *Optica*, vol. 3, no. 4, p. 414, Apr. 2016, doi: 10.1364/OPTICA.3.000414.

[39] V. Durán, S. Tainta, and V. Torres-Company, “Ultrafast electrooptic dual-comb interferometry,” *Opt. Express*, vol. 23, no. 23, p. 30557, 2015, doi: 10.1364/OE.23.030557.

[40] N. B. Hébert, V. Michaud-Belleau, J. D. Anstie, J.-D. Deschênes, A. N. Luiten, and J. Genest, “Self-heterodyne interference spectroscopy using a comb generated by pseudo-random modulation,” *Opt. Express*, vol. 23, no. 21, p. 27806, 2015, doi: 10.1364/oe.23.027806.

[41] V. Durán, C. chnébelin, and H. Guillet de Chatellus, “Coherent multi-heterodyne spectroscopy using acousto-optic frequency combs,” *Opt. Express*, vol. 26, no. 11, p. 13800, May 2018, doi: 10.1364/oe.26.013800.

[42] H. Guillet De Chatellus, E. Lacot, W. Glastre, O. Jacquin, and O. Hugon, “Theory of Talbot lasers,” *Phys. Rev. A - At. Mol. Opt. Phys.*, vol. 88, no. 3, p. 033828, Sep. 2013, doi: 10.1103/PhysRevA.88.033828.

[43] C. K. Chatterjea, S. W. James, and R. P. Tatam, “Pseudoheterodyne signal processing scheme for interrogation of fiber Bragg grating sensor arrays,” *Laser Interferom. IX Tech. Anal.*, vol. 3478, pp. 266–274, Jun. 1998, doi: 10.1117/12.312945.

[44] S. Ozharar, F. Quinlan, I. Ozdur, S. Gee, and P. J. Delfyett, “Ultraflat Optical Comb Generation by Phase-Only Modulation of Continuous-Wave Light,” *IEEE Photonics Technol. Lett.*, vol. 20, no. 1, pp. 36–38, Jan. 2008, doi: 10.1109/LPT.2007.910755.

[45] T. Sakamoto, T. Kawanishi, and M. Izutsu, “Asymptotic formalism for ultraflat optical frequency comb generation using a Mach-Zehnder modulator,” *Opt. Lett.*, vol. 32, no. 11, p. 1515, Jun. 2007, doi: 10.1364/OL.32.001515.

[46] D. A. Poiana, J. A. Garcia-Souto, J. E. Posada, and P. Acedo, “All-Fiber Electro-Optic Dual Optical Frequency Comb for Fiber Sensors,” in *26th International Conference on Optical Fiber Sensors*, Sep. 2018, p. WF82, doi: 10.1364/OFS.2018.WF82.

[47] D. M. S. Johnson, J. M. Hogan, S. -w. Chiow, and M. A. Kasevich, “Broadband optical serrodyne frequency shifting,” *Opt. Lett.*, vol. 35, no. 5, p. 745, 2010, doi: 10.1364/ol.35.000745.

[48] I. Coddington, N. Newbury, and W. Swann, “Dual-comb spectroscopy,” *Optica*, vol. 3, no. 4, p. 414, Apr. 2016, doi: 10.1364/OPTICA.3.000414.

[49] D. A. Poiana, J. A. Garcia-Souto, J. E. Posada, and P. Acedo, “Stabilization of coherent dual optical frequency comb for fiber Bragg Grating sensing,” *Proc. IEEE Sensors*, vol. 2017-Decem, pp. 1–3, 2017, doi: 10.1109/ICSENS.2017.8234082.

[50] B. Xue *et al.*, “Absolute Distance Measurement by Self-Heterodyne EO Comb Interferometry,” *IEEE Photonics Technol. Lett.*, vol. 30, no. 9, pp. 861–864, May 2018, doi: 10.1109/LPT.2018.2820710.

[51] D. A. Jackson, J. A. Garcia-Souto, and J. E. Posada-Roman, “Calibration of laser Doppler vibrometer exploiting Bessel functions of the first kind,” *Electron. Lett.*, vol. 51, no. 14, pp. 1100–1102, Jul. 2015, doi: 10.1049/el.2015.0972.

[52] P. Hariharan, *Basics of interferometry*. Elsevier Academic Press, 2007.

[53] S. Y. Huang, M. M. Ohn, M. LeBlanc, R. Lee, and R. M. Measures, “Fiber optic intra-grating distributed strain sensor,” *Distrib. Mult. Fiber Opt. Sensors IV*, vol. 2294, no. 1, pp. 81–92, 1994, [Online]. Available: http://scitation.aip.org/getabs/servlet/GetabsServlet?prog=normal&id=PSISDG002294000001000081000001&idtype=cvips&gifs=yes.

[54] S. Huang, M. M. Ohn, and R. M. Measures, “Phase-based Bragg intragrating distributed strain sensor,” *Appl. Opt.*, vol. 35, no. 7, p. 1135, 2008, doi: 10.1364/ao.35.001135.

[55] S. Huang, M. LeBlanc, M. M. Ohn, and R. M. Measures, “Bragg intragrating structural sensing,” *Appl. Opt.*, vol. 34, no. 22, p. 5003, 2009, doi: 10.1364/ao.34.005003.

[56] P. Hariharan, B. F. Oreb, and T. Eiju, “Digital phase-shifting interferometry: a simple error-compensating phase calculation algorithm,” *Appl. Opt.*, vol. 26, no. 13, p. 2504, Jul. 1987, doi: 10.1364/AO.26.002504.

[57] P. Hariharan, *Optical interferometry*. Academic Press, 2003.

[58] S. Donati, *Electro-optical instrumentation : sensing and measuring with lasers*. Upper Saddle River NJ: Prentice Hall, 2004.

[59] X. Zhao *et al.*, “Dynamic quasi-distributed ultraweak fiber bragg grating array sensing enabled by depth-resolved dual-comb spectroscopy,” *IEEE Trans. Instrum. Meas.*, vol. 69, no. 8, pp. 5821–5827, Aug. 2020, doi: 10.1109/TIM.2019.2959754.

[60] Xiaojun Fang, “A variable-loop Sagnac interferometer for distributed impact sensing,” *J. Light. Technol.*, vol. 14, no. 10, pp. 2250–2254, 1996, doi: 10.1109/50.541215.

[61] S. J. Spammer, P. L. Swart, and A. A. Chtcherbakov, “Distributed dual-wavelength Sagnac impact sensor,” *Microw. Opt. Technol. Lett.*, vol. 17, no. 3, pp. 170–173, Feb. 1998, doi: 10.1002/(SICI)1098-2760(19980220)17:3<170::AID-MOP6>3.0.CO;2-G.

[62] B. Das, K. Mallick, P. Mandal, B. Dutta, C. Barman, and A. S. Patra, “Flat optical frequency comb generation employing cascaded dual-drive Mach-Zehnder modulators,” *Results Phys.*, vol. 17, p. 103152, Jun. 2020, doi: 10.1016/J.RINP.2020.103152.

[63] G. Millot *et al.*, “Frequency-agile dual-comb spectroscopy,” *Nat. Photonics*, vol. 10, no. 1, pp. 27–30, 2016, doi: 10.1038/nphoton.2015.250.

[64] S. Wang, X. Fan, B. Xu, and Z. He, “Dense electro-optic frequency comb generated by two-stage modulation for dual-comb spectroscopy,” *Opt. Lett.*, vol. 42, no. 19, p. 3984,

2017, doi: 10.1364/OL.42.003984.